Doctoral Dissertation
Doctoral Program in Physics (33rd cycle)

Computational study of reduced Graphene Oxide properties for membrane applications

Filippo Savazzi
* * * * * *

Supervisor
Prof. Giancarlo Cicero

Doctoral Examination Committee:
Dr. Arthur France-Lanord, Referee, Sorbonne Université
Dr. Alessandra Catellani, Referee, Consiglio Nazionale delle Ricerche
Dr. Damien Voiry, Université de Montpellier
Prof. Maurizia Palummo, Università degli Studi di Roma "Tor Vergata"
Prof. Andrea Lamberti, Politecnico di Torino

Politecnico di Torino
April 23, 2021

I hereby declare that, the contents and organization of this dissertation constitute my own original work and do not compromise in any way the rights of third parties, including those relating to the security of personal data.

. . . . . .

Filippo Savazzi
Turin, April 23, 2021

Acknowledgements

I would like to thank my supervisor, Prof. Giancarlo Cicero, for his valuable help and guidance in developing my research project. I would also like to thank Dr. Federico Raffone and Dr. Francesca Risplendi with whom I worked in collaboration to obtain many of the results reported in this thesis. Finally I would like to thank Prof. Jeffrey Grossman and his group at the Massachusetts Institute of Technology for giving me the opportunity to work with them during my research period abroad, as it was a very formative experience.

Summary

In this doctoral thesis we use state-of-the-art atomistic simulations to model and investigate the electronic properties of reduced Graphene Oxide (GO), the evolution of oxygen-containing groups in its structure and the properties of the interface that it forms with water. Reduced GO (rGO) is a very versatile material, atomically-thin as graphene but with much higher complexity due to its variable composition. It is fabricated by oxidizing graphite, a treatment that induces complex modifications to the structural and electronic properties of this material that are still not completely understood.

In this work we try to address some important questions that are still open in GO literature, in particular we present the results of a thorough computational investigation of the structural and electronic properties of rGO, based on accurate classical Molecular Dynamics (MD) and Density Functional Theory (DFT) simulations. We suggest a modification to a widely used structural model for GO and provide useful indications to help interpreting XPS C1s spectra. Moreover, we discuss the mechanisms that lead to oxygen-containing species to diffuse and clusterize in monolayer rGO and investigate how to control this phenomenon and exploit it for producing pores of controlled size. In fact, we provide reliable indications to produce porous single layer rGO membranes for water filtration in a scalable and controllable way. Finally, we investigate the interactions between water and rGO and study how its composition influences surface wettability. We conclude this research project studying the effects of confinement on water between rGO flakes, considering a realistic interlayer distance between the latter as observed in multilayer rGO membranes when soaked in water. Conclusions from these work will shine light on the relationships between microscopical features of rGO flakes and the diffusivity of water molecules in their proximities, fundamental to engineer efficient membranes for water desalination.

Contents

List of Figures

Introduction

In this doctoral thesis we aim at improving scientific knowledge on the nature of reduced rGO, by shining light on its structural and electronic properties, and at facilitating its usage in membrane technology for water filtration. We used combinations of state-of-the-art atomistic simulations, such as DFT, classical and *ab initio* MD, Cluster Expansion (CE) and Kinetic Monte Carlo (KMC) to model and investigate the electronic properties of rGO, the evolution of oxygen-containing groups in its structure and the properties of the interface that it forms with water. The use of quantum and classical atomistic techniques allowed us to accurately evaluate the effects of specific oxygen-containing groups on the key properties of this material at a microscopic scale, impossible to reach experimentally. Reduced GO, but more generally GO, is a very versatile material, atomically-thin as graphene but with much higher complexity due to its variable composition. It is fabricated by oxidizing graphite, leading to the incorporation of oxygen-containing species in the hexagonal lattice of sp^2-hybridized carbon atoms. The presence of these oxygen-containing groups facilitate the exfoliation of stacked graphite flakes and leads to the dispersion of the latter in solution, as actual 2D monolayers. For this reason, as we will see in the following, the oxidation of graphite to GO, its exfoliation and deoxygenation are considered a viable route to produce chemically-derived graphene that should be cheaper and more scalable than mechanical exfoliation or CVD deposition [1]. More intriguing than exfoliation, the oxidation of graphite induce complex modifications to the structural and electronic properties of this material that are still not completely understood. Due to this lack of knowledge, the use of GO has been almost entirely limited to scientific research until recent. Nowadays, it receives particular interest for its possible use as substrate for optoelectronics applications, as well as for the fabrication of FET and sensors, thanks to the possibility of tuning its characteristics by controlling its composition [2]. In this work instead, we will mainly explore the application of rGO for the production of membranes for water purification, a field where, as we will see, it has the potential to make a relevant impact.

In this work we try to address some important questions that are still open in GO literature, in particular:

- Which are the effects of specific oxygen-containing species on the structure and properties of rGO?

- How to address difficulties in fabricating porous monolayers with reliable pore size to produce single- layer graphitic membranes?
- How rGO is modified at the atomic level when in contact with water, and how the wetting properties of its surface are modified by its composition?

In Chapter 1 we review scientific literature on GO, since it was first obtained in 1855 [3]. We briefly discuss fabrication methods, together with the intermediate phases and transformations that graphite undergoes during its oxidation and exfoliation to GO, as well as the main strategies to tune its composition. Moreover, we reviewed the main structural models for this material, in order to understand their contributions and limitations. The reader will discover that these structural models evolved together with characterization techniques, to adapt and explain new experimental evidences, although incongruences persist among contemporary models [2], which justify further investigations. Finally, we review the main technological applications of GO, with particular focus on the field of reverse osmosis membranes for water purification.

In Chapter 2 are briefly introduced the computational methods that we used to investigate rGO in this work. We outline the foundations of DFT and its state of the art implementations, as well as the basic concepts of MD in both its classical and *ab initio* applications. DFT and MD simulations are the core of this doctoral thesis and allowed us to accurately model rGO, study its properties and microscopical characteristics and finally model its behavior when in contact with water. Moreover, we introduce the use of CE to accurately predict the configurational energy of rGO structures containing oxygen-containing groups clusters and of KMC technique to simulate the evolution of rGO samples under realistic experimental conditions.

In Chapter 3 we present the results of a thorough computational investigation of the structural and electronic properties of rGO, based on accurate classical MD and DFT simulations. We created reliable models for monolayer rGO at different degrees of oxidation and stoichiometries to study the effects of specific oxygen-containing groups on the electronic properties of this material and the structural deformations that they induce. Based on these simulations, we suggest a modification to a widely used structural model for GO and provide useful indications to help interpreting XPS C1s spectra.

In Chapter 4 we discuss the mechanism that lead to oxygen-containing species to diffuse and clusterize in monolayer rGO and investigated how to control this phenomenon to exploit it for producing pores of controlled size. We presented the results of a complex computational study involving state of the art DFT, CE, KMC and MD simulations and provided reliable indications to produce porous single layer rGO membranes for water filtration in a scalable and controllable way.

In Chapter 5 we investigate the interactions between rGO and water, considering the modifications induced by water on the material, in particular how oxygen-containing groups evolve or desorb, as well as the effects of the surface on the properties of interfacial water. We study how the composition of rGO influences surface wettability by analyzing fundamental physical quantities. Moreover, we investigate the effects of

confinement on water between rGO flakes, considering an interlayer distance between the latter as observed in multilayer rGO membranes when soaked in water. Conclusions from these work shine light on the relationships between microscopical features of rGO flakes and the diffusivity of water molecules in their proximities, fundamental to engineer efficient membranes for water desalination.

Chapter 1

Graphene Oxide

1.1 Introduction

GO is a two-dimensional (2D) graphitic material with oxygen-containing groups on its surface. It consists of a monolayer of sp^2-hybridized carbon atoms forming a honeycomb 2D lattice, as graphite, with covalently bonded oxygen-containing species distributed randomly over the surface which locally modify carbon atoms hybridization to sp^3. It is usually produced oxidizing graphite in strongly acidic solutions, with the procedure eventually leading to the separation of oxidized graphitic monolayers in suspension. The dispersion of GO layers in solution can be complete, leading to flakes of monolayer GO (2D) suspended in solution, or partial, leading to suspended flakes of multilayer GO. In Figure 1.1 are reported examples of (a) monolayer GO flakes and (b) multilayer GO flakes, after being separated from solution and deposited on a substrate. GO was first reported by Brodie in 1855 [3] and a detailed description of its preparation was published in 1859 [4]. This involved the treatment of graphite precursors with concentrated nitric acid together with potassium chlorate. By the end of the 19^{th} century this material had already withdrew the interest of many chemists, in particular for what concerned preparation methods, with the quest of finding alternative and less dangerous oxidizing reagents. Indeed in 1898 Staudenmaier [5] published the first review on the various preparation methods existing for GO.

During the 20^{th} century, research on GO focused on studying the chemo-physical properties of this material and defining unambiguously its composition and structure, also with the aid of newly developed techniques such as x-ray diffraction (XRD) [6]. After a century there are still many open questions about GO composition and properties, with a universal structural model that remains elusive and leaves research in the field open. These difficulties are due to a large variability in oxidation levels following from different preparations, instability of the bonded oxygen-containing species which continuously evolve on the surface and the amorphous structure that arises from the previous two. A further level of complication comes from the sensitivity of GO structure and composition to ambient conditions, such as temperature and humidity, that leads

to frequent reactions between GO and its surroundings typically involving the release of CO and CO_2 molecules or proton exchange with water. This reactivity, as we will see, can be exploited to tailor the composition of GO samples by mean of controlled reduction processes. What is known today about GO is that it is a metastable material, whose properties and composition continuously change under the influence of temperature, light and exposure to water. When heat is applied, a slow decomposition starts with the release of CO and CO_2, at temperatures slightly higher than room temperature, and continues at higher temperatures with the material loosing weight by dehydration and decomposition. Scholz reported that GO decomposition starts at temperatures as low as 50°C, observing a very slow color transition and release of CO and CO_2 [7]. GO reacts with many reducing agents which remove oxygen-containing groups from its structure, leaving dispersed graphite layers with a low degree of oxidation. Deoxygenation of dispersed GO layers by means of reducing agent allowed for the first time to obtain carbon monolayers [8]. Since GO was first reported, its acidic properties were noticed [4] [9] as well as the tendency to release protons and uptake ions when dispersed in a basic solution [10]. In 1956 Clauss et al demonstrated that multilayer GO films are permeable to water while almost impermeable to many other molecules [11].

More recently, after the discovery of graphene in 2004 by Novoselov and Geim [12], research on GO gained new momentum thanks to many affinities and similarities between the two materials. This latter stage of research on GO is mainly focused on technological applications as we will see at the end of this chapter. In this thesis, we will address primarily the use of rGO for its application in membranes for water desalination, trying to provide answers to some of the main challenges that currently limit the use of this kind of membranes.

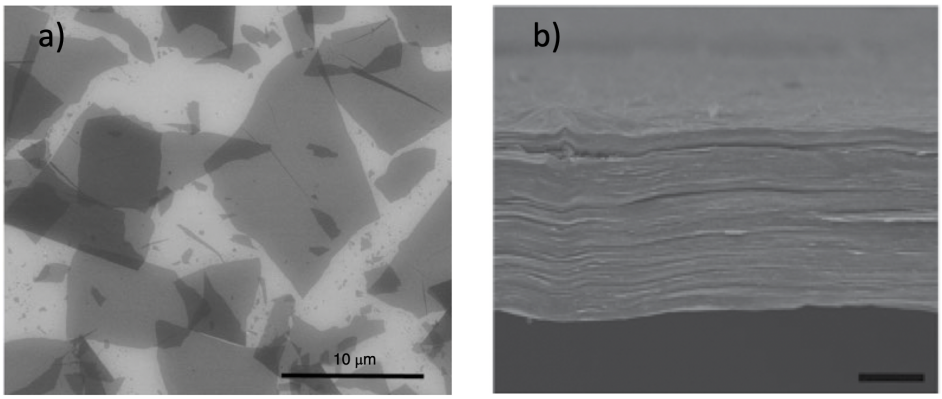

Figure 1.1: SEM acquisitions of (a) monolayer GO flakes (it is possible to see where they overlap as darker-gray two-layer structures) and (b) thick multilayer GO paper. Figures reproduced from [2] with permissions from John Wiley and Sons.

1.2 GO fabrication and reduction

In 1859 Brodie published a paper [4] that described the production of GO with a mixture of highly concentrated nitric acid and potassium chloride in which graphite is immersed for 3-4 days at 60°C, followed by washing with water and vacuum drying. This procedure is cycled several times until the maximum possible oxidation is reached and became known in the literature as "Brodie method". As we previously mentioned, the preparation of GO has been the subject of a great deal of research [5] [13] [14] [7] [15] [16]. In 1898 Staudenmaier reported a procedure to exfoliate graphite using a mix of sulfuric and nitric acids and adding potassium chlorate [5], known as the "Staudenmaier method", which nonetheless involved the use of hazardous substances, the production of poisonous gases and the risk of explosions. In 1958, Hummers and Offeman published a method that use potassium permanganate ($KMnO_4$) as oxidant agent to produce GO [15], which involves sulfuric acid and sodium nitrate and is carried at lower temperatures than the "Staudenmaier method" preventing the risk of explosion. Today this is known as the "Hummers method".

These three methods are predominant nowadays in the production of GO, with a large collection of different treatments published between the 19^{th} and 20^{th} centuries that never gained popularity and today are left as scientific history. A first review of these three main methods was published by Boehm and Scholz [17] whose main conclusions were that: (1) the Brodie method produced the most stable and purest samples, (2) the purification of samples prepared using the Hummers and Staudenmaier methods was more difficult due to a higher degree of contaminants, (3) there is a general trend in the degree of oxidation of samples, with the Brodie method resulting in lower oxidation, followed by the Staudenmaier method and finally the Hummers method resulting in higher oxidation degrees. It is worth mentioning that according to Dimiev [2], reality is not as straightforward and GO with different oxidation degrees can be produced by all three methods by varying quantities of reagents and times.

1.2.1 Main preparation methods

Brodie method

In his paper of 1859, Brodie laid the bricks for research in GO production and characterization. He first reported the protocol to oxidize graphite which became known as the "Brodie method" for producing GO. Graphite is oxidized by mixing it with three times its weight of potassium chlorate ($KClO_3$), then adding enough fuming nitric acid (concentrated HNO_3) to make the compost fluid and leaving it at 60°C for three to four days. The compound is then washed in abundant water and dried, finally the whole procedure is repeated until no further change is noticed (usually 4 - 5 times) [4]. Interestingly it is reported that leaving the liquid compost in a flask under direct sunlight speeds up the oxidation reaction and without any need for heating. Brodie examined

the resulting crystals with an optical microscope and described them as extremely thin and transparent. He then reported a careful study of the composition of these crystals by analyzing the products of their combustion using samples taken at different oxidation steps to evaluate after how many cycles the oxidation is completed. The reported average composition of these samples lead to a proposed $C_{11}H_4O_5$ formula. Brodie also reported successive thermal treatments that he applied to his GO samples before checking their composition by combustion analysis. He reported that, upon heating at about 250°C until gas evolution ceases (typically 3 - 4 hours), GO produced transparent crystals whose composition lead to a $C_{22}H_2O_4$ formula which implies a 4 times reduction of hydrogen content and a 2.5 times reduction of oxygen content.

Staudenmaier method

In 1898, Staudenmaier published an alternative method to Brodie's for the production of GO. This uses $KClO_3$ in a mixture of concentrated sulfuric (H_2SO_4) and nitric (HNO_3) acids, with particular attention required in providing multiple portions of $KClO_3$ during the reaction since this is consumed quickly. The whole procedure, which takes place in one step (whereas Brodie's needs many cycles of oxidation-washing) takes 4 days to complete. Staudenmaier reported that the product obtained after washing and drying was green, but could be turned to yellow with a solution of $KMnO_4$ and diluted H_2SO_4. This method uses relatively hazardous reagents, is prone to explosion and takes a long time to complete, although it improves preparation efficiency with respect to the Brodie method since it is complete in just one step. Boehm and Scholz [17] reported a carbon content in samples prepared with the Staudenmaier method to be on average 57%.

Hummers method

The idea of using of $KMnO_4$ together with H_2SO_4 to oxidize graphite was first introduced by Charpy in 1909[14] although it took until 1958 to become popular, when Hummers and Offeman published a new protocol $KMnO_4$ to oxidize graphite and produce GO. They mixed powdered graphite flakes with sodium nitrate ($NaNO_3$), placed it in a solution of concentrated H_2SO_4 and added portions of $KMnO_4$ while limiting reaction temperatures below 20°C. This method uses $KMnO_4$ as oxidant rather than chlorates, requires only concentrated H_2SO_4 and as the authors claim it is complete in only 2 hours. Boehm and Scholz [17] reported a carbon content in samples prepared with the Hummers method ranging between 56% and 64%. Nowadays this is the most used method to produce GO, thanks to shorter reaction times and lack of toxic fumes from nitric acid and chlorates.

1.2.2 Formation mechanisms

The oxidation of graphite flakes and their transformation into GO proceeds by sequential steps. Independently on the preparation method of choice, graphite is first oxidized in water-free conditions when the oxidant agents intercalate within graphite layers after the interlayer distance between these latter is increased by the action of the acid. Finally these oxidized flakes are exposed to water and exfoliate into GO. It is possible to identify three different phases of GO formation which correspond to separate steps during the preparation procedure [2], in the following we will examine these phases while following the Hummers method.

Step 1

When graphite powder is exposed to H_2SO_4, this diffuses between graphite layers and continues until every layer is intercalated by the acid. Graphite turns deep blue during this step, while the main structural effect of this intercalation is the increase of the interlayer distance between graphitic layers.

Step 2

After the oxidizing agent ($KMnO_4$ in the case of the Hummers method) is added to the mixture, this moves within graphite layers aided by the increased interlayer distance, substituting H_2SO_4 while oxidizing carbon atoms. The oxidation reaction occurs from edge to center of the intercalated flakes and is diffusion controlled. During this phase, which takes several hours, flakes turn from deep blue to light yellow.

Step 3

In this last phase the oxidized compound is exposed to water during washing procedures, which may involve stirring, sonication or other treatments, depending on the preparation protocol. When in contact with water single atomic layers are exfoliated and dispersed in solution which changes color from light yellow to dark brown.

1.2.3 Reduction treatments

Once GO is prepared, depending on the fabrication method its carbon weight content typically ranges from 55% to 60%, which translates into a percentage of C atoms in GO flakes ranging from 60% to 65%. In this subsection we will introduce the concept of oxygen removal in GO to prepare rGO and see how this is typically achieved in literature. The reasons to reduce the oxygen content of GO can be many, depending usually on final applications, among them there is the possibility to tune the electronic, optical and mechanical properties of GO layers, change its morphology, reactivity and wettability, as well as to attempt the production of high-quality graphene. The removal

of oxygen from GO is typically achieved following three different routes: thermally, chemically or electrochemically.

Thermal deoxygenation, first reported by Brodie in 1859 [4], beside removing oxygen-containing groups, decomposes GO in CO_2 and CO, leaving damaged layers with defects and holes. Epoxide and hydroxyl groups are almost completely removed after treatment in a 160°C - 300°C range, while carbonyls are removed at temperatures above 500°C. Although for temperatures above 700°C the graphitic layer is partially healed, the resulting rGO is still very defective and its electrical properties are largely inferior than those of pristine graphene and chemically reduced GO [2].

Chemical reduction was also first reported by Brodie in 1859 describing the treatment of GO with reducing agents like potassium and ammonium sulfide [4]. Hoffman and collaborators concluded that the removed amount of oxygen depends on the reducing agent employed [18]. According to their study, Fe(II) chloride removes 68% of the oxygen content, hydrazine hydrate 82% and H_2S 91%. Hydroquinone and $NaBH_4$ were introduced by Bourlinos and coworkers in 2003 [19], with the former being of special interest since it produce rGO with higher crystalline quality [2].

Electrochemical reduction was introduced in 2009 by Zhou et al. While it can be considered an environment-friendly approach, since it does not involve any hazardous chemical, its application is limited by the reaction taking place only on the surface of the negative electrode and not in the bulk solution. Nonetheless it remains an effective method to prepare thin films of rGO deposited on electrodes, for applications such as supercapacitors, batteries and sensors.

These approaches differ in terms of effectiveness (typically assessed in terms of C/O ratio and electrical conductivity [2]) and composition of the final products. Thermal deoxygenation usually induces more defects in GO than chemical reductions, since decomposition is catalyzed by the presence of previous defects. On the other side chemical reduction strategies leave the structure less defected, but usually are not able to remove oxygens as effectively as thermal decomposition and leave reaction byproducts. The two approaches are usually combined in order to exploit respective advantages: first GO is chemically reduced, removing most oxygens without additionally damaging the graphitic layer, then high-temperature thermal treatment (900°C - 1000°C) removes remaining oxygens and, as we mentioned above, partially heals broken C—C bonds. This combined approach typically yields high-quality rGO with high electrical conductivity, although not comparable to graphene in these terms [2]. Important steps toward obtaining chemically derived graphene were published by Eigler and coworkers in 2013 [1] whom produced minimally damaged GO by keeping reaction temperatures of a modified Hummers method below 10°C, therefore preventing the formation of defects during fabrication. They showed that chemical reduction yields rGO with very high carriers concentration (as high as $10^{12} cm^{-2}$) and carriers mobility (typically in the range $200 - 250 cm^2 V^{-1} s^{-1}$ but with some flakes exceeding $1000 cm^2 V^{-1} s^{-1}$. Another solution to produce high-quality rGO, proposed by Voiry and collaborators in 2016 [20], involves the use of microwave pulses to reduce GO obtained via the Hummers method

and repair defects in the basal plane. The authors obtained highly reduced GO with very low defectivity and high carriers mobility, inferring that microwaves cause a rapid heating of GO that induces oxygens desorption and a reordering of the graphitic lattice.

1.3 Structural models

Information about the composition of GO, given by Brodie and other early investigators based on combustion analysis, does not give any clue on the nature of the chemical bonding between oxygen, hydrogen atoms and graphitic carbons. It is not a sufficient representation of this material and a detailed structural model is fundamental to shine light on its properties and develop applications that involve GO.

Several model structures have been suggested for GO since it was first reported 165 years ago. In the first decades of the 20^{th}century, novel analytical tools such as XRD and IR spectroscopy were introduced allowing to determine crystalline structures of samples and investigate the nature of chemical bonds. In this period, research on GO moved from purely chemical investigations, such as combustion analysis, to more chemo-physical approaches and the first structural models became to appear. Among the first models introduced for GO, Thiele in 1930 [21] concluded that only hydroxyl groups (–OH) were present, adsorbed on both sides of a honeycomb carbon lattice (that today we call graphene). A completely opposite view was given by Hofmann et al in 1934 [18], claiming that GO was made of only epoxide groups (—O—) bridged between carbon atoms in a honeycomb lattice, based on results from the first ever application of XRD to GO. Both these models agree on GO being made of sp^2-hybridized carbon atoms in a honeycomb lattice (that today we identify as graphene), while they disagree on the nature of adsorbed species. An alternative model, published by Ruess et al in 1947, suggested a completely different view of GO basal plane, made of sp^3-hybridized carbon atoms, still in a honeycomb lattice but heavily corrugated, decorated with 1,3-ether species and –OH groups. Ruess based this model on a re-evaluation of the Hofmann's model and new XRD data. In 1969 Boehm and Scholz introduced a new structural model [22], based on the interpretation of IR spectra, where carbonyls and hydroxyls decorate the structure of GO and break C–C bonds. With the development of new investigation techniques, such as solid-state nuclear magnetic resonance (SSNMR) for the analysis of chemical species and high-resolution transmission electron microscope (HRTEM) for visualising details within atomic resolution, it became possible to validate or rule out aspects of previous models and new ones appeared. In 1998, Lerf et al published the results from their SSNMR measurements [23], and concluded that GO was amorphous, made of pristine sp^2-hybridized graphitic regions which were not oxidized during preparation and areas where oxygen-containing species were adsorbed. From SSNMR spectra they determined these species to be hydroxyls and epoxides (ruling out 1,3-ethers) in the basal plane, as shown in Figure 1.2, while suggesting the presence of carboxyl decorating the edges of the flakes. This representation became known as

the "Lerf-Klinowski" model for GO and gained a remarkable popularity after HRTEM images published in 2010 [24][25] confirmed the amorphous nature of the material and the presence of oxidized and unoxidized regions. Unfortunately even conclusions based on such sophisticated techniques may be ambiguous, and further studies gave different structural interpretations of their measures. According to Dimiev [2], concepts from both Ruess and Boehm-Scholz models were resurrected by Szabó and collaborators in 2006 [26], which proposed a representation of GO as a periodic structure of cyclohexane stripes, decorated with hydroxyls, 1,3-ethers, ketones and quinones in the presence of broken C—C bonds. Although one of the assumptions of the "Szabó-Dékány" model, the ordered and stoichiometric nature of GO, was ruled out by HRTEM images, also a widely accepted feature of the Lerf-Klinowski model, namely the presence of carboxyl groups at the edges, seems to be disproven in favor of carbonyls as predicted by the Szabó-Dékány model and discussed in Dimiev's book at Section 2.6 [2]. It is clear that a complete model for GO is still missing today, although research activities goes on largely based on assumptions from either the Lerf-Klinowski or Szabó-Dékány models. Given the heterogeneous composition of GO samples, its reactivity in water and unstable nature the introduction of an unambiguous model is very challenging and indeed these two models are consistent only for particular aspects of GO and ambient conditions. Neither the Lerf-Klinowski nor the Szabó-Dékány models, for example, account for the acidity of GO in water [2]. In order to address this deficiency of previous models, in 2012 Dimiev et al [27] introduced a new model for GO called "Dynamic structural model" (DSM) based on acidity related studies. This model, which can be seen in Figure 1.3, considers hydroxyls and epoxides as the predominant species on the basal plane, with enols and ketones in correspondence of C—C cleavage points (which are not considered as edges). It also suggests that these species are in constant evolution when in contact with water, forming hydronium cations (H_3O^+) that are ultimately responsible for the acidification of water.

1.4 Characterization

In this section we will review briefly the main characterization techniques that have been applied to study GO and the results obtained. The order in which they are presented tries to follow the historical evolution of GO research and consequently tends to be increasingly sophisticated and complex.

1.4.1 Optical Microscopy

The observation of GO flakes with an optical microscope was reported in the seminal paper by Brodie in 1859 [4]. In this paper, GO flakes are observed by mean of an optical microscope, described as "[...] perfectly transparent, and exhibit beautiful colors by the agency of polarized light" and their crystalline system speculated to be either

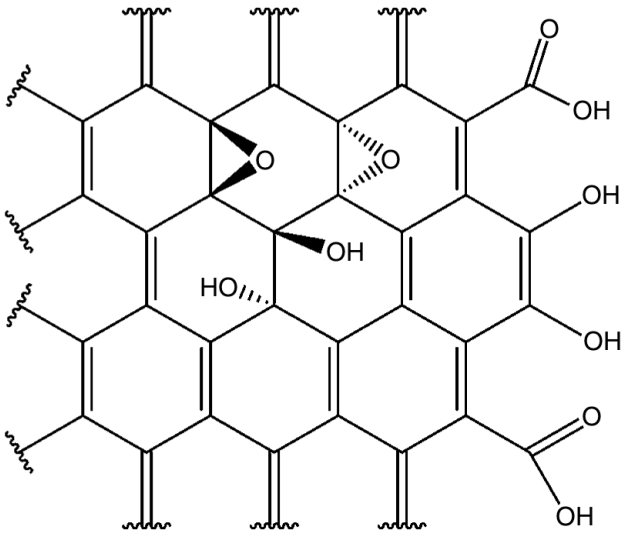

Figure 1.2: Lerf-Klinowski model representing the basal plane of GO (edges are not shown), where we can identify the hexagonal carbon layer with adsorbed epoxide and hydroxyl species in random positions. Figure reproduced from [2] with permissions from John Wiley and Sons.

prismatic or oblique. Nonetheless, given the typical dimensions of the flakes in the order of few micrometers, structural details of the sample remained invisible.

1.4.2 X-ray Diffraction

X-ray diffraction (XRD) was first reported applied to GO samples by Hofmann in 1928 [6]. XRD measurements are particularly suitable to investigate the interlayer distance between crystalline planes that constitutes graphite and the first intercalated stages obtained during GO fabrication. Indeed Hofmann et al, in the publication mentioned above, reported that the interlayer distance of graphite layers increased from 3.4Å to 8Å during reaction with a mixture of H_2SO_4 and HNO_3. XRD investigations have been used also to support the introduction of new models for GO [18] [27].

1.4.3 Infrared Spectroscopy

Fourier transform infrared spectroscopy (FTIR) is a fast and convenient investigation technique for GO. Although only a few bands can be assigned without ambiguities, with the information being essentially qualitative it provides interesting evidences regarding GO composition and environment [2]. According to Dimiev and Eigler [2], four distinctive bands are typically present in GO FTIR spectra (shown in Figure 1.4):

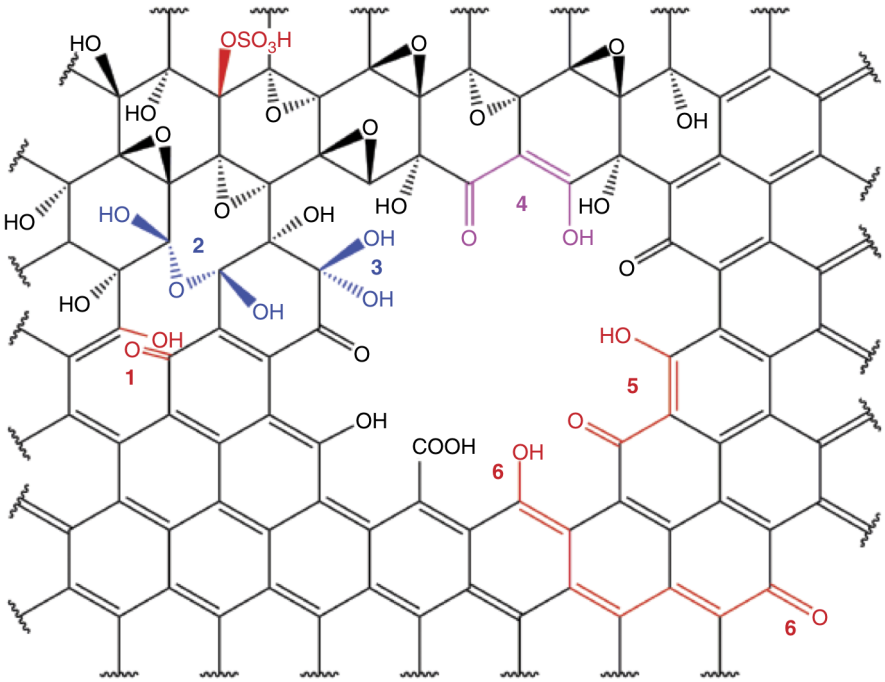

Figure 1.3: Dimiev-Tour dynamic model, considers epoxide and hydroxyl species in random positions as predominant in the basal plane. Points where C—C are cleaved (see point 1) are not considered as edges and are decorated with enols and ketones, whereas holes are decorated by enoles, ketones, carbonyls and carboxyls. Figure reproduced from [2] with permissions from John Wiley and Sons.

- 3600-2400 cm^{-1} band: corresponds to O—H bonds stretching; it may be due to OH groups in the structure or water molecules trapped within GO structure. Experiments with deuterated water (D_2O) demonstrated that this band is dominated by water molecules which are not strongly physisorbed [28] [26] [29].
- 1723 cm^{-1} peak: assigned to carbonyl groups.
- 1619 cm^{-1} peak: originates from bending modes of water molecules strongly physisorbed to GO, as demonstrated in [28] [26] [29] or hydroxyls.
- Fingerprint region: difficult to unambiguously assign due to the overlapping of bands from different functional groups.

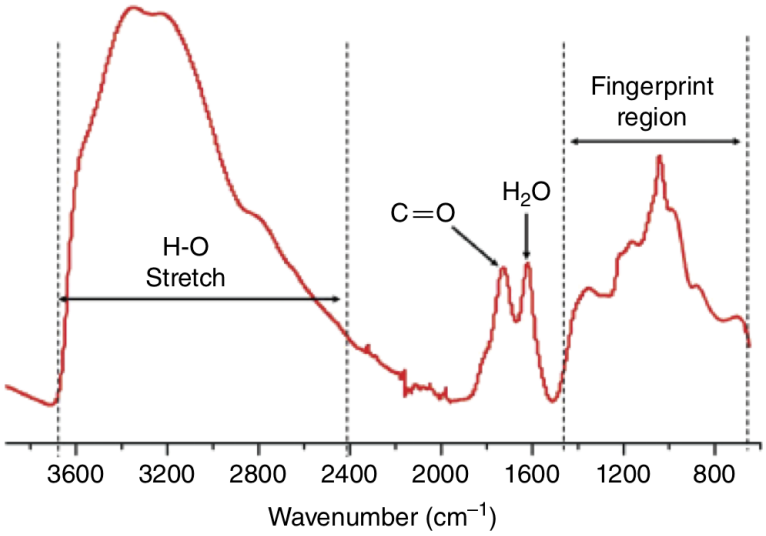

Figure 1.4: Typical FTIR spectrum of GO. It is possible to recognize four characteristic bands and peaks: 3600-2400 cm^{-1} band corresponds to O—H bonds stretching and is due to weakly-adsorbed water, 1723 cm^{-1} peak assigned to carbonyls, 1619 cm^{-1} peak assigned to bending modes of strongly physisorbed water and a fingerprint region whose contributions cannot be unambiguously identified. Figure reproduced from [2] with permissions from John Wiley and Sons.

1.4.4 X-ray Photoelectron Spectroscopy

X-ray photoelectron spectroscopy (XPS) is a very important characterization technique in the field of GO research since it provides quantitative information on the composition of the material, hence the percentage of different oxygen-containing species in the samples. The nature and relative content of these species is typically determined from the energy of different contributions to the C1s spectra and by the area beneath them. Thanks to these convenient features, XPS became a very popular method for GO investigations [2]. As we saw in the case of FTIR analysis it is possible to assign, with some confidence, different contributions and peaks in the XPS spectra (see Figure 1.5) to specific chemical environments in the samples. It is universally accepted that sp^2-hybridized C atoms give rise to the peak centered around 284.5 eV, while the peak centered around 286.5 eV is often attributed to epoxides and tertiary alcohols (i.e. –OH). A further component, usually around 288-289 eV likely originates from the superposition of carboxyl and carbonyl groups although there is scarce agreement in literature [2].

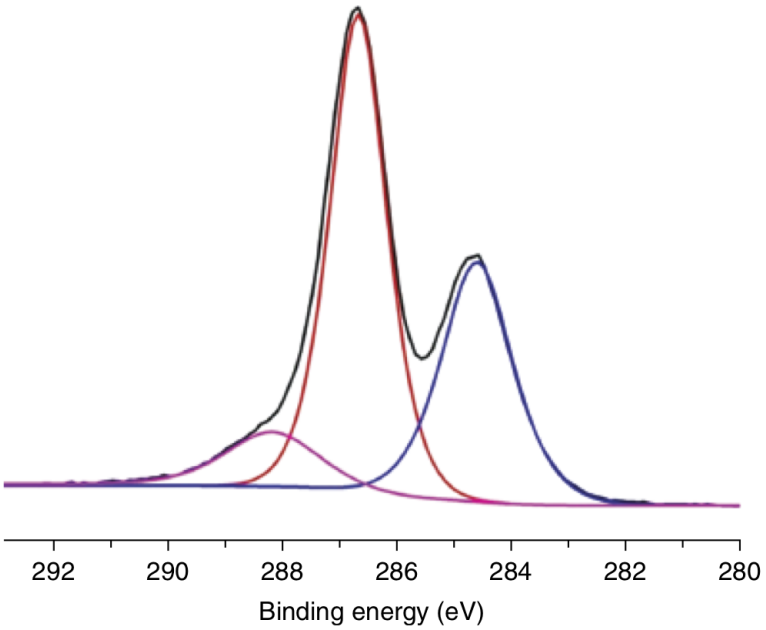

Figure 1.5: Typical XPS C1s spectrum of GO. The experimental spectrum of a GO sample is deconvoluted into three components: peak 284.5 eV assigned to sp^2 carbon atoms, peak 286.5 eV assigned to epoxide and hydroxyl groups, peak 288-289 eV that according to the authors probably originates from a superposition of carbonyl and carboxyl groups. Figure reproduced from [2] with permissions from John Wiley and Sons.

1.4.5 High Resolution Transmission Electron Microscopy

High resolution transmission electron microscopy (HRTEM) was first used for GO by Gómez-Navarro and coworkers in 2010 [24]. It became extremely important in the study of GO, thanks to its very high resolution that allows to discriminate details at the atomic scale. For the first time it was possible to visualize the atomic structure of GO and identify different characteristics and regions. The authors identified pristine graphitic areas where the hexagonal lattice was clearly observable. Intact regions, point defects (e.g. holes, substitutions, single adsorbed species) and vast oxidized areas that appeared amorphous were highlighted. They reported the size of the graphitic domains to be on average 3-6 nm, while the average area of defective domains to be around 1-2 nm. The same year also Erickson and collaborators published a similar study using HRTEM [25], an example of their acquisition is reported, together with inset on different regions (the same identified by Gómez-Navarro et al), is reported in Figure 1.6.

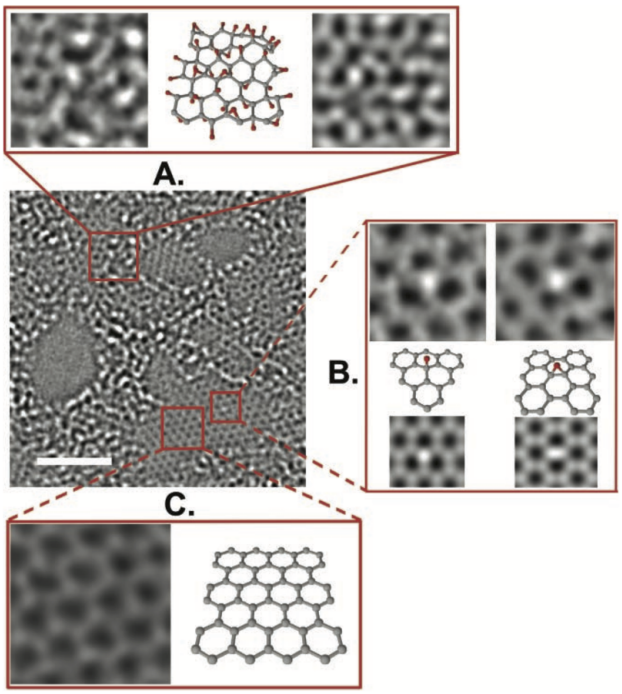

Figure 1.6: HRTEM image of single-layer suspended GO, with insets showing details and corresponding atomic models. Inset A focuses on a oxidized amorphous region, inset B shows an isolated point defect (probably an adsorbed epoxyde) and inset C represents a pristine graphitic region. Figure reproduced from [25] with permissions from John Wiley and Sons

1.4.6 Atomistic simulations

Atomistic simulations allow to model and characterize solid state and molecular systems across different physical scales: from sub-nanometric (e.g. DFT, classical and *ab initio* MD) to micrometric (e.g. large-scale MD and Monte Carlo techniques). In this thesis we focus on classical and quantum simulations at the atomic scale, which have the potential to shine light on fine structural and chemo-physical features of GO that are still ambiguous or missing in the literature. DFT and molecular dynamics have been successfully applied to study GO and its applications since many years but, despite these efforts, more computational work would be highly beneficial for the field. Classical molecular dynamics has been extensively employed for the investigation of technological applications of GO, such as in studying the use as single-layer membranes for water desalination [30] [31] (Figure 1.7 (a)), as well as to investigate water and ions diffusion through multilayer GO membranes [32] [33] [34] (Figure 1.7 (b)), gas separation [35] (Figure 1.7 (c)), electrostatic properties in presence of electrolytes [36] (Figure 1.7

(d)) and many others. On the other side, the study of the fundamental chemo-physical properties of GO by means of accurate quantum simulation techniques, such as DFT and *ab initio* MD, is less extensive in the literature. While many of these simulations provided important information on GO, such as considerations on the stability of different oxygen-containing species [37] [38], mechanisms for oxygen desorption [39] and defects formation [40], as well as approximate data on the electronic density of states [41], many of these works are usually based on simple model structures with high symmetry and few atoms [42] [43] due to prohibitive computational costs of large DFT simulations. These small models cannot fully grasp the complexity of an amorphous and meta-stable material such as GO. Accurate *ab initio* investigations on large and disordered structures, as the one employed in this thesis work, are needed to realistically study its properties and features.

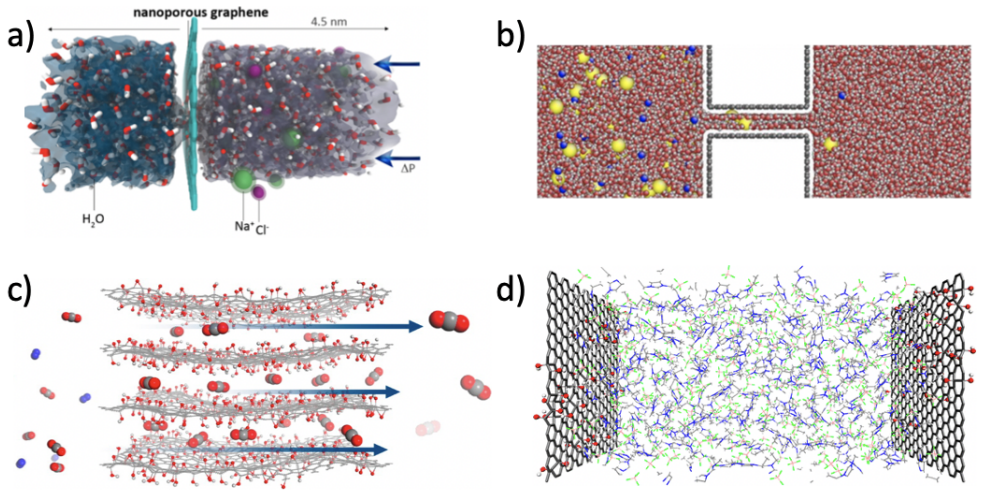

Figure 1.7: Examples of MD simulations used to model technological applications of rGO and graphene. In particular: a) simulation of water filtration through a single-layer porous membrane for water desalination (reproduced from [30] with permissions from ACS); b) simulation of solvated ions diffusion through multilayer GO membranes (reproduced from [32] with permissions from AAAS); c) application of multilayer rGO membranes for gas separation (reproduced from [44] with permissions from ACS); d) investigation of the electrostatic properties of rGO in presence of electrolytes (reproduced from [36] with permissions from ACS).

1.5 Applications

In the final section of this introductory chapter on GO, we review briefly some of the possible applications, proposed in scientific literature, that benefit from the use of GO

and rGO. These cover many fields of science and technology, from molecular sensors to electronic devices, from energy harvest and storage to filtration technologies, as a reminder of the versatility of this material.

1.5.1 Membranes for water desalination

Membranes play a relevant role in several industries nowadays, with major interest from the healthcare industry and growing applications in sectors such as water purification, gas separation and chemical synthesis. The use of membranes for industrial and widespread applications took about 200 years to develop, since first rudimental experiments in the eighteenth century using animal parts, essentially because membranes were unreliable, unselective, expensive and had very low permeation rates [45]. The development of ultrathin polymeric membranes with high permeability between 1960 and 1980, and their use to produce artificial kidneys, acted as a catalyzer for the application of membranes in industrial technologies. Among different separation techniques involving membranes, reverse osmosis (RO) is particularly suited for water purification since it allows lower energy consumption with respect to distillation. Given that global water consumption is projected to steeply increase in the next decades, while the fresh-water hydrogeological cycle is expected to be modified by global warming all over the world, the possibility to provide efficient and inexpensive desalination techniques to access sea and brackish water as a source of drinkable water, is crucial to mitigate suffering and death due to water shortages in the near future [46]. The process of RO involves forcing water to flow through a semi-permeable membrane, separating the feed stream into permeate and retentate phases, by mean of intense applied pressure. Currently, research is focused on increasing the permeability of RO membranes, while preserving selectivity, in order to reduce needed pressures and therefore the energy consumption of desalination plants.

Classic semi-permeable membranes, based on thin-film polymeric composites, typically offer low permeation fluxes (or in case of higher permeation, low selectivity) and are easily damaged when in contact with chlorine [46]. For what concerns water permeation fluxes, standard membranes nowadays range from about $10^1 \div 10^2\, L/(m^2 \cdot hr \cdot MPa)$ [46]. To reduce energy consumptions and costs of desalination, it is therefore necessary to introduce novel membrane concepts that allow for much higher water permeation fluxes. In this sense, in 2012 Cohen-Tanugi and collaborators suggested the use of nanoporous single layer graphene as an almost ideal RO membrane: strong, atomically-thin and resistant to chemical damages [30]. They concluded, based on results from MD simulations, that such RO membranes would have a very high theoretical water permeation flux, up to about $660000 L/(m^2 \cdot day \cdot MPa)$ which is about 3 or 4 order of magnitudes higher than commercial membranes.

Graphene is the thinnest material currently known and, since the water flux through a membrane is inversely proportional to its thickness, it can be considered as the natural choice to produce membranes with higher permeation rates. Moreover, defect-free

graphene is impermeable even to hydrogen and helium atoms, therefore it also promises very good selectivity [46]. The application of GO for the fabrication of graphene-based membranes for RO water desalination is frequent in scientific literature, for its easy fabrication and deposition that make it a suitable and cheap substitute of graphene [31] [32]. The presence of oxygen-containing species allows further degrees of freedom for tuning membrane characteristics, as we will see later in this section and in the following chapters.

There are currently two different approaches to fabricate GO membranes: monolayer membranes made of a large nanoporous single-layer GO flake and stacked multilayer membranes that exploit different diffusion rates through the narrow channels between GO flakes.

Monolayer GO membranes

As we already mentioned, perfect graphene is impermeable even to the lightest atomic elements due to its dense electron cloud that blocks permeation through aromatic rings [47]. The fabrication of sub-nanometric pores with uniform and controlled size would then allow very high and targeted selectivity based on size exclusion, as well as superior permeability performances. Molecular dynamics simulations of water desalination with ideal graphene nanoporous membranes predicted very high salt rejection (>99%) and extraordinary water fluxes (up to $660000 L/(m^2 \cdot day \cdot MPa)$) [30]. In Figure 1.8 is reported, as an example, a schematic representation of monolayer graphene membrane for RO desalination of water as published in [30]. GO presents further complications with respect to graphene for its application as monolayer membranes, mainly due to its intrinsic defectivity that result in the presence of holes with uncontrollable size in the graphitic plane. In this sense, fabrication methods that prevent the disruption of the carbon backbone and minimize the formation of defects, such as the one proposed by Eigler [1], offer an effective solution for the use of GO in this field. As we will see in Chapter 4, we demonstrated that it is possible to exploit the presence of oxygen-containing species to fabricate pores of uniform and controlled size in defect-free monolayer rGO.

Among several mechanisms involved in filtration by GO monolayer membranes, size exclusion is the most relevant, while dehydration effects and charge repulsion play an important, albeit less explicit, role. Size exclusion is determined by the size of ions in the feed being larger than membranes pore dimensions; to this extent it was determined that the optimal pores diameter to separate NaCl from water ranges between 6 Å and 8 Å [48]. Dehydration, on the other side, consists in the removal of water molecules from an ion's hydration shell when strongly confined, which is energetically unfavorable and prevents the diffusion of certain ionic species. The presence of epoxides and hydroxyls in GO complicates this aspect, in fact it is possible for oxygen-containing species decorating pores to partially replace water molecules in ions hydration shell and therefore

modify rejection properties. Finally, oxygen-containing groups in GO are usually ionized in water as negatively charged species, introducing further contributions to salt rejection due to electrostatic repulsion.

Beside numerous computational studies predicting impressive performances of monolayer graphitic membranes, several experimental works demonstrated the accuracy of theoretical predictions [49] [50] [51], although faced with non-trivial challenges such as the high fabrication costs of large-area monolayers, the presence of intrinsic defects after fabrication and technical difficulties in fabricating pores with controlled and uniform size. In Chapter 4 we will address this last challenge by suggesting a reliable and scalable two-steps treatment that allows to fabricate pores of uniform and controlled size in monolayer rGO.

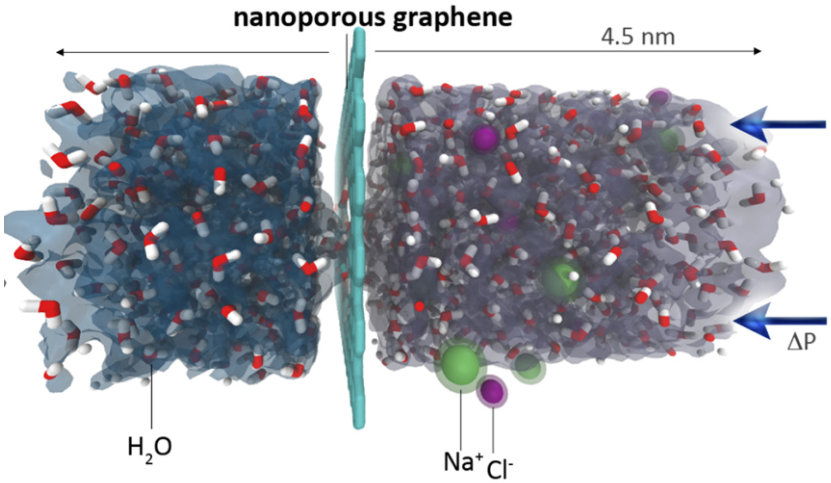

Figure 1.8: Schematic representation of a monolayer graphene membrane used for RO desalination of water. Figure reproduced from [30] with permissions from ACS.

Multilayer GO membranes

As we have seen, monolayer GO membranes still face relevant challenges to their experimental applicability. In particular, difficulties in fabricating large area defect-free GO with controlled and uniform pores pushed toward approaching different technological solutions that allow for the use of defected GO flakes. To this end, many publications demonstrated that the stacking of several GO monolayers produces free-standing membranes that prevent the solute from flowing through defects in singular layers and work well in RO application [2] [46]. These membranes are made of several GO monolayers orderly stacked, forming 2D nanochannels that allow the permeation of water molecules while rejecting other solutes, as shown in Figure 1.9. It was proved, by means

of MD simulations, that water molecules flow very fast parallel to pristine graphene regions in GO, whereas due to hydrogen bonding with oxygen-containing groups water molecules flow slower between oxidized areas [52]. The main separation mechanism in multilayer membranes is size exclusion, as in the case of monolayer ones, although this time it is the interlayer distance between GO sheets that determines the exclusion size. Nevertheless, dehydration plays a more relevant role than in monolayer membranes due to much higher surface exposure and consequent interaction with oxygen-containing groups, highlighting the importance of carefully investigating the chemo-physical properties of GO in water and the dynamics of ions under realistic conditions.

One of the main problems faced by multilayer GO is swelling in water, since increasing the interlayer distance has adverse effects on salt rejection [46]. In fact, dry GO presents an interlayer distance of about 6-7 Å which increases to 14 Å and more when soaked in water [52]. Swelling leads to dramatic problems for membrane filtration due to uncontrolled modifications of the interlayer distance that disrupt rejection capabilities. For example, for water desalination the interlayer spacing should not exceed 7 Å to reject Na^+ ions, but upon hydration the interlayer distance of GO can grow fast up to 14 Å (membranes may even delaminate completely in some circumstances). To face these challenges, the research community explored different ways to suppress or reduce swelling in GO multilayer membranes, typically involving reduction treatments or cross-linking with small molecules [53]. Reduction of GO, by removing oxygen-containing species and therefore promoting $\pi - \pi$ interactions between pristine graphene areas in stacked layers, shrinks the interlayer distance and increases membranes stability. Cross-linking instead is based on the insertion of small molecules (e.g. boric acid [54]) or nanoparticles between stacked GO layers and is typically achieved with layer-by-layer deposition. It exploits the binding between GO layers and cross-linkers to fix the interlayer distance (according to the dimensions of the chosen cross-linker, hence it is possible to tune this distance) when membranes are soaked in water, therefore preventing swelling and preserving salt rejection and water permeability.

In Chapter 5 we will discuss the physics of interactions between rGO layers and water in the context of multilayer membranes, based on results from a thorough *ab initio* MD investigation. We analyzed the properties of water confined between rGO layers in terms of distribution, polarization and diffusivity, as well as modifications induced by water to rGO. These results will hopefully improve our knowledge of the mechanisms controlling water diffusion and salt rejection in GO multilayer membranes, as well as assist in choosing the right rGO composition and interlayer distance to optimize desalination performances.

1.5.2 Electrodes

As we discussed in Section 1.2.3, following the deoxygenation of GO to rGO we obtain a quasi-metallic material with relatively high conductivity and carrier mobility. Good conductivity together with good transparency in the visible range make rGO a

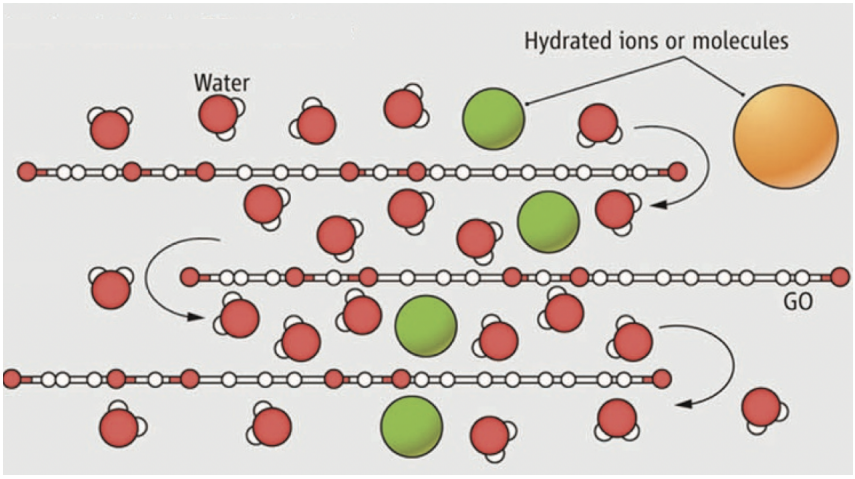

Figure 1.9: Schematic representation of a multilayer GO membrane used for RO desalination of water. Figure reproduced from [55] with permissions from AAAS.

suitable candidate for the fabrication of Transparent Conductive Electrodes (TCE). TCEs are of fundamental importance for the production of optoelectronic devices such as LEDs and displays, as well as photovoltaic and photo-electrochemical cells. Nowadays, Indium-Tin-Oxide (ITO) is the most used material for the production of TCEs, although its lack of flexibility and the high cost of indium is pushing research toward its substitution [56]. Graphene, which is flexible, conductive and transparent, showed promising results when substituting ITO in photovoltaic cells, LEDs, touch screens and optoelectronic devices [57]. Different strategies have been employed to fabricate TCEs using rGO, all of them involve a trade-off between conductivity (which increases with thickness) and transparency (which decreases with thickness). Typically GO is deposited on a substrate and then deoxygenated (either thermally or by chemical reduction) to improve its conductivity. In this sense different approaches have been suggested in literature, such as chemical doping, hybridization with carbon nanotubes and the use of large-area flakes that demonstrated better conductivity than smaller sized flakes [58]. The characteristics that make rGO a good candidate to produce TCEs also make it an interesting option to be used in photovoltaic technologies. Graphene-like materials have already been used in a variety of solar cells, among them we find dye-sensitized solar cells (DSSC), thin-film cells as well as attempts of integration within conventional silicon cells. In the literature we also find attempts to use graphene and rGO not as TCE but as counter-electrode, holes conductor, semiconducting layer and even as sensitizer (in DSSC) [57] [59] [2].

Another field where attempts to use graphene and rGO showed promising results is that of energy storage, in particular for the fabrication of batteries and supercapacitors electrodes. Lithium-ion batteries are typically built using a graphite anode, a liquid electrolyte and a lithium cobalt oxide ($LiCoO_2$) cathode, therefore attempts to use graphene

and rGO as anodic material are numerous in scientific literature [60] [61].

1.5.3 Field Effect Transistors

A Field Effect Transistor (FET) is an electronic device that allows to control the flow of electric current through its channel by means of an applied electric field. It usually consists of two electrodes (source and drain) through which electrons flow and a third electrode (gate) that controls this flux. Graphene is an excellent candidate to replace silicon in these devices, given its high mobility and the possibility to tune its conductivity with an electric field [12]. A gap can be opened in its electronic band structure by lateral confinement (cutting nanoribbons) as well as by doping and oxidation. Reduced GO was also successfully used for the fabrication of FET by depositing metal electrodes on top of a GO film after it was reduced with hydrazine [62]. The authors showed that the resistance of the GO film decreased by 4 orders of magnitude upon reduction to rGO and I/V curves showed a semiconducting behavior.

1.5.4 Sensors

GO is of great importance for sensors technology, deoxygenated to exploit its good conductivity and mechanical strength or as-produced to exploit its reactive oxygen-containing species [63] [64]. Graphene based sensors are usually investigated in scientific literature to sense gas (e.g. NO_2, CO, alcohols and ammonia) or moisture and they typically deal on modifications of conductivity upon the adsorption of target molecules to detect their presence. Solution processed rGO has been often studied as a cheap replacement of CVD graphene in sensors but, differently from this latter, the oxygen-containing groups in its structure interact with the environment and possibly enhance sensitivity to target molecules [64]. In this sense, much attention has been devoted to control and tailor the oxidation degree of GO flakes in order to improve sensors efficiency [65].

In this doctoral thesis we will not address direct applications of rGO as electrodes, sensors or FET, nonetheless our results may be relevant to support further investigations in these fields. In fact we reported results that highlight general properties of rGO, relevant to electronic and optical applications. For example, we discussed the effects of different oxygen-containing species on the valence band properties and provided indications on the energy band gap of rGO as a function of its stoichiometry.

Chapter 2

Simulation methods

2.1 Introduction

In this chapter we review the basic concepts of the simulation techniques used to model and investigate the properties of rGO. First we recall the founding concepts of DFT, introducing the two Hohenberg-Kohn theorems [66] and the Kohn-Sham approach [67] that allow to recast the many-electrons problem describing an atomic system, as a set of one-particle Schrödinger-like equations. We will review the use of atomic-centered basis sets and of planewaves formalism to solve the electronic structure problem of a solid-state system and finally discuss some of the available approximations to model the contribution of quantum exchange and correlation on the total energy of the system.

In the second section, we will discuss how the dynamical evolution of a system can be obtained by means of MD. The computation of interatomic forces, fundamental for a correct description of atomic movements, can be achieved either applying analytical interaction models (classical approximation) or by using DFT to describe these interactions *ab initio* (quantum description). We will review both approximations, with particular focus on the Car-Parrinello implementation of *ab initio* MD that we most frequently used in our investigations.

Finally, we will introduce CE, a useful technique to predict the stability of possible species arrangements in heterogeneous material, that we used to study preferential configurations of epoxide clusters, and KMC that we used to investigate the slow diffusion of epoxides in rGO at room temperature.

2.2 Density Functional Theory

It is possible to predict the chemo-physical properties of a system of N interacting particles (e.g: electrons and atoms in a crystal), by solving the Schrödinger equation for that system. Indeed, knowing the solutions of the Schrödinger Equation, it is possible

to predict all the properties of a material.

Unfortunately, solving the Schrödinger Equation is a cumbersome task and its exact analytical solution remains possible only for the hydrogen atom. As a first simplification to describe the quantum properties of a condensed system, it should be considered that the nuclei are much heavier than the electrons, so that they can be considered "frozen" by the point of view of the electrons. This is the adiabatic approximation, which implies that the nuclei have zero kinetic energy since their interaction is constant ($|\boldsymbol{R_A} - \boldsymbol{R_B}|$ being constant). Using atomic units, the Hamiltonian within the adiabatic approximation for the system can be written as:

$$\hat{H} = -\frac{1}{2}\sum_i \nabla_i^2 + \frac{1}{2}\sum_i \sum_{j\neq i} \frac{1}{|\boldsymbol{r_i} - \boldsymbol{r_j}|} - \sum_A \sum_i \frac{1}{|\boldsymbol{r_i} - \boldsymbol{R_A}|} \tag{2.1}$$

whose terms are respectively the kinetic energy of the electrons, the electron-electron repulsion and the attraction between electrons and nuclei. Capital letters are used to indicate quantities relative to nuclei and lower-case letters for quantities related to the electrons.

To define the simulation domain, proper boundaries conditions must be applied according to the dimensionality of the system. To treat samples that are extended in space, periodic boundary conditions (PBC) are applied so that the system is modeled as infinite. In this case when a particle reaches one end of the boundary, it exits the simulation domain and it simultaneously re-enters from the opposite boundary, rather than being reflected.

Density Functional Theory lays its foundations on two theorem published by Hohenberg and Kohn in 1964 [66]. The *first Hohenberg-Kohn theorem* states that for any system of interacting particles (as described by the Hamiltonian in Equation 2.2), the external potential $V_{ext}(\boldsymbol{r})$ is determined uniquely, except for a constant, by the ground state particle density $n_0(\boldsymbol{r})$. It follows that since the Hamiltonian is fully determined, also the many-body wavefunctions for all the states are determined:

$$\hat{H} = -\frac{1}{2}\sum_i \nabla_i^2 + \sum_i V_{ext}(\boldsymbol{r_i}) + \frac{1}{2}\sum_{i\neq j} \frac{1}{|\boldsymbol{r_i} - \boldsymbol{r_j}|} \tag{2.2}$$

The *second Hohenberg-Kohn theorem* states that there exists a universal functional of the energy in terms of the density, which is valid for every V_{ext}. For any particular potential, the exact ground state energy of the system is the global minimum of this energy functional, while the exact ground state density $n_0(\boldsymbol{r})$ is the one that minimize it:

$$E^{HK}[n] = T[n] + V[n] = T[n] + E_{int}[n] + E_{ext}[n] = F_{HK}[n] + E_{ext}[n] \tag{2.3}$$

$T[n]$ is the kinetic energy of the particles in the interacting many-body system, $E_{int}[n]$ is the energy due to the interactions between the electrons in the system, while $E_{ext}[n]$

represents the contribution due to the interactions between electrons and nuclei. The universal functional F_{HK} includes all the internal energies of the system (kinetic and potential). In order to find the ground state energy of the system, $E[n]$ must be minimized with respect to the density, considering also a constraint on the total electronic density ($\int n(\boldsymbol{r})d\boldsymbol{r} = N$, N being the number of electrons in the system) introduced with the Lagrange multipliers method:

$$\frac{\partial}{\partial n}\left\{ E[n] - \mu(\int n(\boldsymbol{r})d\boldsymbol{r} - N)\right\} = 0 \tag{2.4}$$

An explicit proof of both theorems can be found in the original paper from Hohenberg and Kohn [66].

If the energy functional $F_{HK}[n]$ was known, then minimizing the total energy with respect to the density would yield the exact ground state energy and density of the interacting many-body system. Unfortunately the analytical form of this functional is undetermined. The approach proposed by Kohn and Sham in 1965 to this problem [67], is to replace the unpractical interacting many-body system, with an auxiliary system made of non-interacting particles and therefore easier to treat. This auxiliary system leads to Schrödinger-like independent-particle equations which have all the many-body contributions incorporated into an exchange-correlation functional of the energy. These equations are in principle exact, with accuracy limited only by the approximations of the exchange-correlation functional.

The Kohn-Sham approach is based on two assumptions:

- The exact ground-state density can be represented by the ground-state energy of an auxiliary system of non-interacting particles.
- The auxiliary hamiltonian is chosen to have the usual kinetic energy operator and an effective local potential $V_{eff}^{(\boldsymbol{r})}$ acting on an electron of spin σ at position $\boldsymbol{r}$:

$$\hat{H}_{aux} = -\frac{1}{2}\nabla^2 + V(\boldsymbol{r}) \tag{2.5}$$

Based on these premises, the expression for the ground-state energy functional introduced with Equation 2.3 is restated as:

$$E^{KS}[n] = T_S[n] + E_{ext}[n] + E_{Ha}[n] + E_{XC}[n] \tag{2.6}$$

where $T_S[n]$ is the kinetic energy of the particles in the fictitious non-interacting system (different from $T[n]$ in Equations 2.3 which is the kinetic energy in the original interacting system), E_{ext} is the contribution due to the interaction between electrons and nuclei, E_{Ha} refers to classical Coulomb interactions between electrons and E_{XC} takes into account all the many-body effects (correlation and exchange).

It follows from the first assumption of the Kohn-Sham approach that at ground-state the following must be:

$$E^{HK}[n_0] = E^{KS}[n_0]$$

$$T_S[n_0] - T[n_0] + E_{ext}[n_0] - E_{ext}[n_0] + E_{Ha}[n_0] + E_{XC}[n_0] + E_{int}[n_0] = 0$$

$$E_{XC}[n_0] = T[n_0] - T_S[n_0] + E_{int}[n_0] - E_{Ha}[n_0] \tag{2.7}$$

It is clear that E_{XC} takes into account every dissimilarities between the original interacting many-body system and the auxiliary non-interacting one, considering difference of kinetic energy between the two systems, as well as in terms of electron-electron interactions. Unfortunately there are no exact definitions for E_{XC} but this term can be approximated using different techniques.

All contributions to Equation 2.6, but the exchange and correlation energy, can be explicitly expressed:

$$T_S = -\frac{1}{2}\sum_{i=1}^{N_{occ}} < \psi_i(\boldsymbol{r})|\nabla_i^2|\psi_i(\boldsymbol{r})) >$$

$$E_{ext}[n] = \int V_{ext}(\boldsymbol{r})n(\boldsymbol{r})d\boldsymbol{r}$$

$$E_{Ha}[n] = \frac{1}{2}\int\int \frac{n(\boldsymbol{r})n(\boldsymbol{r}')}{|\boldsymbol{r}-\boldsymbol{r}'|}d\boldsymbol{r}d\boldsymbol{r}'$$

To derive the ground-state energy and density of the system, the Kohn-Sham energy functional must be minimized with respect to the density, according to the second Hohenberg-Kohn theorem:

$$\frac{\partial E^{KS}[n]}{\partial n} = 0, \quad \text{with constraint: } \int n(\boldsymbol{r})d\boldsymbol{r} = N \tag{2.8}$$

Since the kinetic energy is expressed in terms of wavefunctions while other terms are functions of the density, we apply the chain rule to derive the variational equation:

$$\frac{\partial E^{KS}[n]}{\partial \psi_i^*} = \frac{\partial T_S}{\partial \psi_i^*} + \left(\frac{\partial E_{ext}}{\partial n} + \frac{\partial E_{Ha}}{\partial n} + \frac{\partial E_{XC}}{\partial n}\right)\frac{\partial n}{\partial \psi_i^*} = 0 \tag{2.9}$$

Equation 2.9 yields the so called Kohn-Sham equations, which have the form of single-particle Schrodinger-like equations.

$$\hat{H}_{KS}\psi_i(\boldsymbol{r}) = \varepsilon_i\psi_i(\boldsymbol{r}) \tag{2.10}$$

where

$$\hat{H}_{KS} = -\frac{1}{2}\nabla^2 + V_{ext}(\boldsymbol{r}) + V_{Ha}(\boldsymbol{r}) + V_{XC}(\boldsymbol{r}) \tag{2.11}$$

When solving the Kohn-Sham (KS) equation, the energy functional depends on the electronic density of the system, which is itself unknown. Therefore, to practically solve the equation, a numerical procedure called Self-Consistent Field (SCF) must be applied. The SCF algorithm starts from an initial guess for the electronic density, successively solving the KS equation while changing the effective potential and density to approach a self-consistent result.

2.2.1 Exchange and correlation functionals

The Kohn-Sham approach separates independent particle kinetic energy and electrostatic terms from the exchange-correlation energy functional, into which is contained all the complexity of electron-electron interactions arising from the original many-body system. The exchange-correlation functional $E_{XC}[n]$ can be defined in first approximation as a local functional of the density, such that can be expressed as:

$$E_{XC}[n] = \int n(\boldsymbol{r})\epsilon_{XC}([n], \boldsymbol{r})d\boldsymbol{r} \tag{2.12}$$

$\epsilon_{XC}([n], \boldsymbol{r})$ is the energy per electron at point $\boldsymbol{r}$ which comes from the *exchange-correlation hole's* definition.

If we consider a system of uncorrelated particles, the probability to find a particle of spin σ at position $\boldsymbol{r}$ is $n(\boldsymbol{r}, \sigma)$, the probability to find another particle of spin σ' at position $\boldsymbol{r}'$ is $n(\boldsymbol{r}', \sigma')$, while the joint probability is simply the product $n(\boldsymbol{r}, \sigma) \cdot n(\boldsymbol{r}', \sigma')$. If the particles were correlated instead, the joint probability would be $n(\boldsymbol{r}, \boldsymbol{r}', \sigma, \sigma')$. A measure for correlation is then:

$$\Delta n(\boldsymbol{r}, \boldsymbol{r}', \sigma, \sigma') = n(\boldsymbol{r}, \boldsymbol{r}', \sigma, \sigma') - [n(\boldsymbol{r}, \sigma) \cdot n(\boldsymbol{r}', \sigma')]$$

The exchange between particles takes into account Pauli's exclusion principle, as well as self-interaction of electrons. When we consider exchange and correlation, the result is a lowering of the total energy with respect to the case in which we neglect them. It is possible to think of this energy lowering as the interaction between each electron with a positive exchange-correlation hole that surrounds it:

$$n_{XC} = n_X(\boldsymbol{r}, \boldsymbol{r}', \sigma, \sigma') + n_C(\boldsymbol{r}, \boldsymbol{r}', \sigma, \sigma')$$

Kohn and Sham pointed out that often solids can be approximated as an homogeneous electron gas, for which the effects of exchange and correlation have local character. They proposed the Local Spin Density Approximation (LSDA) for which E_{XC} is the integral over all space with ϵ_{XC} at each point assumed to be the same as in a homogeneous electron gas with the same density. In the case of unpolarized system the LSDA becomes simply LDA. Equation 2.12 becomes:

$$E_{XC}^{LDA}[n] = \int n(\boldsymbol{r})[\epsilon_X^{hom}([n], \boldsymbol{r}) + \epsilon_C^{hom}([n], \boldsymbol{r})]d\boldsymbol{r} \tag{2.13}$$

The only information needed are the exchange energy density and correlation energy density, the first has a simple analytical form (reported in Chapter 5 of [68]) while the latter can be calculated with great accuracy using Monte Carlo methods [69].

The accuracy of LDA is usually good for solids whose electrons are close to a homogeneous electron gas (e.g. metals) and worse for inhomogeneous cases (e.g. surfaces), one should always test the validity to the specific application with respect to experimental observables. The most obvious failure of LDA is due to the self-interaction term that, differently from the Hartree-Fock approximation, is only partially cancelled due to the fact that exchange is considered locally. LDA typically underestimates the energy gap of insulator materials.

In order to fix the deficiencies of LDA, in particular for those cases with highly nonuniform densities (e.g. atoms and molecules), Generalized-Gradient Approximations (GGAs) have been developed. These methods consider also the gradient of the density (∇n) as a contribution to E_{XC} which then becomes:

$$E_{XC}^{GGA}[n] = \int n(\boldsymbol{r})\epsilon_{XC}[n(\boldsymbol{r}), \nabla n(\boldsymbol{r})]d\boldsymbol{r} \tag{2.14}$$

Several GGA functionals have been proposed, among them we recall the forms of Becke (B88) [70], Perdew-Wang (PW91) [71] and Perdew-Burke-Ernzerhof (PBE) [72].

It turns out that GGAs typically lead to a lower exchange energy with respect to LDA, in particular in the case of atoms. For example, GGAs correct the over-binding of LDA for adsorbed atoms on a surface, improving the agreement with experiments. Nevertheless, GGAs also describe the electronic properties of some atomic systems, such as the energy gap of insulators, with limited accuracy.

A further class of exchange-correlation functionals has been introduced considering that while DFT treats well correlation effects, on the other hand the Hartree-Fock approximation provides an exact description of the exchange contribution. Hybrid functionals have been introduced by Becke [73] who proposed to use an energy functional for exchange and correlation that takes advantages from both theories, combining contributions to the exchange from Hartree-Fock and contributions to correlation from DFT:

$$E_{XC} = \frac{1}{2}\left(E_X^{HF} + E_C^{DFT}\right) \tag{2.15}$$

where the correlation contribution may come from either LDA or GGA functionals. Numerous hybrid functionals have been introduced, with different parameters and hybridizations between HF and DFT.

In this thesis work we used the PBE functional [72] (a kind of GGA functional) to perform *ab initio* MD and to analyze structural and dynamical properties of rGO in Chapters 4 and 5, while we used B3LYP to investigate the electronic properties of rGO in Chapter 3. This latter usually provides better predictions of excitation energies with

respect to LDA or GGAs and usually a more accurate description of overall electronic properties [74]. B3LYP exchange-correlation functional is defined as:

$$E_{XC}^{B3LYP} = E_{XC}^{LDA} + a_0(E_X^{HF} - E_X^{LDA}) + a_X(E_X^{GGA} - E_X^{LDA}) + a_C(E_C^{GGA} - E_C^{LDA}) \quad (2.16)$$

where $a_0 = 0.20$, $a_X = 0.72$, $a_C = 0.81$, E_X^{GGA} and E_C^{GGA} are respectively the B88 [70] exchange functional and Lee-Yang-Parr (LYP) [75] correlation functional.

B3LYP has been used with success to perform DFT calculations on graphene and functionalized graphene, to calculate adsorption energy for catalysis [76] and to compute the electronic properties of graphene oxide [77].

2.2.2 Electron wavefunctions representation

In order to numerically solve the Kohn-Sham equation (2.10), the single-electron wavefunction $\psi_i(\boldsymbol{r})$ is usually expanded using a complete basis set, and written as:

$$\psi_i(\boldsymbol{r}) = \sum_{j=1}^{\infty} c_j \phi_j(\boldsymbol{r}) \quad (2.17)$$

where $\phi_j(\boldsymbol{r})$ are the known components of a complete set of functions. Clearly, it is practically impossible to deal with an infinite number of functions, therefore the sum must be truncated to a finite number of elements, introducing a source of numerical error.

The choice of the basis set is arbitrary and the known components $\phi_j(\boldsymbol{r})$ are often chosen to be either localized atomic-like orbitals or planewaves. To perform DFT simulations on rGO models, as we will see in the next chapters, we used both approaches.

Localized basis set representation

In Chapter 3 we performed DFT calculations with CRYSTAL14 [78] using basis sets of localized orbitals centered on nuclei. This approach allowed us to obtain a full description of the atomic orbitals, from core to valence electrons, that we further exploit to simulate XPS spectra.

Different functions can be used to model atomic orbitals, most frequently Slater-type functions (SF) or Gaussian functions (GF); for example in the case of a 1s orbital, centered on the nucleus in position $\boldsymbol{R_A}$, they are defined as:

- 1s Slater-type function: $\phi_{1s}^{SF}(\zeta, \boldsymbol{r} - \boldsymbol{R_A}) = \left(\frac{\zeta^3}{\pi}\right)^{1/2} e^{-\zeta|\boldsymbol{r}-\boldsymbol{R_A}|}$
- 1s Gaussian-type function: $\phi_{1s}^{GF}(\alpha, \boldsymbol{r} - \boldsymbol{R_A}) = \left(\frac{2\alpha}{\pi}\right)^{3/4} e^{-\alpha|\boldsymbol{r}-\boldsymbol{R_A}|}$

The orbital exponents (α or ζ) determine the diffuseness of the basis: a large exponent provides a small dense function, while a small exponent yields a large and diffuse orbital. These two different kind of orbitals have complementary advantages and drawbacks: while Slater functions describe with better accuracy features of molecular orbitals than Gaussian functions, the latter allow faster calculations. In order to take advantage from both worlds, we use basis set of contracted Gaussian functions (CGF), approximating Slater-like orbitals as linear combinations of Gaussian primitives:

$$\phi^{CGF}(\boldsymbol{r}-\boldsymbol{R_A}) = \sum_{k=1}^{L} d_k g_k(\alpha_k, \boldsymbol{r}-\boldsymbol{R_A}) \tag{2.18}$$

where d_k and α_k are respectively the expansion coefficients and exponents, and g_k are the Gaussian primitive functions (of type 1s, 2p, 3d, ...):

$$g_{1s} = \left(\frac{8\alpha^3}{\pi^3}\right)^{1/4} e^{-\alpha(\boldsymbol{r}-\boldsymbol{R_A})^2}$$

$$g_{2p_x} = \left(\frac{128\alpha^5}{\pi^3}\right)^{1/4} x e^{-\alpha(\boldsymbol{r}-\boldsymbol{R_A})^2}$$

$$g_{3d_{xy}} = \left(\frac{2048\alpha^3}{\pi^3}\right)^{1/4} xy e^{-\alpha(\boldsymbol{r}-\boldsymbol{R_A})^2}$$

Usually contraction parameters are determined from results of atomic SCF calculations: starting from a large un- contracted set of Gaussian functions, the coefficients and exponentials are optimized for every atomic orbital.

Minimal STO-LG (Slater-Type Orbitals of L contracted gaussians) basis sets are computationally inexpensive, having the minimum number of functions to describe occupied atomic orbitals. They do not provide accurate results, though they are useful to gain a qualitative view of the properties of the system. They use contractions of L primitive Gaussians to describe each basis function:

$$\phi_{1s}^{CGF} = \sum_{k=1}^{L} d_{k,1s} g_{1s}(\alpha_{k,1s})$$

$$\phi_{2s}^{CGF} = \sum_{k=1}^{L} d_{k,2s} g_{1s}(\alpha_{k,2sp})$$

$$\phi_{2p}^{CGF} = \sum_{k=1}^{L} d_{k,2p} g_{2p}(\alpha_{k,2sp})$$

where the contraction coefficients are obtained approximating Slater functions using a least-squares fit

Double-zeta basis sets use two functions for each minimal basis function (e.g. for ϕ_{1s} they use ϕ'_{1s} and ϕ''_{1s}). The two functions have exponents that are slightly below

and slightly above the optimal exponents of the relative basis function; this allow to effectively contract or expand the orbital changing linear parameters. Double-zeta basis sets also give a further degree of anisotropy with respect to STO-LG basis sets for what it concerns p and d orbitals.

Polarized basis sets are double-zeta which add p-type functions to hydrogen atoms and d-type functions to first-row atoms of the periodic table. These fictitious orbitals (which are not occupied in the specified atoms) allow to take into account asymmetries arising from electric fields and non-spherical environments (non- isolated atoms).

Plane waves representation and the pseudopotential approach

For all DFT simulations reported in Chapter 4 and 5 of this thesis we used a plane waves description for the electron wavefunctions, with ultrasoft pseudopotential approximation for core electrons, as implemented in Quantum Espresso [79].

Plane waves are well suited to represent the electron wavefunctions in ordered solid crystals, for which periodic boundary conditions can be applied. Since any periodic function can be expanded as a complete basis set of Fourier components, each eigenfunction of the Schrödinger equation in a periodic crystal of volume Ω can be written, in the reciprocal space, as:

$$\psi_i(\boldsymbol{r}) = \sum_{\boldsymbol{k}} c_{i,\boldsymbol{k}} \cdot \frac{1}{\sqrt{\Omega}} e^{i\boldsymbol{k}\cdot\boldsymbol{r}} = \sum_{\boldsymbol{k}} c_{i,\boldsymbol{k}} \cdot |\boldsymbol{k}\rangle \tag{2.19}$$

where $c_{i,\boldsymbol{k}}$ are the expansion coefficients in the basis set of orthonormal plane waves $|\boldsymbol{k}\rangle$ satisfying $\langle \mathbf{k}' | \mathbf{k} \rangle = \delta_{\boldsymbol{k}'\boldsymbol{k}}$.

In this formalism, the Schrödinger equation can be restated as a matrix equation, defining $\boldsymbol{q} = \boldsymbol{k} + \boldsymbol{G}$ and $\boldsymbol{q}' = \boldsymbol{k} + \boldsymbol{G}'$ that differ only by a reciprocal lattice vector $\boldsymbol{G}$:

$$\psi_i(\boldsymbol{r}) = \sum_{q'} H_{q,q'}(\boldsymbol{k}) c_{i,q'}(\boldsymbol{k}) = \epsilon_i(\boldsymbol{k}) c_{i,q}(\boldsymbol{k}) \tag{2.20}$$

By using the Bloch theorem, it is possible to rewrite the eigenvalues of the Schrödinger equation as products of plane waves ($e^{i\boldsymbol{k}\cdot\boldsymbol{r}}$) and periodic functions $u_{i,\boldsymbol{k}}(\boldsymbol{r})$, with the same periodicity as the crystal and orthonormal in the primitive zone. In principle, an infinite number of plane waves would be needed to exactly represent electron wavefunctions, but for computational reasons this summation must be truncated to a reasonable value. The number of plane waves in the expansion of the electronic wavefunctions, is truncated to include plane waves with energy up to a pre-defined cut-off (E_{cut}).

The idea behind the use of pseudopotentials, is to replace the Coulomb potential of the nucleus and the effects of the core electrons with an effective potential acting on the valence electrons. Since core electrons have wavefunctions with closely spaced nodes in the reciprocal space, they need to be expanded using high-energy plane waves and therefore require a high cut-off energy which translates into a large number of plane waves. Using pseudopotentials, core electrons are substituted with an average ionic

potential allowing the use of lower cut-off energies and reducing the computational cost. For all DFT simulations based on plane waves, we used ultrasoft pseudopotentials to further reduce computational costs while maintaining reasonable accuracy. Ultrasoft pseudopotentials are built to produce very smooth pseudofunctions that allow the use of lower energy cut-offs with respect to norm-conserving pseudopotentials (that are considered the benchmark of pseudopotentials accuracy).

2.2.3 Reciprocal space integration and sampling of the k-points

In the case of periodic structures, the physical quantities of interest are calculated integrating over allowed $\boldsymbol{k}$ vectors within the Brillouin Zone (BZ). Since it is not possible to practically compute an integral over infinite points, a suitable way to sample the BZ must be introduced. Typically a Monkhorst-Pack grid [80] is used, which consists of a mesh of equally spaced points along the three reciprocal space primitive vectors. It is defined by three integers (n_x, n_y, n_z) which represent the number of sampling points along each direction in the reciprocal space.

The number of points to be used for the grid strictly depends on the characteristics of the system under treatment. Usually convergency tests are performed in order to choose the best grid in terms of accuracy and computational cost.

2.3 Molecular Dynamics

The main goal of MD is to model the evolution of an atomic system made of N particles (nuclei), simulating the motion of atoms according to Newtonian equations of motion.

$$\frac{d^2\boldsymbol{r_i}}{dt^2} = \frac{\boldsymbol{f_i}(t)}{m_i}, \quad i = 1..N \tag{2.21}$$

After defining a discrete time grid, with spacing dt, to sample the evolution of the system, positions and velocities can be expanded as a second-order Taylor series, allowing to compute their values at successive time steps.

$$\begin{cases} \boldsymbol{r}(t+dt) = \boldsymbol{r}(t) + \boldsymbol{v}(t)dt + \frac{\boldsymbol{f}(t)}{2m}dt^2 + o(dt^3) \\ \boldsymbol{v}(t+dt) = \boldsymbol{v}(t) + \frac{\boldsymbol{f}(t)}{m}dt + \frac{1}{2m}\frac{d\boldsymbol{f}(t)}{dt}dt^2 + o(dt^3) \end{cases} \tag{2.22}$$

Force derivatives can be expanded as $\frac{d\boldsymbol{f}(t)}{dt} = \frac{\boldsymbol{f}(t+dt)-\boldsymbol{f}(t)}{dt} + o(dt)$, allowing to rewrite Equation 2.22 without differential terms, as the so called "Velocity-Verlet algorithm":

$$\begin{cases} \boldsymbol{r}(t+dt) = \boldsymbol{r}(t) + \boldsymbol{v}(t)dt + \frac{\boldsymbol{f}(t)}{2m}dt^2 + o(dt^3) \\ \boldsymbol{v}(t+dt) = \boldsymbol{v}(t) + \frac{1}{2m}\left[\boldsymbol{f}(t) + \boldsymbol{f}(t+dt)\right]dt + o(dt^3) \end{cases} \tag{2.23}$$

Using the Velocity-Verlet algorithm, during each time step (t) positions and velocities at the following time step ($t + dt$) are computed together, in order to model the time evolution of the system.

It is important to choose an optimal timestep for the simulation, which should not be too short (the motion of particles would be too small for a meaningful description and the computational cost would be higher), neither too long (would cause integration errors resulting in total energy divergences). This parameter strongly depends on the nature of the system, therefore it must be carefully evaluated for each particular system performing preliminary test simulations.

Forces acting on the *i-th* atom are computed as the gradient of the potential energy surface in its surroundings:

$$f_i = \frac{dU(\boldsymbol{r_1}, ..., \boldsymbol{r_i}, ..., \boldsymbol{r_N})}{d\boldsymbol{r_i}} \tag{2.24}$$

There are several approximations available to model inter-atomic forces in a system during MD simulations, which are generally divided in two classes: classical force fields and *ab initio* methods. In the following we focus in particular on classical reactive force fields and on the Car-Parrinello implementation of *ab initio* MD, as we used these two approaches for all MD simulations.

2.3.1 Classical MD

Many contributions need to be taken into account to describe atomic bonds by means of classical models. In this work we used the ReaxFF [81] potential, since it has been proven valid to model graphene and graphene oxide reactions [82], [83], [84], [85]. ReaxFF is able to describe reactive interactions dealing on the bond order formalism. Bond order is calculated using an empirical formula which is a function of the interatomic distance (and other empirical parameters) and yields differentiable potential energy surfaces. Those terms in the potential which depend on bond order are directly calculated, then a charge equilibration scheme is applied to determine atomic charges, and subsequently to compute Coulombic interactions.

2.3.2 Car-Parrinello MD

To include quantum electronic effects in MD simulations, one straightforward way is to consider each step in the dynamic as a set of fixed atomic positions and reduce the electronic problem to a series of time-independent Schrödinger equations that can be approximated by DFT. This approach, called Born-Oppenheimer MD, requires the complete solution of the Kohn-Sham problem at each step and provides the exact energy of the system on the adiabatic potential surface, as described by DFT. For large systems and long trajectories, the computational time of Born-Oppenheimer MD may become prohibitive, for this reason in 1985 Car and Parrinello [86] suggested a way to reduce

the computational cost of *ab inito* MD simulations, avoiding to solve the KS equation after each step. The basic idea behind the Car-Parrinello approach is to deal on the adiabatic time-scales separation between fast electrons and slow nuclei to map a two-components quantum / classical system into a completely classical model with separate energy and time-scales. It exploits the fact that the forces acting on nuclei in classical dynamics can be obtained from derivatives of a suitable Lagrangian, to interpret electronic orbitals as classical fields with an associated Lagrangian $\mathscr{L}_{CP}$ whose derivatives yield the forces acting on these orbitals. It follows that the two-components classical system can be described with two Newtonian Car-Parrinello equations of motion: one describing slow ions, one describing fast electronic orbitals. As the equation of motion relative to the ionic part has an obvious description of the mass (the actual mass of the nuclei), the electronic part is associated with a fictitious mass μ_{el} that leads to the definition of a fictitious temperature associated to electrons. The main assumption of Car-Parrinello MD is that the electronic and ionic subsystems remain well decoupled during the adiabatic time evolution, so that ground-state electronic wavefunctions optimized for the initial configuration of the nuclei will remain close to the ground state during time evolution. Provided that optimal simulation parameters are chosen for the given system, adiabaticity should be preserved during the classical co-evolution of the ionic and electronic systems. Simulation parameters should be carefully chosen performing preliminary tests and by comparison with Born-Oppenheimer MD results as reference.

Car-Parrinello MD is extremely popular nowadays and has abundantly demonstrated its validity during the years. For more comprehensive information many reviews have been published about this fundamental computational method [87].

2.3.3 Temperature and pressure control

Molecular Dynamics can be performed on a system with a constant number of particles (N), according to different thermodynamical ensembles: micro-canonical which keeps the system at constant energy and volume (NVE), canonical which instead keeps the system at constant temperature and volume (NVT), isothermal-isobaric which keeps pressure and temperature fixed (NPT). Plain MD, without any applied thermostat, samples the micro-canonical ensemble, so the system is kept at constant energy (NVE), not at constant temperature. The temperature of a system under simulation can be derived from the equipartition rule which relates the mean kinetic energy of the system to the temperature:

$$< \frac{1}{2} m v^2 >= \frac{3}{2} k_B T \tag{2.25}$$

From Equation 2.25, which holds for 3-dimensional systems, the case for a system of N particles is obtained:

$$\frac{1}{2}\sum_{i=1}^{N} m_i v_i^2(t) = \frac{3}{2} N k_B T(t) \rightarrow T(t) = \frac{1}{3N k_B}\sum_{i=1}^{N} m_i v_i^2(t) \tag{2.26}$$

This puts a restriction on the choice of the initial conditions (particularly particles velocities), since they need to be consistent with the temperature at which the simulation is carried out. Attention must also be paid that the total momentum of the system remains zero, hence the sum of the velocities of all particles must be zero. A computational thermostat can be added to control the temperature of the system during simulations. The easiest way to implement a thermostat is to use a velocity scaling algorithm which adjusts particles velocities as:

$$v' = \lambda v$$

$$\lambda = \sqrt{\frac{T_{fixed}}{T(t)}}$$

Velocity scaling algorithms deeply affect the systems dynamics, introducing discontinuities due to velocity randomization. To mitigate this problem, the Nosé-Hoover thermostat [88] was introduced, where a variable, function of particles potential and kinetic energies, scales atomic velocities and the thermostat timestep (how often the thermostat acts to regulate the temperature) to simulate the application of a thermal bath. An equivalent approach to control the pressure of the system is the Nosé-Hoover barostat, which allows the volume of the system to scale, in order to keep pressure fixed.

2.4 Cluster Expansion

CE was proposed as a method to compute alloy energies by Gerbrand Ceder in 1993 [89]. It provides a representation of configuration-dependent alloys energies, based on a lattice model which describes configurational disorder. CE is a generalization of the Ising Hamiltonian and describes the occupation of lattice sites with binary variables σ that, in the formalism introduced by Ceder to describe binary alloys, indicate the presence of either a A or B atom on the $i-th$ lattice site. The method was successfully applied in studying the thermodynamics of alloy materials [90], as well as to model surface chemisorption [91] [92], for this reason we applied CE to study the clusterization of oxygen-containing species in low-coverage rGO.

With CE, the energy of a particular configuration of rGO is computed as the sum of energetic contributions of specific oxygen-containing clusters in that configuration. Each figure is represented as a set of sites on a lattice grid that can vary in number of combined states (singlets, pairs, triplets, quadruplets and so on) and maximum distance between lattice sites. In this work we applied a special case of CE, where each lattice site

is associated with an occupancy variable σ whose value can either be 0 (unoccupied) or 1 (occupied). We represented the lattice-gas Hamiltonian as [93]:

$$H(\sigma) = H_0 + \sum_{i=1}^{S_L} h_i \sigma_i + \sum_{i=1}^{S_L} \sum_{j=i+1}^{S_L} J_{ij} \sigma_i \sigma_j + \sum_{i=1}^{S_L} \sum_{j>i}^{S_L} \sum_{k>j}^{S_L} J_{ijk} \sigma_i \sigma_j \sigma_k \tag{2.27}$$

where H_0 is the energy of the pristine graphene layer, h_i is the energy contribution from a singlet (isolated oxygen-containing species), S_L is the number of sites in the lattice, while J_{ij} and J_{ijk} are the effective cluster interaction (ECI) coefficients of pairs and triplets modeling the contribution of each figure to the total energy. The expansions were truncated to triplets as it was shown in literature that considering only small figures (up to small triplets) generally ensures good accuracy while converging rapidly [94]. Proper figures and ECIs are determined by fitting them with a training set of relevant configurations whose energies were computed by mean of DFT. Finally, to evaluate the predictive power of a fitted CE, cross-validation (CV) scores are typically computed as [94]:

$$CV = \frac{1}{n} \sum_{i=1}^{n} (E_i - \widehat{E_{(i)}})^2 \tag{2.28}$$

where E_i is the energy of the i-th configuration computed by DFT, while $\widehat{E_{(i)}}$ is the predicted energy from a fit on the other (n-1) configurations. The CV score is not a monotonic function, in fact it typically decreases in the early stages of fitting (increasing predictive power) until it reaches a minimum and then start increasing (a sign of overfitting and therefore reduced predictive power). For this reason the CV score is an effective criterion to assess the predictive capabilities of CE, select the figures and the optimal level of fitting [94].

Our main goal using CE is to rapidly predict the energies of all oxygen-containing group clusters in rGO and then use this information to compute transition rates in Kinetic Monte Carlo (KMC) simulations to describe the evolution of oxygen-containing species in rGO during long simulation times, as we will see in Chapter 4.

2.5 Kinetic Monte Carlo

The KMC approach simulates the time evolution of processes (diffusion, desorption and clusterization of epoxides in our case, see Chapter 4) as a sequence of events whose occurrence is randomly selected on the basis of transition rates that depend on the local characteristics of the material. Transition rates for each possible events and for each oxygen-containing species are given as inputs to the algorithm and are computed based on the local environment of each species [95]. In our investigation of epoxide diffusion in rGO all events are thermally activated, so we computed energy potential barriers at each step of KMC evolution based on Nudged Elastic Band (NEB) calculations

of zero-coverage limit barriers (when only one epoxide is present on the surface) and CE-predicted total energies in the initial and final states of the transition (considering the energetic contributions from epoxide clusters). In particular, while NEB calculations which are computationally intensive were only performed once for isolated oxygens, CE allowed us to quickly estimate energies of rGO configurations, to include the stabilizing influence of clusters when computing potential energy barriers, at each step of KMC simulations. Finally, from energy barriers we could determine transition rates for every events, at each step and for each oxygen-containing species [93].

In Chapter 4 we will demonstrate how using KMC allows to simulate the accurate evolution of oxygen-containing species in rGO, for very long simulation time scales that are inaccessible even with computationally light MD simulations given the low probability of the events involved.

Chapter 3

Structure and electronic properties of monolayer rGO

3.1 Introduction

In this chapter we discuss the modeling, by means of classical MD and all electrons DFT simulations, of the atomic structure of reduced GO based on the work by Lerf and collaborators (introduced in Chapter 1.3). Using this model we extensively investigated the structural and electronic properties of this complex material, covering a range of oxidation levels (10-20% coverage) that fits important technological fields, such as membranes, sensors and optoelectronics. We will cover in detail how rGO is modeled to compute realistic representations of its atomic and electronic structures and how this allowed us to draw important conclusions on the composition of this material. In particular, we will discuss the formation of 1,2-ethers from epoxides and propose their addition as a distinct species in the Lerf-Klinowski model [23], based on rigorous evidences showing how these two oxygen-containing groups (epoxide and 1,2-ethers) have very different effects on GO. Moreover, we highlight the effects of these groups on the electronic structure of reduced GO around the Fermi level and possibly their contribution to C-1s XPS spectra. Part of the results that we discuss in this chapter were published, as a letter, in the *Journal of Physical Chemistry Letters* [96].

In this work we first created initial structures of rGO by randomly distributing epoxide and hydroxyl groups on both faces of a graphene supercell, according to different coverages Θ (defined as the atomic percentage with respect to carbon atoms) and —OH/—O— ratios. These initial model structures were subject to classical MD room temperature annealing, to promote the adsorption of oxygen-containing groups and create a stable rGO monolayer. In this sense, sufficiently long MD runs activate the accessible vibrational modes at a given temperature, yielding structures which are thermodynamically stable. After classical MD thermal treatment, the atomic structure of the obtained rGO monolayers was relaxed by means of DFT, to minimize their conformational energy to the nearest minimum as approximated with hybrid-DFT. Finally we

analyzed the structural characteristics of our *in silico* rGO samples, computed their valence electron density of states (DOS) and simulated their XPS spectra, based on B3LYP-DFT eigenvalues of carbon core electrons.

3.2 Atomic model

Reduced GO composition varies, depending on the fabrication method and reduction treatments, within a wide range of stoichiometries. To represent this variability we created samples with different oxidation degrees and ratios between hydroxyl and epoxide groups. We placed these groups at random adsorption sites over an orthorombic 4x7 pristine graphene supercell, in order to model the amorphous nature of GO. In this sense, we created 6 independent samples for each oxidation level and —OH/—O— ratio to represent the high variability of reduced GO oxidation and to average our analysis on a statistically meaningful ensemble. Graphene rectangular cell was obtained from geometrical transformation of a primitive hexagonal cell, with lattice parameter $a_{hex} = 2.458$ Åresulting from atomic relaxation by means of DFT. After transforming the hexagonal cell into a rectangular one, we replicated it 4 times along x-direction and 7 times along y-direction, resulting in a final supercell with lattice parameters $a_{1,sup} = 17.035$ Å, $a_{2,sup} = 17.212$ Å and containing 112 carbon atoms. Finally, we prepared our *in silico* samples of reduced GO by distributing epoxide and hydroxyl species on both sides of graphene supercells to represent $\Theta = 10\% - 20\%$ atomic coverages and —OH/—O— = 0%, 25%, 50% and 100% (addressing respectively samples with only –O–, with 75% –O– and 25% –OH, 50% –O– and 50% –OH and ultimately only –OH). This oxidation range fits typical rGO compositions, usually reported in the experimental literature [97] [98]. One of these model structure is shown in Figure 3.1 as an example.

3.3 Simulation Strategy

3.3.1 Classical MD

To perform classical MD simulations we used the LAMMPS code [99] and the ReaxFF reactive force field to describe the atomic interactions [81]. Since ReaxFF allows to simulate the formation and breaking of atomic bonds, it is rather valuable to model the oxidation of graphene into GO, as reported in the literature [100]. We ran NPT dynamics using Nosé-Hoover thermostat and barostat, while integrating equations of motion with time-step $dt = 0.25$ fs. Pressure was kept constant at $P = 0$ Pa during the whole MD run (to allow the supercell to change its dimension and reduce induced stress), temperature instead was modified as follows:

- Initial heating ramp to $T = 300$ K, 0.5 ps long.

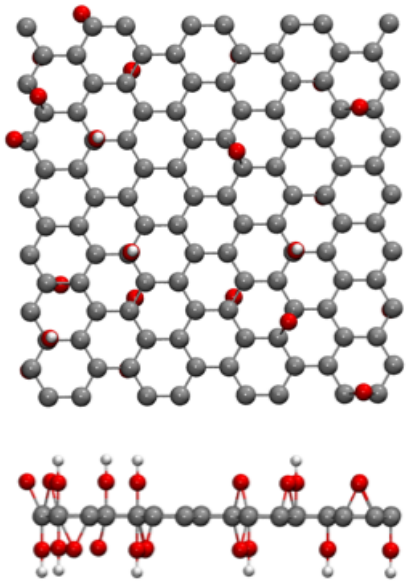

Figure 3.1: Top and side views of one of the initial model structures for rGO at a given oxidation ($\theta = 20\%, —OH/—O— = 50\%$) that we used in this investigation. MD and DFT relaxation will follow in order to obtain a realistic sample.

- Annealing at constant $T = 300$ K for 50 ps.
- Final cooling ramp from $T = 300$ K to $T = 10$ K, 0.5 ps long

The use of classical MD for preliminary structural optimization allowed us to reduce the computational cost that a DFT relaxation would have required, therefore to increase the number of simulated structures to improve the statistical relevance of our simulations. Final MD snapshots for each sample were then used as starting points for successive DFT relaxation steps, to obtain more accurate structures at a quantum level of description.

3.3.2 Density Functional Theory

We based our DFT simulations on hybrid exchange-correlation functionals that, as we discussed in the previous chapter, usually describe electronic properties (e.g. electronic band gap and excitation energies) more accurately than GGA functionals [68]. Moreover, we opted for a full-electrons description by means of localized atomic basis sets since this allows to investigate details of the core electrons which are fundamental to simulate XPS spectra. In particular, we used the CRYSTAL14 package [101] with B3LYP exchange-correlation functional. Following preliminary tests, we determined the DFT configuration that gave most accurate results with respect to the experimental

lattice parameters and atomic distances of graphene and diamond, representative of sp^2 and sp^3 hybridized carbons. Atomic orbitals were expanded as linear combinations of local atom-centered gaussian functions. Carbons were described with a double-zeta polarized 6-111G* basis set [102], while oxygens and hydrogens were described respectively with a 8-411G* and 3-11G* basis sets [103] [104]. For all DFT calculations we used a Monkhorst-Pack grid of 14 k-points along the x-y plane in the reciprocal space. To converge SCF cycles we allowed for a maximum energy difference of $2.7 \cdot 10^{-6}$eV while forces during relaxations were minimized down to $2.3 \cdot 10^{-2}$eV/Å.

3.4 Reduced GO structural analysis

The structures of our *in silico* rGO samples were analyzed in terms of C—C bond distance distribution (d_{CC}) and average out-of-plane carbon displacement ($\overline{\delta_z}$). These are representative respectively of in-plane deformations and of structural corrugation. As reference we simulated a pristine graphene structure which has an almost Dirac delta C—C distribution centered at $d_{CC} = 1.42$Å and a perfectly flat structure $\overline{\delta_z} = 0$Å in agreement with experiments [105] and other B3LYP results [102].

Our simulations showed that when only epoxide are present in the GO structure, the C—C distribution presents three distinct contributions, an example is reported in Figure 3.2 for samples with 20% oxygen coverage. The main peak (1.3Å – 1.5Å) originates from distorted sp^2 hybridized carbon bonds, while sp^3 C—C bonds bridged with epoxides are responsible for peaks between 1.4 Å and 1.8 Å. Interestingly, we discovered that the third contribution (2.1 Å – 2.5 Å) comes from broken C—C bonds originating from the transformation of some epoxides into 1,2-ethers. We will discuss the origin and properties of this latter species in the following section, at the moment we will limit our observations to relevant deformations induced in the planar structure. To this extent, we noticed that epoxides and ethers induce strong corrugation of the graphitic layer and this increases for higher concentration of these species. In our simulations, the average out-of-plane displacement (as defined in Figure 3.4) increased from $\overline{\delta_z} \approx 0.4$Å ($\sigma_z \approx 0.2$Å) for structures at 10% coverage to $\overline{\delta_z} \approx 0.7$Å ($\sigma_z \approx 0.2$Å) for structures at 20% coverage.

When only hydroxyls are present in the structure instead, the C—C distribution presents two clear contributions, of which we can see an example in Figure 3.3 for samples with 20% oxygen coverage. As in the previous case, with only epoxides and ethers, we have a main peak between 1.3 Å and 1.5 Å that originates from distorted graphene-like carbons, but this time the contribution from sp^3 C—C bonds appears as a very sharp peak between 1.5 Å and 1.6 Å. This suggests that the adsorption of –OH has a local strain effects on C–C bonds and cause less extended deformations in the graphitic structure, as also supported by smaller average out-of-plane displacements ($\overline{\delta_z} \approx 0.3$Å with $\sigma_z \approx 0.1$Åat 10% coverage and $\overline{\delta_z} \approx 0.3$Å with $\sigma_z \approx 0.1$Åat 20% coverage).

In summary, we demonstrated that a higher degree of oxidation determines stronger

deformations of the graphitic lattice, both in terms of average C—C distances and corrugation. While epoxide and ether species induce large in-plane strain and an overall strong corrugation, the effects of –OH adsorption are localized on the adsorption site and its first neighbors so that structures remain almost flat.

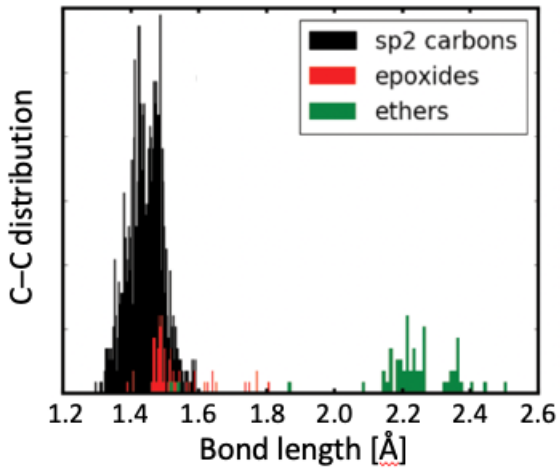

Figure 3.2: C—C bond length distribution of rGO samples at 20% oxygen coverage, with only epoxides in the structure. The contribution from graphene-like carbons is shown in black, from epoxide groups in red and from 1,2-ethers in green. Figure reproduced from [96] with permissions from ACS.

3.5 Charge distribution analysis and 1,2-ethers identification

To discriminate between epoxides and the 1,2-ethers that we introduced in the previous section, we had to explicitly identify the presence or absence of a bond between the two carbon atoms bound to an —O— species. We based this analysis on the Quantum Theory of Atoms in Molecules (QTAIM) introduced by Bader [106], which states that atoms and bonds can be identified as stationary points in the electronic density distribution. This 3D scalar field represents a probability distribution in the real space of a crystalline structure (or molecule) which describes the average distribution of the electronic charge in the external potential created by the nuclei. Bader's theory mathematically analyzes the topology of the electronic density distribution ($\rho_{el}(\boldsymbol{r})$) to identify critical points where density gradient vanishes ($\nabla\rho_{el}(\boldsymbol{r}) = \mathbf{0}$). These critical points (CP) can be further analyzed by computing the Laplacian ($\nabla^2\rho_{el}(\boldsymbol{r})$) from which we can identify whether a CP is a local maximum (atomic nucleus) or a point on a saddle that links two local maxima (bond).

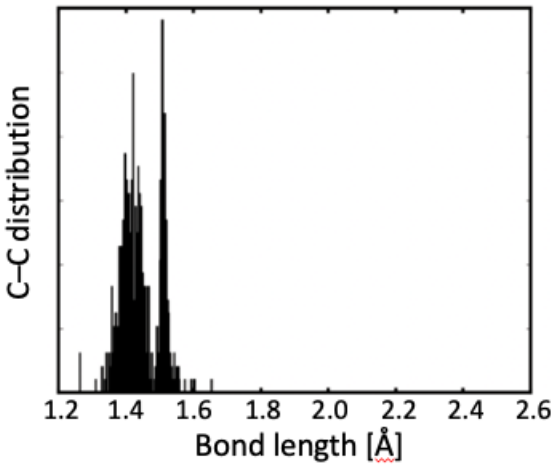

Figure 3.3: C—C bonds length distribution of rGO samples at 20% oxygen coverage, with only hydroxyls in the structure. The contribution from hydroxyl groups can be seen as a sharp peak between 1.5Å and 1.6Å. Figure reproduced from [96] with permissions from ACS.

We applied QTAIM to distinguish between 1,2-ethers and epoxides in rGO by checking if the electron density presents a "bond" type CP between carbon atoms bound to an –O– species. If this CP exists then the carbon atoms are 4-coordinated (sp^3 hybridized) and –O– is an epoxide group. If the two carbon atoms are not bonded together instead, they form a 1,2-ether species which preserves the sp^2 hybridization of graphene while introducing large strains in the structure due to increased interatomic distances.

Being able to accurately sort ethers from epoxides, we observed that when epoxide groups are clustered together in the initial model structure the formation of ethers is favored. In particular, according to our observations, ethers are preferentially found when several epoxides are clustered within the range of few aromatic rings.

Finally, to provide a comprehensive description of the effects of oxidation in rGO, we investigated the transfer of electronic charge between carbon and oxygen atoms. We computed this charge transfer by comparing Mulliken electronic populations of pristine graphene and of our rGO samples. Our findings show that there is always a transfer of electrons from carbons in the graphitic basal plane to the adsorbed oxygens, with epoxides and ethers drawing more charge than hydroxyl species. The total amount of transferred charge linearly depends on the degree of oxidation. As a final remark, we would like to clarify that, although there is accumulation of charge on the adsorbed oxygen-containing species, we do not expect any net polarity (also in terms of spin) along the vertical direction in our *in silico* samples, due to the random distribution of oxygen-containing species on both sides of rGO model structures.

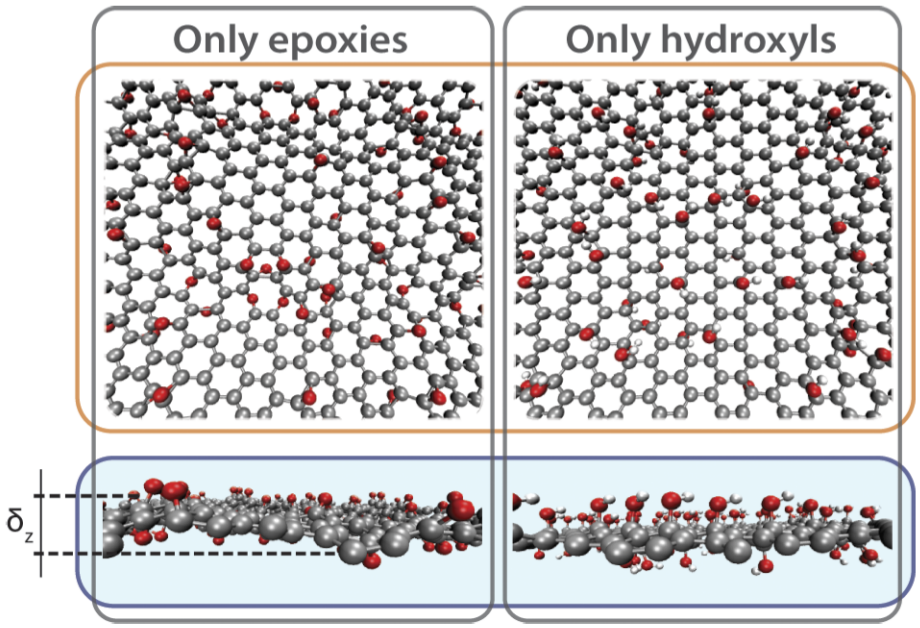

Figure 3.4: Example of two rGO structures at 20% coverage, containing only epoxide/ethers (left) and only hydroxyls (right), reported in [96]. The definition of $\overline{\delta_z}$ is reported in the light blue panel with the side view of these samples, from which it is possible to see the difference in the extent of corrugation induced by ethers/epoxide (left) and by hydroxyls (right). Figure reproduced from [96] with permissions from ACS.

3.6 Reduced GO electronic properties

To investigate the effects of oxygen-containing species on the electronic properties of rGO we computed the electronic density of states (DOS) of the valence and conduction bands in proximity to the Fermi level for all our samples. We discovered that structures containing only epoxides and ethers present an energy gap between valence and conduction bands whose width is proportional to the degree of oxidation. Computed at a B3LYP level of approximation, this ranges on average from about 0.6 eV at 10% coverage to about 0.8 eV at 20% coverage.

Hydroxyls, on the other side, induce sharp defect states at the Fermi level in the computed total DOS, making rGO samples apparently metallic. To deepen our knowledge of the effects of hydroxyl species in rGO we investigated model structures with just one and two adsorbed –OH, in order to appreciate specific modifications from isolated species and their combination. Upon the adsorption of a single –OH group, a band-gap of about 0.5eV is present in the total DOS. The formation of this band-gap and of the high-density peak appearing around the Fermi level, is due to broken symmetry around the adsorption site which cause p_z bonds of neighboring carbons to localize, as can be

seen in Figure 3.5 from the DOS projected on specific atoms and orbitals. Contributions from first neighbors of the adsorption site to the DOS are relevant close to the valence band edge, with carbon atoms further away from the –OH contributing less to this band, as confirmation of the localization effect. When we considered the presence of two adsorbed –OH instead, the overall effect on the total DOS was less clear and appeared to depend on the relative positions of the two species. In particular, depending on whether the two –OH species are adsorbed on sites belonging to the same graphene sub-lattice and how far from each other these sites are, the total DOS showed very different characteristics: either a well defined band-gap or high-density peaks at the Fermi level. To conclude, the disordered nature of rGO means that is ideally impossible for hydroxyl groups to bind only on one specific graphene sub-lattice, so that the overall effect of –OH adsorption on the DOS of our *in silico* samples was always to induce high density states at the Fermi level, even when in presence of epoxides and ethers.

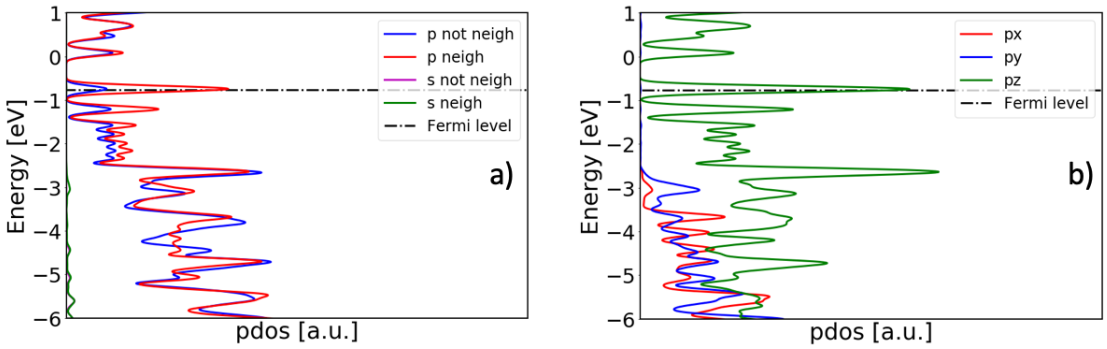

Figure 3.5: Projected DOS on p and s orbitals of the –OH adsorption site's first neighbors and farther carbons (a). Projected DOS on p_x, p_y and p_z electronic orbitals of carbon atoms that are first neighbors of one adsorbed –OH (b).

3.7 Simulation of C-1s XPS spectra

As we saw in previous sections, rGO is a disordered material whose structural and electronic properties are deeply influenced by the oxidation degree and by oxygen-containing species concentration and relative positions. XPS is usually employed to experimentally measure the concentration of oxygen-containing species and infer the oxidation degree of GO flakes, given the semi-quantitative character of the technique, as we discussed in Chapter 1.4. XPS peaks are typically deconvoluted into Gaussians or Lorentzian functions centered at different binding energy values which are then used to identify the chemical species contributing to the total spectra. To simulate realistic XPS spectra we applied the same concept, by associating Lorentzian functions (HWHM

= 0.25 eV) to core electron eigenvalues of each carbon atoms in our structures, as computed by hybrid-DFT. We decided to report XPS spectra as a function of the chemical shift (energy difference) between different oxygen-containing group contributions and the peak resulting from sp^2 hybridized carbons, that we use as energy reference. This is motivated by the fact that absolute energies have no physical meaning in DFT, while energy differences have. In Figure 3.6 are reported simulated C-1s XPS spectra for rGO structures at 20% coverage, containing only epoxides and ethers (a) and only hydroxyls (b). The reference peak, arising from sp^2 graphene-like carbons, is reported in black and is always centered at 0 eV, while contributions from carbons bonded to oxygen-containing species are reported in red (epoxides), green (1,2-ethers) and purple (hydroxyls), at specific chemical shifts that remain constant when changing the degree of oxidation. Specifically, we observed that the 1,2-ether peak is shifted toward higher energies by $\sim$ 1.2 eV, the epoxide peak is shifted by $\sim$ 1.6 eV and the hydroxyl peak by $\sim$ 1.7 eV with respect to the graphitic peak. These values are consistent with experimental results reported by Hossain and collaborators [107] concerning the epoxide peak, and with simulations by Barinov et al based on small structures with few functional groups [108]. These simulated spectra highlight the possibility to identify different chemical species in rGO using XPS with the assistance of accurate *ab initio* modeling to clarify the experimental interpretation of XPS peaks. Moreover, by identifying different contributions to XPS peaks from epoxides and 1,2-ethers we provided further evidences supporting the distinction between these two species.

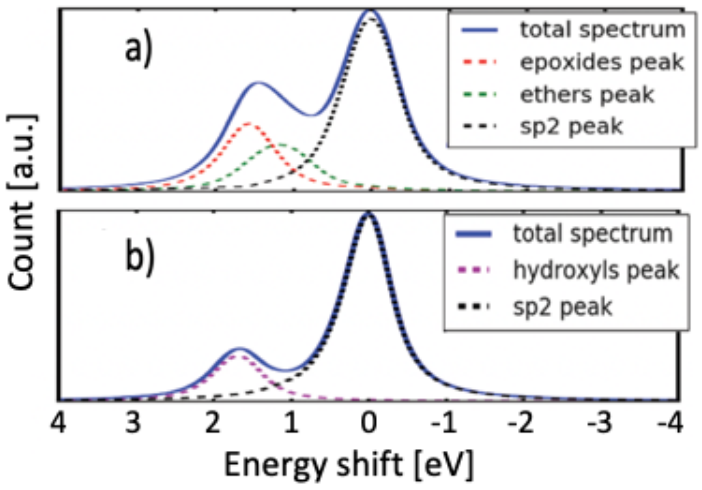

Figure 3.6: Simulated XPS spectra of rGO at coverage $\Theta = 20\%$: only epoxide and ether groups (a), only hydroxyl groups (b).

3.8 Conclusions and perspectives

State-of-the-art atomistic simulations were used to extensively investigate structural and electronic properties of rGO samples with different compositions. We created accurate computational models for rGO at different compositions and degrees of oxidation, based on the Lerf-Klinowski model, and used MD and DFT to optimize and relax these structures. After preparing these models, we used accurate DFT simulations to investigate the structural and electronic properties of monolayer rGO. Our investigation revealed a strong distinction between epoxide species and 1,2-ethers, a species which is not considered neither in the Lerf-Klinowski nor Szabó-Dékány models, both originating from bridged oxygen (—O—). In this sense, we highlighted the presence of 1,2-ethers by mean of rigorous topological analysis of the electronic density [106] and observed that these are preferentially formed when epoxides are clusterized. As consequence, we propose the addition of 1,2-ethers to the Lerf-Klinowski model. For these three oxygen-containing species (epoxides, 1,2-ethers and hydroxyls) we reported evidences of different modifications that they induce on the structural and electronic properties of rGO, as well as their contribution to XPS C-1s spectra. In particular, we demonstrated that epoxides and ethers, not only induce the strongest deformations in the plane of rGO, but also introduce an energy band gap between valence and conduction bands which is proportional to their concentrations. On the other side, we showed that hydroxyls act locally in the 2D plane, changing the planar sp^2 hybridization of neighboring carbons to tetrahedral sp^3 and introducing intense defect states around the Fermi level in the surroundings of adsorption sites.

The potential contributions of this work to the research field of GO are many. Considerations drawn from the analysis of the DOS of our *in silico* samples may aide in tailoring the electronic properties of rGO flakes for applications such as electronic and optical devices. Moreover, detailed knowledge of 1,2-ethers have an important role in devising treatments to produce defect-free rGO as well as controlled pores formation, opening the path to important applications such as for example graphene substitutes and atomic-sized membranes for molecular filtration. For this reason, in the next Chapter we will present a two-step process to produce uniform pores of controllable size in monolayer rGO, based on a thorough investigation of chemo-physical transformations that occur in this material and lead to oxygen-containing groups clusterization. We will show, by means of accurate atomistic simulations, that by first promoting the clusterization of epoxides and ethers and then reducing rGO flakes at high temperatures, it is possible to produce pores with optimal size for water desalination and therefore fabricate effective single layer graphitic membranes for this purpose. Finally, we expect that the C-1s XPS chemical shifts, that we computed and attributed to the three main oxygen-containing species in rGO basal plane, will provide useful indications to interpret experimental XPS spectra of rGO flakes, which is of paramount importance for all those applications that need a careful control of the material composition.

Chapter 4

Controlled pores formation in monolayer Graphene Oxide

4.1 Introduction

As we discussed in Chapter 1.5.1, the use of graphene for the production of membranes is considered by many in the scientific literature as part of the solution to improve the efficiency and applicability of filtration technologies. In particular, fields of growing and vital importance such as water filtration (e.g. desalination) or renewable energy storage and production (e.g. membranes for electrolyte separation) are expected to abundantly benefit from the application of this material [46] [109]. As we have seen in that chapter, in the case of water desalination by means of reverse osmosis filtration, the use of nanoporous graphene membranes can greatly improve process performances, ideally offering almost complete salt rejection (if pores are of the optimal size) and water permeability order of magnitude higher than commercial membranes [30] [110]. Unfortunately, the fabrication of graphene membranes with controlled and uniform pores is still facing many difficulties, typically showing lack of pore size accuracy and of fabrication scalability [111] [112]. In this chapter we will discuss the application of monolayer rGO as a substitute of graphene for the fabrication of ultra-thin membranes for water desalination and we will also introduce a possible experimental treatment to accurately engineer the structure of rGO in this sense. The use of rGO for this purpose was suggested by Lin and collaborators [31] based on MD simulations. They showed how the annealing at high temperature of rGO produces holes in the material that can be exploited for water filtration, although pores obtained in this way are hardly controllable in size.

In the previous chapter, after creating accurate *in silico* models of monolayer rGO, we investigated its structural and electronic properties and observed a tendency of epoxide and ether groups to yield more stable structures (in terms of total energy) when they are close to each other. These conclusions are in agreement with that of Kumar and collaborators [113] which observed experimentally the tendency of GO to form

separate phases (highly oxidized areas and pristine graphene areas) when annealed at a temperature of 80 °C. As discussed by the same authors in a further publication [114], the formation of highly oxidized areas in rGO seems to enhance the removal of carbon atoms when exposed to high temperatures, therefore we decided to investigate the possibility to exploit this behavior to fabricate single-layer porous rGO membranes.

In this chapter we will discuss results from our thorough study of the mechanisms that lead oxygen-containing groups to diffuse and clusterize in rGO, we will analyze how to control this phenomenon and exploit it to produce pores of accurate and precise size. We first studied, by means of state-of-the-art DFT, CE and KMC simulations, the driving forces behind clustering of oxygen-containing species and simulated their evolution on the time-scale of days, focusing on epoxides for their predicted ability to produce pores in the graphitic layer when desorbed [39]. Then we investigated the role of high-temperature treatments concerning the removal of oxygen and carbon from rGO, confirming the evolution of CO and CO_2 molecules following the breaking of C—C bonds and the formation of pores in correspondence of oxidized areas. With these meticulous studies we highlighted the appropriate physical conditions to obtain circular pores of controllable size in monolayer rGO and provided quantitative relationships between initial rGO oxidation levels, annealing time, temperatures and final pore shape and dimension. These contributions are of fundamental importance for the scalable and reliable production of porous single layer rGO membranes for water filtration and were published in the *Journal of Physical Chemistry Letters* [93].

4.2 Simulation Strategy

We used KMC to simulate the evolution of rGO structures during thermal annealing at low temperatures, for simulation times up to 5.6 days, and investigated the diffusion of epoxides in rGO structures with different coverages. The evolution of rGO in time was modeled as a series of thermally activated events, whose transition rates were calculated by mean of CE. Using CE we could quickly predict configurational energies of rGO structures containing epoxides and so compute diffusion energy barriers of all possible events, for each epoxide at every step of the KMC simulation. We used DFT to model all possible configurations of epoxide pairs and triplets, compute energies of relative rGO samples and used such training set to fit CE parameters and eventually predict total energies of given rGO structures.

After studying the clusterization of epoxide groups we investigated the use of high-temperature treatments to produce pores in correspondence of these oxidized areas. To model the harsh annealing of clusterized rGO structures, we used classical MD with the ReaxFF interatomic potential after validating preliminary results with respect to *ab initio* MD simulations.

4.2.1 Kinetic Monte Carlo

KMC simulations were used to model the long (up to more than 5 days) mild annealing of large low-coverage rGO structures and investigate the diffusion and clusterization of epoxide species. We modeled the evolution of epoxides as a sequence of events, selected randomly on the basis of transition rates. These events are thermally activated, so we computed their KMC transition rates as:

$$k = A \cdot e^{-\frac{E_{bar}(\sigma)}{k_B T}} \tag{4.1}$$

where $E_{bar}(\sigma)$ is the energy barrier for event σ considering interaction between epoxides. It is calculated computing the energy barriers in the zero-coverage limit for each event (diffusion and desorption) from NEB simulations and by shifting these barriers according to the energy differences between initial and final states. Energy shifts take into account epoxide-epoxide interactions since they are obtained from predicted CE configurational energies. This approximation of assuming a constant value for energy barriers as in the zero-coverage limit, is at the foundation of the Zacros software [115] to compute the activation energy of dynamical events and it has been used to model complex reactions such as catalysis [116] [91]. Pre-exponential factors (A) were calculated from phonon frequencies as indicated in [117]. We only considered diffusion and desorption events during KMC, since for adsorption we calculated a very high potential barrier and low pre-exponential.

Reduced GO monolayers were modeled with 120 Å × 120 Å supercells over which we initially distributed epoxides in random positions, representing 4 different possible coverages: 5%, 10%, 15% and 30%. We simulated mild annealing of rGO supercells at 300K and 350K for all different coverages using the Zacros software [115].

4.2.2 Cluster expansion

As we saw in Chapter 2.4, CE models the energy of a given atomic configuration as the summation of energetic contributions from figures constituting that particular configuration, weighted by the effective cluster interaction (ECI) coefficient J_i representing how energetically favorable is each possible figure. We performed CE using the Alloy Theoretic Automated Toolkit (ATAT) [94], with a fitting set of rGO supercells optimized by means of DFT that allowed to achieve an expansion of 14 figures with a validation score of 0.002eV. Structures in the fitting set contained a few epoxides, with all possible pairs and triplets accounted for within a diameter of 6Å, whose energy was computed by means of DFT. We excluded nearest-neighbor epoxides from the training set since they led to instabilities, and considered the oxidation only on one side of rGO after determining with preliminary tests that for CE the side on which epoxides are positioned is irrelevant. In Figure 4.1 are reported (a) the DFT formation energies of possible epoxide pairs all on one side of rGO (we tested also the case where epoxides

are distributed on both sides and obtained minimal differences) and (b) all figures used to compute configurational energies with CE, as published in [93].

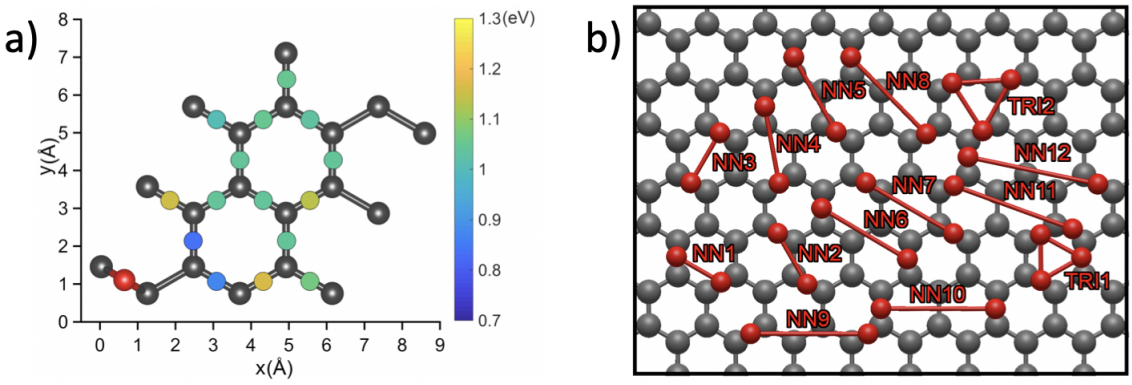

Figure 4.1: Formation energies of all possible epoxide pairs on one side of rGO calculated by mean of DFT (a) and 14 figures (pairs and triplets) used for CE (b). Figure reproduced from [93] with permissions from ACS.

4.2.3 Density Functional Theory

To fit Cluster Expansions we computed configurational energies by mean of plane waves based DFT as implemented in Quantum Espresso [79], using the PBE functional for exchange and correlation [72] and ultrasoft pseudopotentials [118]. Electronic wavefunctions were expanded up to an energy cutoff $E_{cut} = 36$ Ry and a $(14 \times 14 \times 1)$ Monkhorst-Pack grid to sample the Brillouin Zone of graphene primitive cell, then scaled accordingly to the dimensions of the supercell used. Graphene and rGO monolayers were represented using 6×6 supercells with periodic boundary conditions and a periodicity of 10 Å along the vertical axis (distance between vertical replicas). To relax supercell dimensions and atomic positions we minimized forces down to 26 meV/Å.

As in this chapter we are not investigating directly the electronic properties of rGO but rather its structural properties and how these evolve under certain conditions, we decided to use a GGA functional (PBE) to model electronic exchange and correlation. As we discussed in Chapter 2, GGA functionals typically describe surfaces and adsorbed species with sufficient accuracy, at a reduced computational cost with respect to hybrid functionals which instead are typically used to model electronic excitations. We tested the validity of using the PBE functional in this work by comparing the adsorption energy of one oxygen atom on a coronene molecule computed with different DFT functionals with respect to that computed by chemically accurate DLPNO-CCSD(T) simulations [119] using the ORCA software [120]. We considered for this comparison LDA (PW91 [71]), GGA (PBE), meta-GGA (SCAN [121]) and hybrid (PBE0 [122] and B3LYP)

DFT functionals. We performed DLPNO-CCSD(T) using an automated procedure to extrapolate the correlation energy to the basis set limit as implemented in ORCA, considering polarized triple-zeta (cc-pVTZ) and quadruple-zeta (cc-pVQZ) basis sets. From this comparison we observed that in the case of oxygen adsorption on a coronene molecule, the meta-GGA SCAN functional yields the closest value to DLPNO-CCSD(T) adsorption energy, nonetheless PBE, PBE0 and B3LYP yielded similar consistent results. Based on these evidences we decided to use the PBE functional to model the structural properties of rGO, as it provided results comparable with hybrid and meta-GGA functionals, at a fraction of their computational cost.

4.2.4 Molecular Dynamics

To understand the effects of high-temperature reducing treatments on clusterized epoxides, we performed classical reactive MD simulations, using LAMMPS [99] with the ReaxFF interatomic potential [81]. We used 43 Å × 45 Å × 90 Å periodic graphene supercells with clustered oxidized areas at their center, considering local atomic coverages (only the clusters area) of 12.5% and 25.3% and different –O– / –OH ratios (0.33 and 3.00). We simulated the heating of rGO samples with a 4 ps temperature ramp from 10K to target temperature, followed by 500 ps NVT dynamics at fixed temperature and finally a 1 ps cooling ramp to 300 K from which temperature is kept fixed for another 40 ps. We ran simulations at three target temperature (1000 K, 1500 K and 2500 K) that represent three different process intensities and should not be taken quantitatively. Indeed, in the field of MD it is common practice to increase simulations temperature to increase reaction speed of otherwise very slow processes and to reduce simulation times [31]. All simulations were performed with an integration timestep of 0.1 fs and Nosé-Hoover thermostat with a damping factor of 100 timesteps.

Before using ReaxFF to model the breaking and formation of bonds in rGO at high temperatures, we performed a preliminary validation, comparing results from classical simulations and accurate Car-Parrinello MD runs. We modeled one low-coverage ($\Theta = 10\%$) rGO structure, with only epoxides in packed configuration, using a 17 Å× 17Å× 12Å periodic supercell. Although dimensions of this test sample are smaller than the actual structures used for classical MD due to the much higher computational cost of *ab initio* MD, they are typical of DFT investigations of rGO and were shown to provide reliable results with negligible self-interaction between replicas [39] [38] [96]. We only compared results at 2500 K to promote faster desorption of carbons and oxygens and reduce simulation time. We performed accurate CP MD simulations using the Quantum Espresso suite [79], with PBE exchange and correlation functional [72] and ultrasoft pseudopotentials [118]. Electronic wavefunctions were expanded up to an energy cutoff $E_{cut} = 36$ Ry and the Brillouin Zone was only sampled at Γ. After initial system setup and electronic energy minimization, CP MD was performed using an electron fictitious mass $\mu = 200$ a.u. and a timestep $dt = 6$ a.u. for Verlet integration of the equations of

motion. As with classical dynamics we increased the temperature of our system gradually, from ~0 K to 2500 K in ~4 ps. When the system reached thermal equilibrium we performed 16ps of microcanonical (NVE) MD during which we collected data for trajectory analysis. Although temperature control was not applied during these 16 ps, the system temperature remained stable at ~2500 K as set initially. Comparing classical and *ab initio* MD trajectories, both starting from the same epoxide cluster configuration, we observed similar evolutions of the oxidized areas. During the initial MD steps, the graphitic lattice in correspondence with the epoxide cluster becomes very distorted and defected. Eventually, the formation of pentagonal and heptagonal rings and their vertical displacement out of the graphitic plane lead to the formation of a small pore, terminated with mainly carbonyl species. During both classical and *ab initio* MD simulations we observed the desorption of CO molecules from the edges of this pore, leading to the formation of further defects and growing of the pore area.

4.3 Epoxide clusterization analysis

In this work we used KMC to simulate the evolution of epoxides in rGO during low temperature annealing, to provide an accurate atomistic analysis of how these groups diffuse and clusterize during days of mild thermal treatment. KMC allowed us to expand the time scale of this study from nanoseconds (achievable with classical MD) to days and therefore to provide a much more realistic description of these phenomena with respect to what we could have achieved using MD. Modeling large rGO structures and performing long simulations we could provide realistic and quantitative relationships between annealing time, temperature and final clusters dimensions, that can be transferred to experimental procedures.

In this work we used CE to accurately predict total energies of monolayer rGO structures at each event during KMC simulations and compute transition rates relative to each possible event (diffusion or desorption). We observed, from preliminary DFT and NEB simulations that the adsorption of an oxygen atoms is a highly unfavorable event due to high energy barriers and low pre-exponential factors. First, we fitted CE parameters using a training set of DFT structures representing all possible pairs and triplets of epoxides within a radius of 6 Å in rGO, then we used CE to quickly predict configurational energies of rGO samples and compute energy barriers and transition rates for KMC simulations. After training CE to predict the energy of rGO structures containing epoxide species, we created realistic rGO supercells to simulate effects of mild annealing on the diffusion of these groups. Epoxides were distributed randomly on the surface of 120 Å × 120 Å supercells, according to different possible coverages (Θ = 5%, 10%, 15%, 30%) and all structures were run both at 300 K and 350 K.

At the early stages of the annealing at 300 K (Figure 4.2(a)), isolated epoxides are very mobile, randomly diffusing on the surface of rGO. As soon as epoxides come in contact they tend to aggregate into metastable clusters that are subject to structural

rearrangements, growth, diffusion and eventually coalescence with other clusters. Our KMC simulations showed a rapid formation of small clusters, in less than 4 minutes (Figure 4.2(b)), followed by a slow progression of aggregations and rearrangements that lead to the formation of large stable clusters. In Figure 4.2(c) we report from [93], as an example, a screenshot of the evolution of epoxide clusters in a $\Theta = 5\%$ rGO monolayer after 5.6 days at 300 K. In this example, from t = 4 minutes to t = 5.6 days, the mean area of oxidized clusters grew from 13 Å to 31 Å, highlighting the slowness of such processes. The importance of time for epoxide clusterization is clearly visible from the distribution of cluster size density as a function of simulation time, as reported in Figure 4.3.

The growth of epoxide clusters has typically a high potential barrier, since clusters that arrange in favorable low-energy configurations become very immobile and stable (as demonstrated by lower CE configurational energies). Therefore, in order for epoxide to diffuse and form larger and more stable clusters, large potential barriers have to be overcome to break the metastability of the initial clusters and detach. To have a quantitative idea of the potential barriers to overcome to form or break an epoxide cluster, we used NEB to compute diffusion barriers for an epoxide approaching and leaving a pair of epoxides, as reported in Figure 4.4. As we can see, an epoxide approaching an epoxide pair is faced with high potential barriers which reduce the closer the epoxide gets to the pairs, due to stabilizing interactions between epoxides forming a triplet. On the other side, an epoxide leaving a triplet is faced with much higher potential barriers, meaning that the detaching of an epoxide from a cluster is less probable during the annealing. From CE energy predictions we noticed that the more stable clusters during KMC annealing were the ones with lower configurational energies. We observed that these stable clusters tend to maximize the number of highly favorable epoxide pairs. From the analysis of pair formation energies computed with DFT, as reported in Figure 4.1(a), it is possible to notice that two configurations are the most stable as their configurational energies are particularly low. The computed ECIs for these two optimal epoxide pair figures are reported in Figure 4.5 and are the lowest values among all 14 different figures used for CE. Based on these evidences, we advance the hypothesis that the driving force behind epoxides clusterization at room temperature in reduced rGO, is the maximization of energetically favorable pairs in dense oxidized clusters. Finally, during KMC simulations we did not observe oxygens desorption, confirming our preliminary conclusion that it is a low-probability process at room temperatures.

Increasing the annealing temperature from 300 K to 350 K we noticed a remarkable acceleration of the clusterization process, with no apparent changes to the mechanism of cluster formation. As a reference, to obtain oxidized clusters with a mean surface area of 31 Å took 3.6 days at 300 K and only 14 minutes at 350 K. We also investigated the effects of higher initial coverages on the shapes and dimensions of the final clusters, and found that for higher coverages the final clusters are less circular and tend to favor linear configurations with epoxides distributed as zig-zag chains. For the highest coverage ($\Theta = 30\%$) it was impossible to identify singular clusters, and this suggests that GO,

and highly oxidized rGO, are likely to yield monolayers with two separate phases after mild annealing: large highly oxidized and pristine graphene areas. In Figure 4.6 are reported, from [93], examples of rGO monolayers at $\Theta = 5\%$ (a), $\Theta = 10\%$ (b), $\Theta = 15\%$ (c), $\Theta = 30\%$ (d) after 2 days of annealing at 300K.

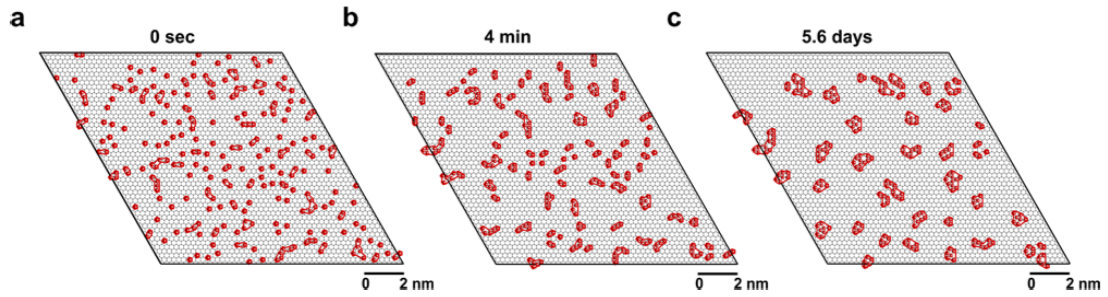

Figure 4.2: Clusterization process of epoxides in a $\Theta = 5\%$ rGO monolayer at 300K, at the beginning of KMC simulation (a), after 4 minutes (b) and after 5.6 days (c). Epoxides, shown as red dots, are magnified to highlight their positions on the large supercell. Figure reproduced from [93] with permissions from ACS.

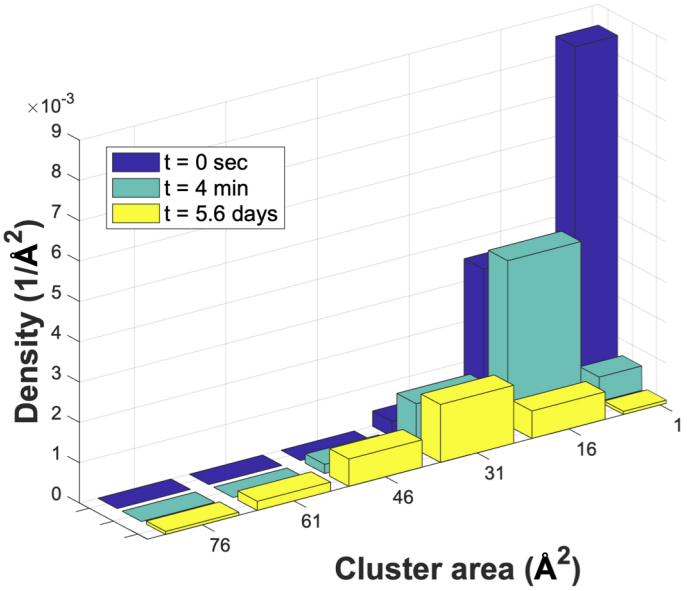

Figure 4.3: Cluster size density distribution as a function of time (snapshots at t = 0, t = 4 minutes and t = 5.6 days) of a $\Theta = 5\%$ rGO monolayer annealed at 300K. Figure reproduced from [93] with permissions from ACS.

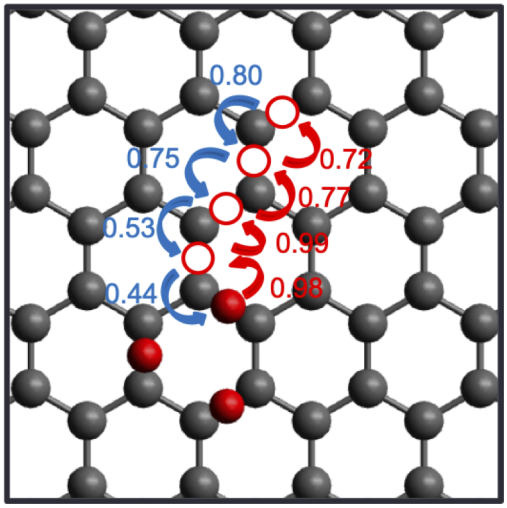

Figure 4.4: Diffusion barriers for an epoxide to attach (blue) and detach (red) from an epoxide pair. The potential barriers faced by an epoxide to detach from a stable pair are much higher than to attach to that pair.Figure reproduced from [93] with permissions from ACS.

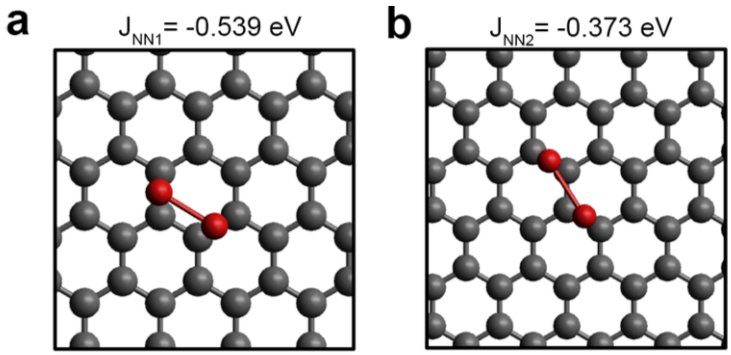

Figure 4.5: Optimal epoxides pair figures used for CE and their relative ECIs. Lower energy values mean more stable configurations, since the interaction between epoxides lowers the total energy. Figure reproduced from [93] with permissions from ACS.

4.4 High-temperature treatment

In this section, we investigate the formation of pores in monolayer rGO when exposed to high temperatures, following the desorption of carbons and oxygens as CO and CO_2 molecules, observed for the first time by Brodie and studied by Larciprete and collaborators using DFT [39]. These authors investigated mechanisms of thermal reduction in GO based on experimental characterizations, DFT and NEB simulations and

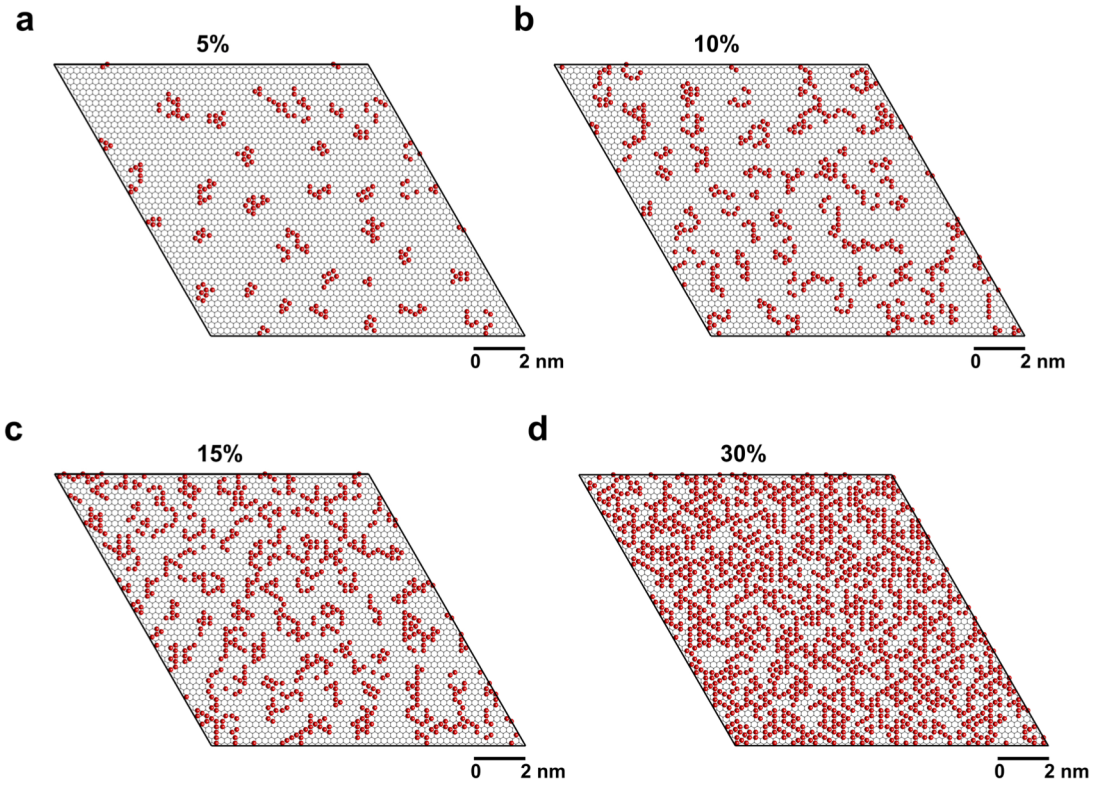

Figure 4.6: Results of 2 days annealing at 300K of rGO monolayers at different coverages: $\Theta = 5\%$ (a), $\Theta = 10\%$ (b), $\Theta = 15\%$ (c), $\Theta = 30\%$ (d). Figure reproduced from [93] with permissions from ACS.

identified epoxide species at high concentrations as responsible for the destruction of the graphitic backbone of GO at high temperatures. Based on these evidences, and on conclusions from [114], we focused our efforts on investigating the possibility to exploit high temperature thermal reduction to create holes in correspondence of epoxide clusters in rGO, for accurate and precise fabrication of porous monolayers. After studying the clusterization of epoxide species in rGO, we concluded that mild annealing is an effective way to promote the formation of oxidized areas of controlled dimensions. In particular, we provided quantitative data demonstrating that by carefully selecting the initial oxidation level of rGO sheets and by tuning temperature and time of the mild annealing procedure it is possible to finely control shape and size of oxidized clusters. We will now discuss the effects of high temperature annealing on these clusters and provide quantitative relationships between the dimensions of initial clusters, treatment conditions and the dimensions of final pores, based on accurate MD simulations.

We first modeled rGO structures as graphene supercells with a cluster of epoxides

and hydroxyls at the center, considering –O–/–OH = 0.33 and –O–/–OH = 3.00 as representative respectively of clusters with a majority of hydroxyls and clusters with a majority of epoxides and ethers. To model high temperature annealing we used classical MD with ReaxFF to run simulations at different temperatures: 1000 K, 1500 K and 2500 K.

Analyzing rGO structures after thermal annealing, we first observed that pores are only formed in the oxidized region, whereas pristine graphene areas remain intact. Observing samples with different compositions, annealed at different temperatures, we could also conclude that carbon desorption is very dependent on –O–/–OH ratio and treatment temperature. In fact, during annealing at low temperature (1000 K), we observed the formation of CO_2 and O_2 molecules only with those structures containing a majority of epoxides and ethers, while H_2O formation is predominant when there is a majority of hydroxyls (Figure 4.7(b)). Increasing temperature (1500 K) CO molecules start forming (in equal rates for both compositions), the formation of CO_2 also increases (mainly when more epoxides are present). At this temperature, when a majority of hydroxyls are present, we observed the formation of large amounts of water (Figure 4.7(c)). At the highest temperature (2500 K) we observed the formation of large quantities of CO and CO_2, almost independently on the –O–/–OH ratio of annealed structures (Figure 4.7(d)). From Figure 4.7(a) we can immediately observe that the mean area of final pores is directly proportional to the annealing temperature. While for lower temperatures higher concentrations of epoxides are needed to produce pores of appreciable size, at 2500 K the pores mean area is independent of the –O–/–OH ratio with the only difference being that higher concentrations of hydroxyls determine a higher standard deviation. We can conclude from this first analysis that epoxide groups are more efficient in producing pores in rGO and therefore we can recommend to process rGO flakes with higher concentrations of epoxide groups to physically produce monolayer porous membranes. As a procedural remark, to measure pores area we modeled each atom as a sphere with correspondent Van der Waals radius and considered the steric hindrance of each atom decorating the pore.

To consider the role of local cluster concentration on the efficiency of carbon removal during high temperature annealing, we also investigated how the local oxygen atomic concentration influences the area of final pores and observed that high local concentrations are needed to consistently produce pores, in agreement with Larciprete [39] and Kumar [114]. We simulated structures with two different local atomic coverages: 12.5% and 25.3%. From results shown in Figure 4.8(a), it is clear that a high local concentration of epoxide is needed to form pores in rGO and that the mean area of these pores depends on the annealing temperature. Moreover, Figure 4.8(b) shows that the final average pore area strongly depends on the initial cluster mean area, making these three physical quantities (initial clusters area, concentration and treatment temperature) of fundamental importance for controlled pores formation in rGO.

The last aspect that we studied is that of the shape of the initial cluster and its influence on the effectiveness of thermal treatments to produce pores in rGO. As we previously discussed in this chapter, we discovered that two epoxide pair configurations are particularly stable (Figure 4.5) one that generally leads to compact circular clusters (a) and the other chains of epoxides along a zig-zag line (b). As the maximization of these two configurations lead to increasingly stable clusters, they are of extreme relevance in the process of pores formation from epoxide clusters. For this reason, we simulated the evolution at high temperature (2500 K) by means of classical MD of different possible cluster arrangements: linear zig-zag line, two parallel zig-zag lines, a square made of three parallel lines and a circular packed cluster made of epoxide pairs. As we can see in Figure 4.9, linear configurations hardly lead to pore formation, as epoxides desorb as O_2 molecules without damaging C–C bonds, while with squared or packed clusters we observe a substantial increase in the resulting pore area. To further confirm this behavior, we simulated the thermal annealing at 2500 K of a selected structure containing a cluster which is the combination of circular and linear configurations. As it is shown in Figure 4.10, after the annealing only the packed circular part of the cluster induced a breaking of C–C bonds and formed a pore, while the linear part of the cluster had the only effect of producing defects in the graphitic plane, confirming our previous observations.

4.5 Conclusions and perspectives

Theoretical simulations demonstrated that to achieve high selectivity toward salt ions and good water flux, when using monolayer graphitic membranes for water desalination, the optimal pores diameter is 5.5 Å [30]. Nonetheless, the fabrication of such porous 2D membranes remains a formidable challenge, due to extreme difficulties in fabricating single layer graphene flakes with such narrow and uniform pores. In this chapter we investigated a consistent fabrication procedure that involves the use of monolayer rGO as a substitute of graphene, to exploit its intrinsic chemo-physical properties to engineer pore formation. The foundations of this work laid on considerations from Kumar and collaborators [114] for which a preliminary mild thermal annealing, promoting a clusterization of oxygen-containing groups, is an effective way to increase the efficiency of pore formation in rGO flakes during harsh thermal treatments.

We investigated the mechanisms driving the formation of epoxide clusters in rGO and we simulated their evolution, with atomic resolution, on the same time scale as experiments (days) [114]. In this way we proved the existence of a direct relationship between annealing time and temperature and the area of resulting epoxide clusters, that can be exploited to finely tune the size of oxidized areas by controlling annealing time, temperature and initial rGO coverage. We also provided quantitative data that can be used directly to estimate experimental conditions to produce pores of desired size. From these evidences we could also conclude that structures with low initial coverage ($\Theta \leq$

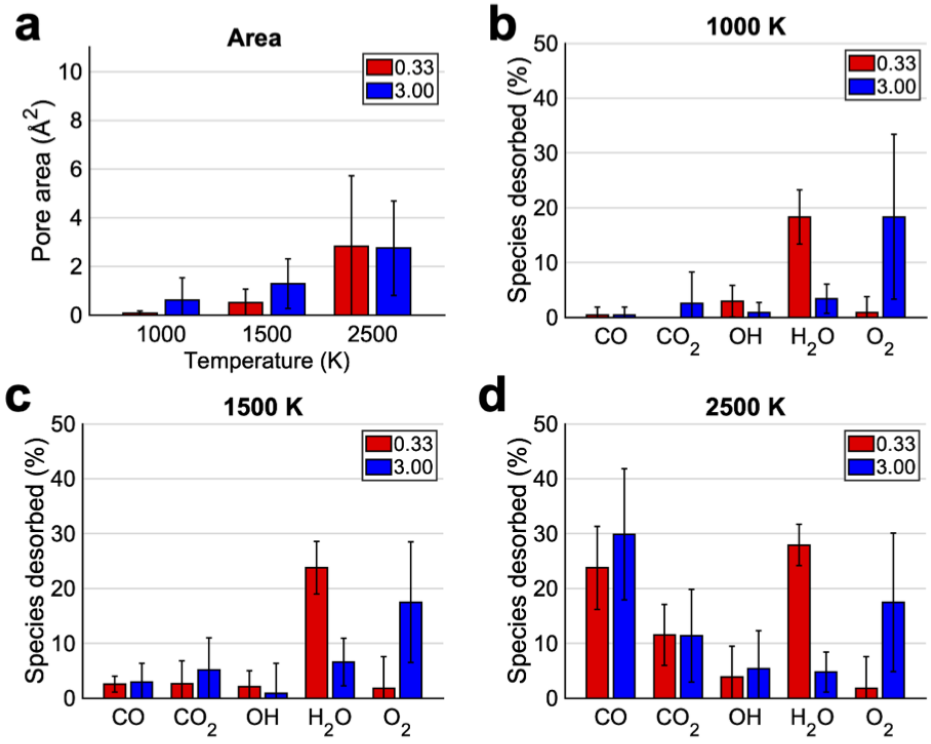

Figure 4.7: Final pore area as function of temperature and –O–/–OH (a); percentage of oxygen-containing species desorbed as CO, CO_2, OH radicals, H_2O and O_2 when rGO structures with different –O–/–OH are annealed at 1000 K (b), 1500 K (c) and 2500 K (d).

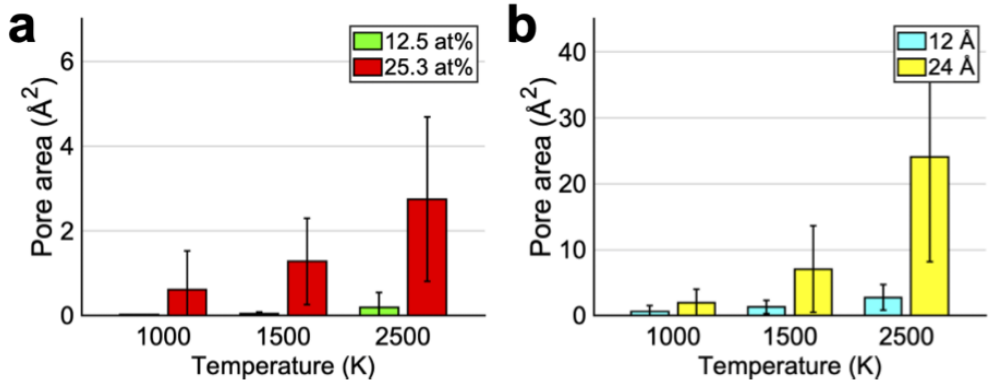

Figure 4.8: Pore area as function of annealing temperature, (a) epoxides concentration (12.5 at% or 25.3at%) in the cluster and (b) initial cluster area (12 Åor 24 Å).

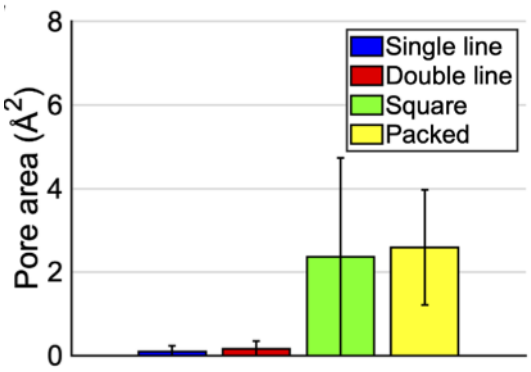

Figure 4.9: Final pore area after annealing at 2500K, starting from single line, double line, square and circular (packed) cluster.

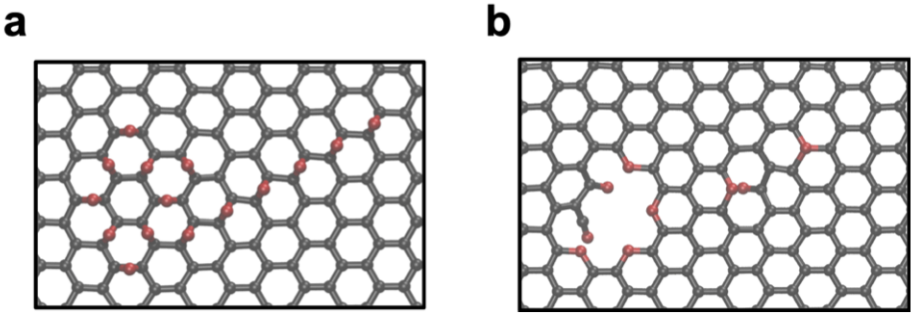

Figure 4.10: Composite cluster, made from a circular-shaped core with a linear tail. After annealing at 2500K only the circular part of the cluster produced a pore in the graphitic layer, while the linear tail only yielded point defects.

10%) determine the formation of circular clusters, while for higher initial coverages a prevalence of linear configurations was observed.

After highlighting the experimental conditions to promote controlled clusterization, we studied the removal of carbon atoms from these oxidized areas at high temperatures as a way to produce pores with uniform size in monolayer rGO. We concluded that pores are only formed in correspondence of initial clusters, while pristine graphene regions remained intact, and that their area is strongly dependent on the shape and oxidation degree of initial clusters, on their size and on annealing temperatures. The best conditions in terms of carbon removal were observed when using rGO structures containing large and dense circular clusters, processed at very high temperatures.

Based on this work, we suggest a two-step experimental treatment that allows to consistently generate pores of controlled size in rGO monolayers, consisting of a first

mild annealing to precisely engineer the morphology of the flake and a successive high-temperature treatment to create pores of accurate and uniform size. We expect such a method to allow for a much easier application of single layer graphitic membranes for water desalination, with its consequent benefits in terms of power consumption of reverse osmosis desalination plants, as we discussed in Chapter 1.5.1. As a final remark, a realistic application of this experimental procedure to the production of desalination membranes requires the use of rGO flakes with very low initial defectivity, in order to avoid the presence of uncontrolled holes that would undermine the proper functioning of membranes. In this sense, GO fabricated by conventional methods is unfit for this use, due to typically high defect densities as we have seen in Chapter 1.2. To overcome these difficulties it is required to use fabrication techniques for the initial GO that preserve the graphitic structure intact, typically by keeping low reaction temperatures as we have also seen in Chapter 1.2 [1] or by soft-oxidation of graphene [123].

Chapter 5

Interactions between water, single and multilayer rGO

5.1 Introduction

In this Chapter we will investigate the interactions between rGO and water, using *ab initio* MD simulations to model the evolution of selected structures, representing realistic rGO stoichiometries, in water at room temperature. We will analyze the modifications induced by water on rGO monolayers, as well as the effects of the surface on the properties of interfacial water. Particular attention will be given to understanding how oxygen-containing groups in rGO evolve and how different groups interact with water through hydrogen bonds.

We will also address how the composition of rGO influences its surface wettability, by analyzing the electric dipole of water molecules and their vibrational spectra. These are fundamental physical quantities to analyze the nature of water at a solid-liquid interface and provide important information about the characteristics of the hydrogen bond network in interfacial water, giving clear indications about surface wettability.

Finally, we will study the effects of confinement on water between rGO flakes, with particular focus on the diffusivity of water molecules. As we discussed in Chapter 1.5.1, permeation is one of the key factors that influence the performance of reverse osmosis membranes and high water permeation rates are crucial to increase membrane efficiency. Considering realistic distances between rGO layers in our models, our goal is to understand how rGO composition influences water diffusivity near the interface. Our structures are meant to represent multilayer rGO membranes soaked in water, with applications as water treatment membranes.

5.2 Simulation Strategy

To investigate the transformations of rGO in water and study the properties of the interfaces, after creating initial model structures representing rGO monolayers dispersed in water, as well as water confined between multilayer rGO, we simulated their evolution at room temperature by means of accurate Car-Parrinello MD simulations. To this extent we ran NVE MD of each interface sample for 10 ps after a 2 ps equilibration at 400 K, since it was reported in the literature that at this temperature DFT-based MD dynamics using PBE yields results in agreement with experiment for structural and dynamical properties at room temperature [124][125][126]. We analyzed MD trajectories in terms of water mass density distribution, water electric dipoles orientation and modulus in order to investigate rGO surface wettability and the modifications induced in water by the interface, as a function of the material composition. Finally, we investigated water diffusivity through multilayer rGO membranes, by computing the mean squared displacement of water molecules confined between rGO sheets with an interlayer distance of 13.7 Å. This allowed us to compute the self-diffusivity coefficient of water molecules confined between rGO layers with different compositions and observe how it is influenced by the presence of different oxygen-containing species.

5.2.1 Initial model structures

We created a set of initial interfaces to represent monolayer rGO in contact with water considering different rGO compositions. To this extent we created 12.83 Å × 12.35 Å graphene supercells containing 60 carbon atoms, over which we uniformly distributed epoxide and hydroxyl species, according to the following atomic percentages: 10%–O– 0%–OH; 0%–O– 10%–OH; 20%–O– 10%–OH; 10%–O– 20%–OH. In order to model a monolayer dispersed in water, we used a supercell perpendicular to the rGO layer of 25Å (considering PBC), which is enough to ensure a correct description of bulk water far from the interface, based on a study of graphene in water from Cicero and collaborators [126]. We included 108 water molecules in these structures in order to have a water density $\rho = 1\frac{g}{cm^3}$ within the simulation domain. Water molecules were distributed in the simulation domain according to a TIP4P model using the "gmx solvate" function of GROMACS [127], to achieve $\rho = 1\frac{g}{cm^3}$. We confirmed the accuracy of this method by means of preliminary classical MD simulations at ≃300 K that confirmed the expected mass density distribution. As we will see in Section 5.4, this configuration allowed us to describe accurately the characteristics of water at the interface with monolayer rGO, as well as its bulk properties far from the interface. In Figure 5.1 is reported an example of an rGO monolayer dispersed in water.

We also defined another set of initial structures, this time representing multilayer rGO samples soaked in water. To this extent we defined rGO supercells with the same lateral dimensions and compositions as in the previous case, fixing the interlayer distance between replicas to 13.7 Å in order to model the thickness of actual nano-channels

between rGO sheets in multilayer membranes. In fact, it is reported in the literature that multilayer GO membranes swell in presence of water, with the average interlayer distance between flakes ranging from $\sim$ 6 Å when completely dry, to $\sim$ 14 Å when completely soaked in water [128]. Therefore our initial models accurately describe typical experimental conditions of multilayer rGO membranes. In this case we determined that 59 water molecules were necessary to yield a water density $\rho \simeq 1 \frac{g}{cm^3}$ (keeping the same x and y supercell size dimensions described above) and performed preliminary classical MD simulations to validate the choice. In Figure 5.2 is reported an example of a multilayer rGO model structure soaked in water.

For each possible rGO composition and interlayer distance we created 10 different structures and selected the one with lowest ground-state energy as the most stable. For this reason, all structures were relaxed by means of plane waves based DFT as implemented in Quantum Espresso [79], using the PBE functional for exchange and correlation [72] and ultrasoft pseudopotentials [118]. Electronic wavefunctions were expanded up to an energy cutoff $E_{cut} = 36$ Ry, the Brillouin zone was sampled with a $(2 \times 2 \times 1)$ Monkhorst-Pack grid, while to relax atomic positions forces were minimized down to 26 meV/Å.

As reference for later comparisons with rGO-water structures, we also created two samples of graphene-water interfaces with respectively 25 Å and 13.7 Å interlayer distances.

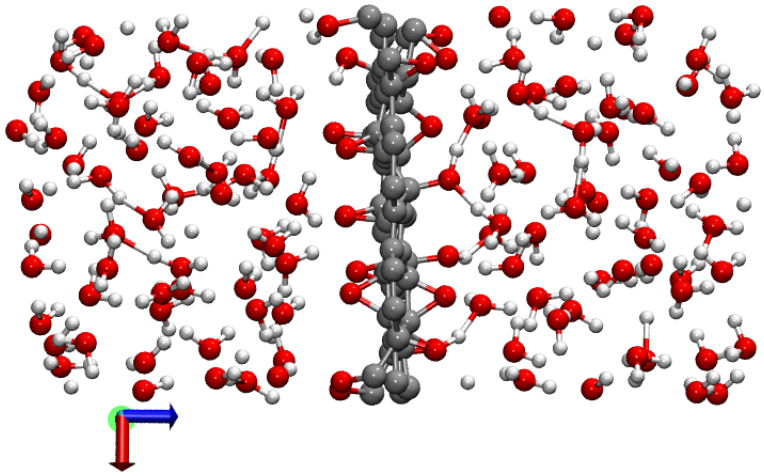

Figure 5.1: Example of rGO monolayer (20% –O– 10% –OH) in water. The supercell along z direction (blue axis), perpendicular to the interface, is 25 Å long.

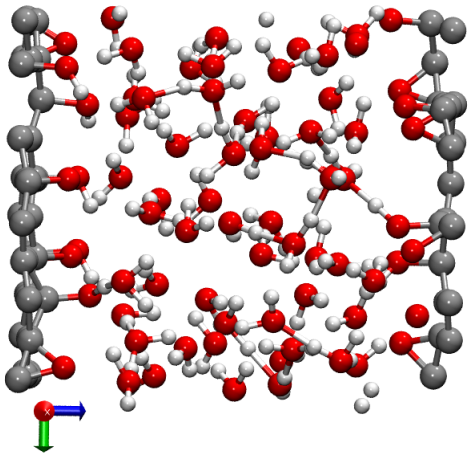

Figure 5.2: Example of multilayer rGO (20% –O– 10% –OH) soaked in water. The supercell along z direction (blue axis), perpendicular to the interface, is 13.7 Å long.

5.2.2 Car-Parrinello Molecular Dynamics

CP MD simulations were performed using the Quantum Espresso suite [79], with PBE exchange and correlation functional [72] and ultrasoft pseudopotentials [118]. Electronic wavefunctions were expanded up to an energy cutoff $E_{cut} = 36$ Ry and the Brillouin Zone was only sampled at Γ. CP MD was performed using an electron fictitious mass $\mu = 200$ a.u. and a timestep $dt = 4$ a.u. for Verlet integration of the equations of motion. In all MD simulations we substituted hydrogen atoms with deuterium atoms, in order to improve total energy conservation for a given integration timestep due to the lower vibrational frequency of O–D bonds. For the sake of readability we will address D_2O and –OD as H_2O molecules and –OH groups in the following. For each interface model, after the initial system setup and electronic energy minimization, we increased the temperature of our system from 0 K to 400 K by means of velocity rescaling and equilibrated the system for 2 ps. To this extent, we payed particular attention to have all different atomic species at similar temperatures (400 K) and avoid the presence of hot or cold species that would impair the accuracy of the investigation. When the system temperature stabilized, after 2 ps, we performed 10 ps of microcanonical (NVE) MD during which we collected data for trajectory analysis. Although temperature control was not applied during these 10 ps, in all cases the system temperature remained stable at 400 K as set initially.

5.2.3 Computation of water molecules diffusivity

In this section we describe how to compute the self-diffusion coefficient of molecules from a MD trajectory. This quantity describes the motion of particles in the absence of external forces acting on them, such as for example any gradients that create a net

flux. We used the Einstein relation to compute the self-diffusion coefficient of water molecules from their mean squared displacement during MD simulations. The Einstein relation defines a proportionality between the mean squared displacement of particles and the observation time, provided that the latter is sufficiently long (ideally infinite):

$$D = \frac{1}{2d} \lim_{x \to \infty} \frac{\langle [r(t_0 + t) - r(t_0)]^2 \rangle}{t} \tag{5.1}$$

where d is the dimensionality of the system, r is the position of particles and finally D is the average self-diffusion coefficient of those particles in the atomic system.

In this work, we averaged the mean squared displacement over all water molecules and over all time origins, as suggested by Keffer [129]. In fact, we defined several time origins (a different time origin every MD snapshot in the first half of the trajectory) to evaluate the mean squared displacement of water molecules, in order to improve sampling statistics by averaging over many values of the latter. After obtaining the mean squared displacement, the self-diffusion coefficient is obtained performing a least square regression of the curve that it defines as a function of time, neglecting the early steps of the dynamics when particles' motion is in a ballistic regime. Indeed, the slope of this fitting represents the self-diffusion coefficient, as defined in Equation 5.1.

5.3 Interactions between rGO and water

Based on observations on the evolution of oxygen-containing species in monolayer rGO soaked in water during MD simulations, we identified four common species: epoxides, 1,2-ethers, negatively charged oxygens (O^-) and hydroxyls. We soon observed from these dynamics the tendency of some epoxide and hydroxyl groups to evolve in O^- species, either by breaking a C–O bond (epoxide breaking) or by losing an hydrogen (–OH deprotonation). We will discuss more specifically the evolution of oxygen-containing groups in the next section while analyzing MD trajectories of monolayer rGO samples in water, although it is worth mentioning that while epoxides, ethers and hydroxyls are stable in dry conditions, O^- groups only form in presence of water. Understanding the interaction between these specific oxygen-containing groups and water molecules is fundamental to investigate their influence on surface wettability, therefore we created additional model structures containing only the specific isolated oxygen-containing species and one or two water molecules. These structures were used to estimate the strength of hydrogen bonds (H-bonds) between water molecules and oxygen-containing groups in rGO, by means of accurate DFT simulations (details for these calculations are the same as reported in Subsection 5.2.1 relative to DFT relaxation). For epoxide (Figure 5.3 A), 1,2-ether (Figure 5.3 B) and hydroxyl (Figure 5.3 D and E) groups we computed the H-bond energy as the difference between the energy of the relaxed rGO sample with one water molecule ($E_{sys}^{H_2O}$), the energy of the relaxed rGO sample without water (E_{sys}) and the energy of a water molecule ($E_{mol}^{H_2O}$):

$$E_{H-bond} = E_{sys}^{H_2O} - E_{sys} - E_{mol}^{H_2O} \tag{5.2}$$

In the case of an hydroxyl species, this can either be an H-bond donor (Figure 5.3 D) or acceptor (Figure 5.3 E). O^- groups (Figure 5.3 C) on the other side, only exist in presence of water and indeed we discovered performing DFT relaxations that they need at least two water molecules to stabilize at ground state (with one water molecule, epoxides are favored). For this reason we computed the H-bond energy between an O^- species and a single water molecules as:

$$E_{H-bond} = \frac{E_{sys}^{H_2O} - E_{sys,constr} - 2E_{mol}^{H_2O}}{2} \tag{5.3}$$

where $E_{sys,constr}$ is the energy of a rGO system without water, where the oxygen atom was constrained to remain vertical during DFT relaxation.

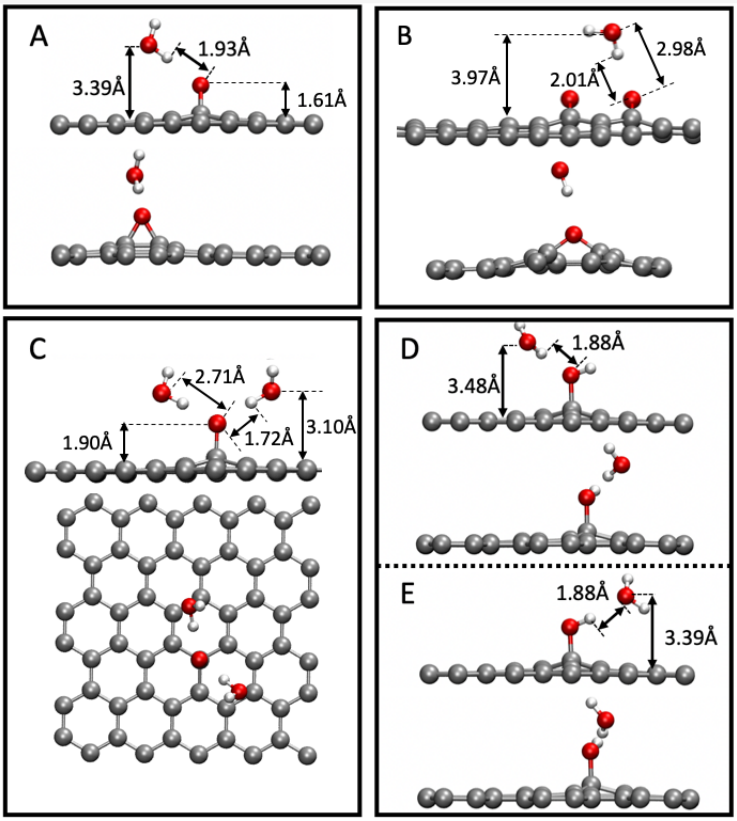

Figure 5.3: Relaxed structures modeling the interaction between (a) an epoxide group and a water molecule, b) two 1,2-ethers and a water molecule, c) one O^- and two water molecules, d) one hydroxyl group (donor) sharing its lone pairs with a water molecule and e) one hydroxyl (acceptor) interacting with lone pair from a water molecule.

From our calculations, the H-bond energy between an epoxide species and a water molecule at ground state is $E^{epo}_{H-bond} = -0.20$ eV, slightly lower than the H-bond energy of a water dimer computed at the same conditions ($E^{H_2O}_{H-bond} = -0.22$ eV). The relaxed distance between the epoxide and the oxygen in the water molecules is $d_{O-O} = 2.90$ Å, the distance between the epoxide and the hydrogen in the water molecule is $d_{O-H} = 1.93$ Å, while the distance between the oxygen in the water molecule and the graphitic plane is $d_{O-C} = 3.39$ Å, as reported in Figure 5.3 A.

For the interaction between a 1,2-ether species and a water molecule, we computed a H-bond energy $E^{eth}_{H-bond} = -0.14$ eV which is lower than the H-bond energy between water and an epoxide species, indicating a weaker interaction of water with 1,2-ether groups in rGO.

In the case of O^- groups, we computed a H-bond energy between this species and one water molecule $E^{O^-}_{H-bond} = -0.43$ eV which instead is considerably higher than the H-bond energy of a water dimer ($E^{H_2O}_{H-bond} = -0.22$ eV), highlighting a very strong affinity between water and O^- groups in rGO. After relaxation to ground state energy, the two water molecules are positioned with their hydrogens in proximity to the O^- in a configuration which is almost perfectly symmetrical. The distance between the O^- and the oxygen in one water molecules is $d_{O-O} = 2.71$ Å, the distance between the O- and the hydrogen in one water molecule is $d_{O-H} = 1.71$ Å, while the distance between the oxygen in the water molecule and the graphitic plane is $d_{O-C} = 3.10$ Å, as reported in Figure 5.3 C.

Finally, for hydroxyl species where the oxygen shares its lone pair with a water molecule (donor –OH, Figure 5.3 D) we computed a H-bond energy $E^{-OH,don}_{H-bond} = -0.24$ eV, whereas for acceptor hydroxyl species (acceptor –OH, Figure 5.3 E) we computed a H-bond energy $E^{-OH,acc}_{H-bond} = -0.23$ eV. These energies are comparable, showing that in either configurations –OH groups have similar interactions with water, as H-bond energies are comparable with that between two water molecules ($E^{H_2O}_{H-bond} = -0.22$ eV), highlighting a good affinity between water and –OH groups in rGO.

5.4 Surface wettability and interfacial water properties

In this section we investigate the wettability of rGO monolayers as a function of their composition. To this extent, as discussed in Section 5.2.1, we created models representing rGO with different degrees of oxidation ($\Theta = 10\%$ and $\Theta = 30\%$) and –O–/–OH ratios, and simulated their evolution in water at 400 K for 20 ps by means of CP MD. As a reminder, these interface models contain 108 water molecules with a distance between rGO replicas of 25 Å, which, as we will see, is enough for water to recover its bulk properties in the middle of the water slab.

As we saw in the previous section, based on calculated H-bond energies between

isolated oxygen-containing groups in rGO and water molecules we could evaluate how strong each of these species interact with water and concluded that while O^- and –OH show a strong affinity with water, epoxide and especially 1,2-ethers interact with water via weaker hydrogen bonds. In this section we relate these data with the wetting properties of rGO monolayers containing combinations of these groups, analyzing three fundamental properties of interfacial water molecules: mass density distribution, O–H bond orientation distribution and electric dipole distribution. The analysis of water density perpendicular to the interface gives clear information about water structural properties, in particular about over-structuring near the surface, and allows to verify that water recovers its bulk characteristics away from the interface. We computed the density of water molecules as a function of the distance from graphene (rather than simply as a function of z coordinate) and averaged over all snapshots of the corresponding 20 ps MD trajectory. The orientation of O–H bond perpendicular to the interface (in Figure 5.4 are shown the definitions of O–H vector and θ angle) instead, allows to identify variations of the preferential orientation of water molecules and further highlights modifications induced by the surface to the H-bond network between H_2O molecules [126]. Also in this case we averaged bond orientations over all snapshots of the corresponding 20 ps MD trajectory. Finally, the average electric dipole distribution of water molecules provides an indication of the strength of the H-bonds between H_2O molecules, with lower dipole values suggesting a weakening of the H-bond network. We computed dipole moments by mean of maximally localized Wannier functions [130]. The electric dipoles of water molecules were computed for 20 different snapshots taken every 1 ps from the corresponding MD trajectory and the values reported in the followings are averaged over these 20 snapshots.

In Figure 5.5 are reported, as reference, the mass density distribution of carbon atoms and oxygens in water, the O–H bond orientation distribution and average electric dipole distribution of H_2O molecules for the case of graphene dispersed in water. This interface has been extensively investigated by Cicero and collaborators [126], which reported clear indications about the interactions between water and the hydrophobic graphene surface that we used to validate our method. From the mass density distribution of oxygen atoms in water molecules (Figure 5.5 a) it is possible to observe an exclusion layer, within 2.5 Å from the surface, where water does not penetrate, followed by a thin interfacial region where H_2O molecules accumulate. It is clear that after 5 Å from the interface the effects of the latter on water density becomes negligible, with the recovery of a bulk-like average density $\rho \sim 1 \frac{g}{cm^3}$ within 10 Å from the surface. High-density peaks are located respectively at -3.5 Å (A) and 3.5 Å (B) from the graphene surface and reach a density $\rho \sim 2 \frac{g}{cm^3}$. This is in good agreement with results from [126], where the authors found high-density water peaks extending from 2.5 Å to 5 Å with maximum density $\rho = 1.96 \frac{g}{cm^3}$. The O–H bond orientation density distribution of water (Figure 5.5 b) shows how molecules near the interface are preferentially

oriented with one hydrogen pointing toward graphene as highlighted by a higher density of O–H bonds corresponding to $\theta \sim 40° - 100°$ and $\theta \sim 140° - 170°$ near the right surface and corresponding to $\theta \sim 80° - 150°$ and $\theta \sim 15° - 45°$ near the left surface. The orientation of hydrogens toward graphene is also suggested by the mass density distribution of hydrogen atoms in water, which extend closer to the surface with respect to the mass density distribution of oxygens in water (Figure 5.5 a). Finally, we observed that the average electric dipole distribution of interfacial H_2O molecules (Figure 5.5 c) is reduced to about 2.7 D - 2.8 D near the surface, with respect to an average value of 3.1 D for water molecules in the bulk (farther than 5 Å from graphene), highlighting a weakening of the H-bond network near the surface as suggested in [126].

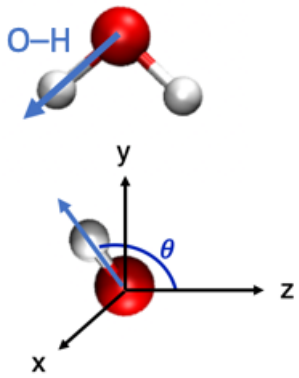

Figure 5.4: Definition of the O–H bond vector in water molecules and of the angle θ that we used in this work to evaluate preferential orientations of water molecules.

The interface between water and monolayer rGO is more complex than in the case of graphene, due to the presence of oxygen-containing groups in the structure of rGO that interact with water and evolve in time. As we saw in the previous section, these groups have different affinities with water molecules, yielding heterogeneous interactions when they are distributed in typical rGO samples. For this reason, a detailed atomistic investigation correlating the presence of specific oxygen-containing species (and their combinations) in rGO to modifications of surrounding water is fundamental to engineer applications of these interfaces. In Figure 5.6 are reported the atomic mass density distribution, the O–H bond orientation density distribution and average electric dipole distribution of H_2O molecules for the case of 10% –O– 0% –OH monolayer rGO in water. Oxygen-containing groups in rGO are located at -1.9 Å (C) and at 1.3 Å (D) from the graphitic surface. Differences between peaks C and D, both in terms of distance from the plane and density, are due to the transformation of one epoxide on the left face of rGO to an O^- species during the MD trajectory. After this transformation in the early stages of the dynamics, the rGO monolayer structure remained unchanged

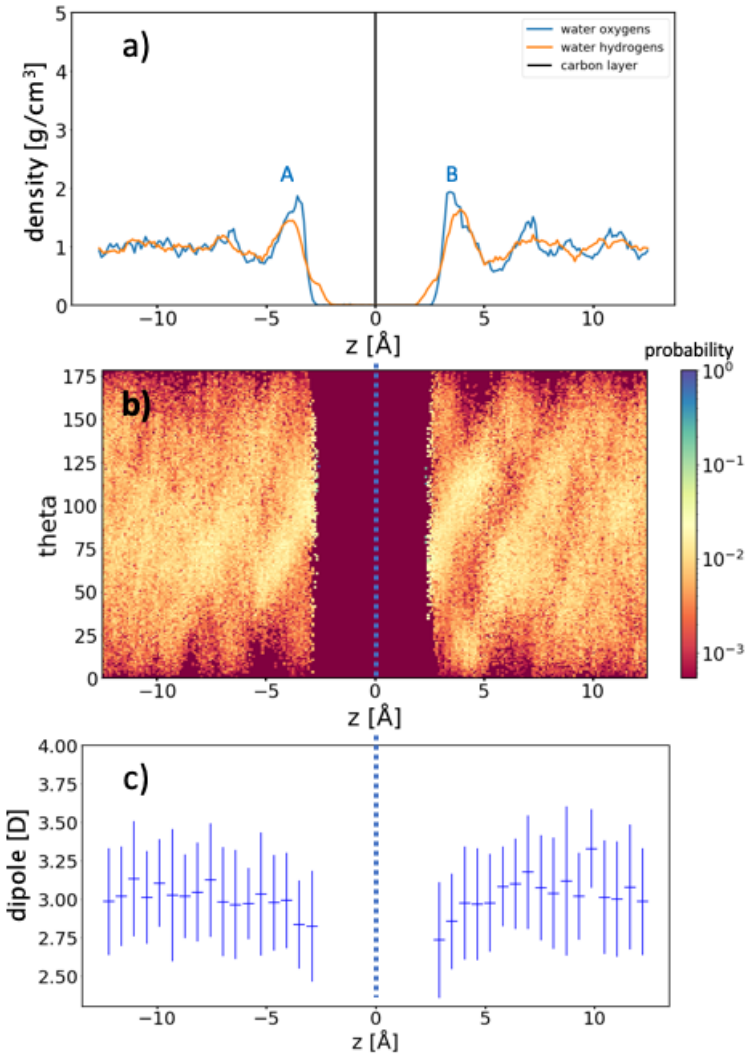

Figure 5.5: Graphene-water interface. Mass density distribution of oxygens in water, as a function of their distance from the graphene layer (a). O–H bond orientation density distribution of H_2O molecules (b). Average electric dipole distribution of H_2O molecules (c). The supercell is 25 Å along the z direction, perpendicular to the interface.

with 3 epoxide groups on its right surface and with 2 epoxides and 1 O^- on its left surface. As in the case of graphene, we observed an exclusion layer for water molecules within 2.5 Å from the graphitic surface. Water mass density shows two peaks at -3.9 Å (A) and at 3.4 Å (B) from the graphitic surface that reach a density $\rho \sim 1.65 \frac{g}{cm^3}$ (slightly less than in the case of graphene). From the O–H bond orientation density distribution of water we concluded that O–H bonds are less oriented toward the surface than in the case of graphene with higher densities of O–H bonds corresponding to $\theta \sim 15°$ –

120° near the right surface and corresponding to $\theta \sim 50° - 160°$ near the left surface. This conclusion is also confirmed by the mass density distribution of hydrogen atoms in water, which differently from the previous case almost completely overlaps with the mass density distribution of oxygens in water (Figure 5.6 a). Finally, we observed that the average electric dipole distribution of interfacial H_2O molecules is reduced to ∼2.8 D near the left surface and to ∼2.7 D near the right surface, with respect to an average value of 3.0 D for water molecules in the bulk. These data suggest that at such low coverage ($\Theta = 10\%$) the surface is mostly hydrophobic like graphene.

In Figure 5.7 we reported our results for the case of 0% –O– 10% –OH monolayer rGO in water. Hydroxyl groups on the left surface of the rGO monolayer are located around -2.1 Å (C) from the graphitic plane. On the right surface instead, one –OH group desorbed in the early stages of the dynamics and remained within the interfacial layer (as can be see from the tail of surface oxygen mass density at ∼7 Å), exchanging protons with neighboring water molecules. This initiated a series of reactions between short-lived –OH in the water interfacial layer and the 2 remaining –OH groups on the right surface of rGO. The latter oscillate between meta-stable states where they exchange protons with ions in water, transforming from –OH to O^- and vice versa during the whole dynamics. As a consequence, the mass density of surface oxygens presents two peaks, at 1.4 Å (D) and 1.8 Å (E) from the graphitic surface. The O–H bond orientation density distribution of water shows higher densities of O–H bonds corresponding to $\theta \sim 25° - 140°$ near the right surface and corresponding to $\theta \sim 45° - 170°$ near the left surface. This suggests that water molecules are slightly more oriented toward rGO with respect to 10% –O– 0% –OH case but still much less oriented than in the case of graphene. The extension of the mass density distribution of hydrogen atoms in water in proximity to surface oxygens in this case is due to the exchange of protons between rGO and water. Finally, we observed that the average electric dipole distribution of interfacial H_2O molecules is reduced to ∼2.8 D near the left surface and to ∼2.9 D near the right surface, with respect to an average value of 3.0 D for water molecules in the bulk.

Figure 5.8 shows our results for the case of 20% –O– 10% –OH monolayer rGO in water. On the left surface, two neighboring –OH lost a proton to a water molecule creating two vertical oxygens sharing the remaining proton, while remaining epoxides and –OH remained unchanged. The mass density of surface oxygens shows two peaks, at -2.1 Å (C) and -1.5 Å (D) from the graphitic surface. On the right surface of rGO instead, one –OH exchanged his proton with neighboring water molecules, creating a metastable O- that transformed back to a hydroxyl group within the first half of the trajectory. As a consequence, the mass density of surface oxygens shows a very pronounced peak, at 1.3 Å from the graphitic surface (E) and a small contribution around 1.8 Å (F) due to short-lived O^-. The O–H bond orientation density distribution of water shows higher densities of O–H bonds corresponding to $\theta \sim 15° - 130°$ near the right surface and corresponding to $\theta \sim 20° - 150°$ near the left surface. This suggests that interfacial water molecules tend to lay parallel to the surface near the right interface, while they

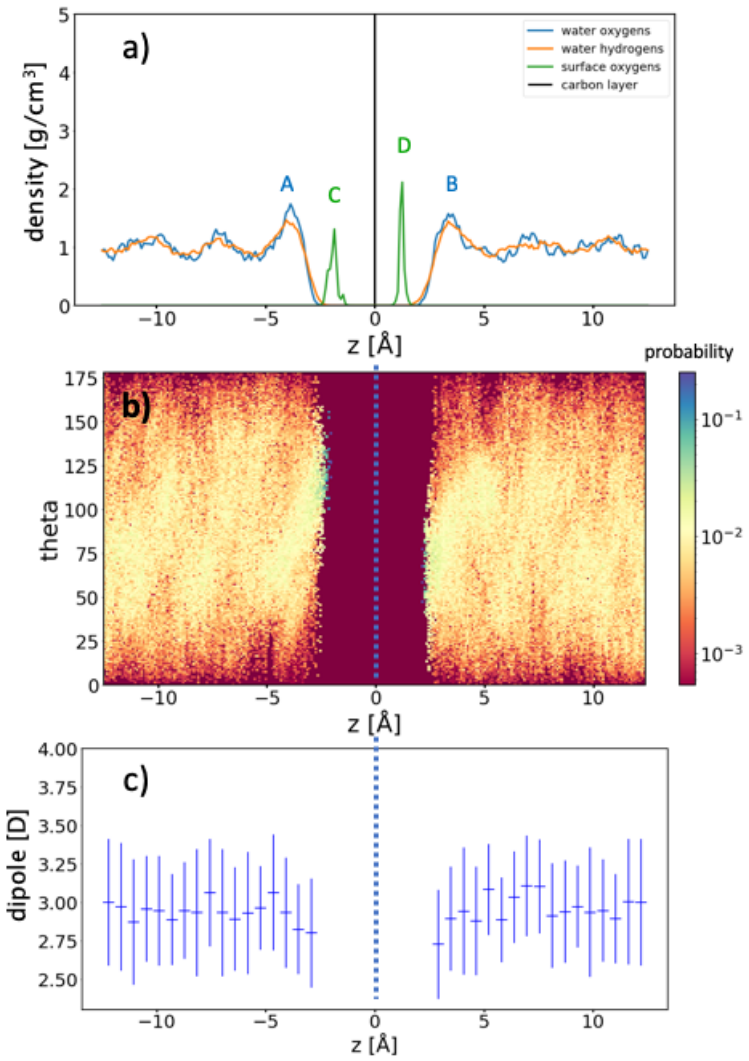

Figure 5.6: rGO-water interface (10% –O– 0% –OH). Mass density distribution of oxygens in water and surface oxygens-containing groups, as a function of their distance from the graphitic layer (a). O–H bond orientation density distribution of H_2O molecules (b). Average electric dipole distribution of H_2O molecules (c). The supercell is 25 Å along the z direction, perpendicular to the interface.

have O–H bonds oriented toward rGO near the left surface. The average electric dipole of interfacial H_2O molecules is ∼3.0 D near the left surface and ∼3.1 D near the right surface, almost unchanged with respect to molecules in the bulk suggesting that this surface does not reduce the strength of the H-bond network between H_2O molecules in the interfacial layers.

Finally, in Figure 5.9 we reported our results for the case of 10% –O– 20% –OH

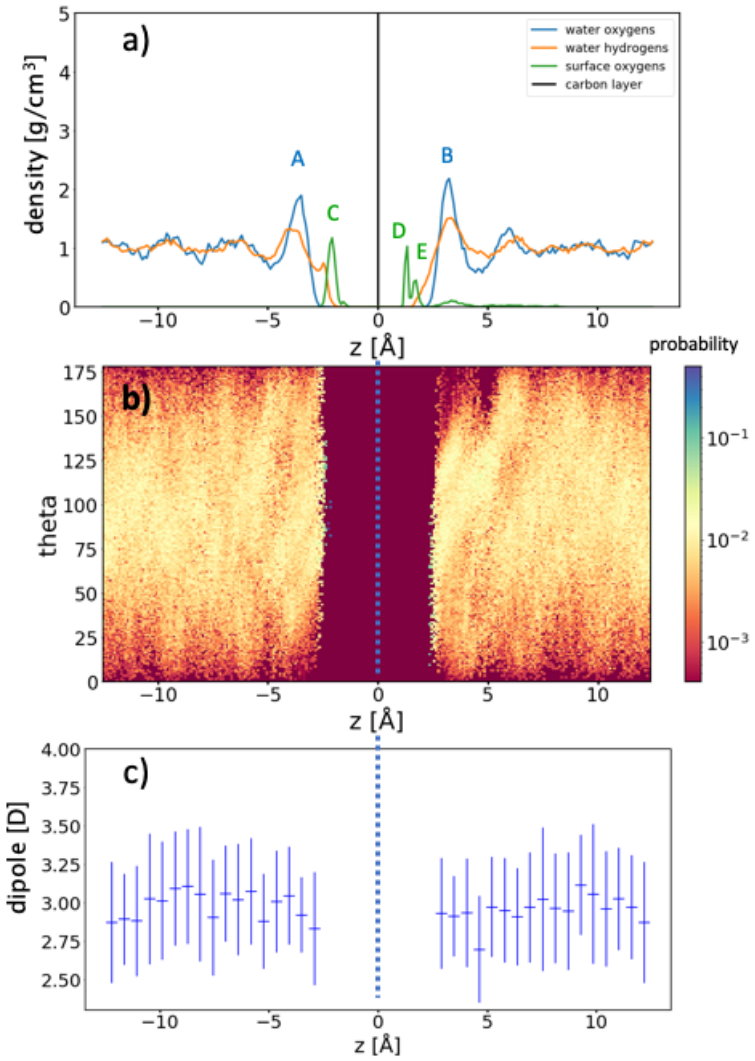

Figure 5.7: rGO-water interface (0% –O– 10% –OH). Mass density distribution of oxygens in water and surface oxygen-containing groups, as a function of their distance from the graphitic layer (a). O–H bond orientation density distribution of H_2O molecules (b). Average electric dipole distribution of H_2O molecules (c). The supercell is 25 Å along the z direction, perpendicular to the interface.

monolayer rGO dispersed in water. This rGO monolayer has a high initial coverage of oxygen-containing species that strongly interact with each other and with water molecules near the interface. In particular, on the left surface of rGO, epoxides transformed into O- species and started exchanging protons between each other, –OH groups and water molecules, creating metastable O^- and –OH species. As a consequence, the mass density of surface oxygens shows two peaks, at -2.1 Å (C) and -1.5 Å (D) from the

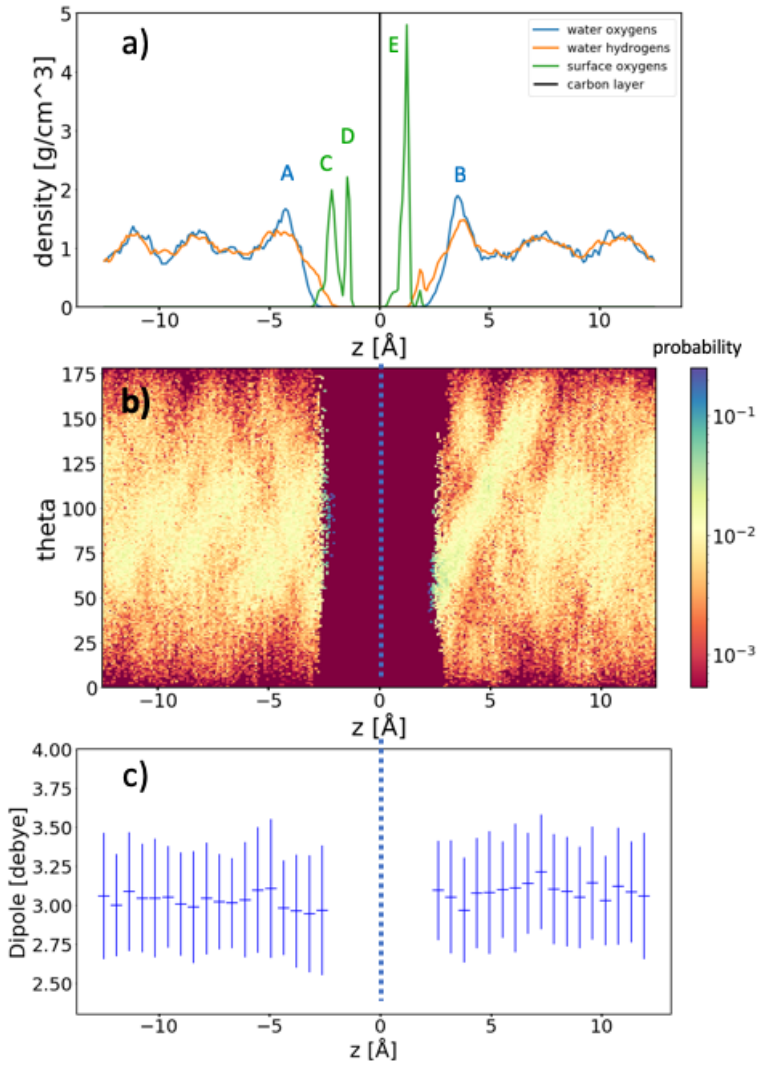

Figure 5.8: rGO-water interface (20% –O– 10% –OH). Mass density distribution of oxygens in water and surface oxygens-containing groups, as a function of their distance from the graphitic layer (a) . O–H bond orientation distribution of H_2O molecules (b). Average electric dipole distribution of H_2O molecules (c). The supercell is 25 Å along the z direction, perpendicular to the interface.

graphitic surface. The right surface instead is more stable, probably due to the presence of 1,2-ethers that do not engage in strong H-bonds, and we did not observe any transformation during the whole trajectory. In this case, the mass density of surface oxygens shows two peaks, at 0.8 Å (E) and 1.3 Å (F) from the graphitic surface. Interfacial water molecules lay parallel to the surface, with higher densities of O–H bonds corresponding to $\theta \sim 20° - 140°$ near the right surface and corresponding to $\theta \sim 40° - 170°$ near

the left surface. The average electric dipole of interfacial H_2O molecules is ∼3.1 D near the left surface and ∼3.2 D near the right surface, with respect to molecules in the bulk (∼3.1 D) suggesting that also this surface does not reduce the strength of the H-bond network between H_2O molecules in the interfacial layers.

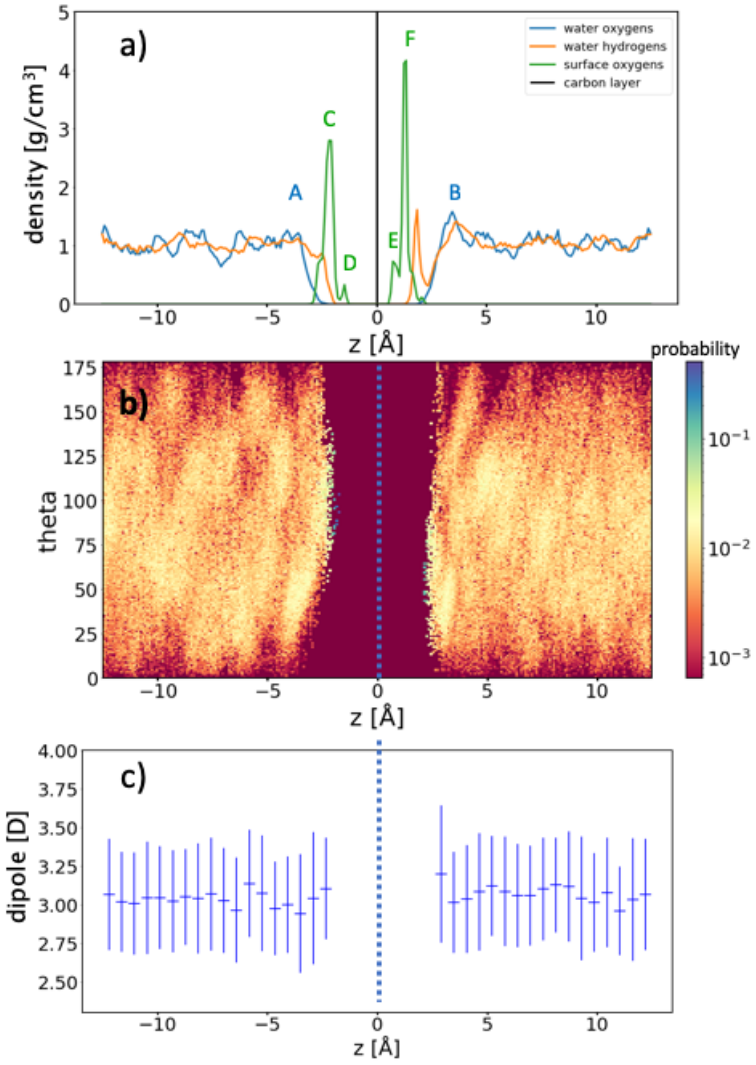

Figure 5.9: rGO-water interface (10% –O– 20% –OH). Mass density distributions of oxygens in water and surface oxygens-containing groups, as a function of their distance from the graphitic layer (a). O–H bonds orientation distribution of H_2O molecules (b). Average electric dipole distribution of H_2O molecules (c).

From the analysis of these data we concluded that of oxygen-containing species in rGO increase its hydrophilicity with respect to graphene. This is particularly evident when in presence of hydroxyl and O^- species, consistently with our findings that such

species interact strongly with water molecules through H-bonds. This is further confirmed by our results showing that the electric dipoles of water molecules near rGO surfaces containing a large number of –OH and O^- groups are slightly enhanced with respect to bulk water, highlighting the formation of a strong H-bonds network between water molecules and these species. Finally, we observed that at low coverages the effects of the hydrophobic graphene basal plane dominate the wettability properties of the rGO layer, as few isolated oxygen-containing groups are unable to create strong H-bonds network with interfacial water molecules.

5.5 Water confinement between rGO layers

In this Section, we investigate the effects of confinement between rGO flakes on the structural properties of water and on its diffusivity. We created atomistic models where 59 water molecules are confined between rGO sheets with an interlayer distance d =13.7 Å, as discussed in Section 5.2.1, to simulate their behavior in fully hydrated rGO multilayer membranes, which have been reported to have such interlayer distance [128]. Different degrees of oxidation –O–/–OH ratios were considered to model rGO, the same compositions examined in previous section for monolayer rGO samples and discussed in Section Section 5.2.1. For each model structure, we performed CP MD simulations at 400 K for ∼10 ps and analyzed the resulting trajectories in terms of water mass density distribution, O–H bond orientation and mean squared displacement. From the latter, as we discussed in Section 5.2.3, it is possible to compute the self-diffusion coefficient of water molecules, that we used to investigate the effects of confinement and of different rGO compositions on water diffusivity across multilayer rGO membranes.

In Figure 5.10 we reported, as reference, results for the hydrophobic graphene interface. Although graphite would have a much smaller interlayer distance (d ∼3.4 Å [32]), this fictitious multilayer graphene structure (with d =13.7 Å) allowed us to compare the self-diffusivity of water molecules confined between rGO and hydrophobic graphene layers at the same physical conditions. As we can see from the mass density distribution of H_2O molecules high-density peaks are located at 3.3 Å (A) and 10.4 Å (B), with their positions almost unchanged with respect to the interface with isolated graphene, although in this case the interfacial layers have higher peak densities $\rho_{max} \simeq 3.1 \frac{g}{cm^3}$. Moreover, due to confinement, water molecules never recover bulk properties, as indicated by oscillations in the mass density distribution at the center of the structure. The average orientation of water molecules near the surfaces, also resembles the case of isolated graphene with O–H bonds preferentially oriented toward graphene sheets ($\theta \sim 10°$ - $110°$ and $\theta \sim 130°$ - $160°$ near the left surface, $\theta \sim 15°$ - $45°$ and $\theta \sim 60°$ - $160°$ near the right surface). For H_2O molecules, we computed a self-diffusion coefficient $\overline{D_{xy}} = 6.6 \times 10^{-5} \frac{cm^2}{s}$ along x and y directions and $\overline{D_z} = 2.3 \times 10^{-5} \frac{cm^2}{s}$ along z direction. Comparing these self-diffusion coefficients with that computed by *ab initio* MD with PBE functional by Gygi and collaborators [131] for bulk water ($\overline{D_{xy}} = 2.9 \times 10^{-5} \frac{cm^2}{s}$ and

$\overline{D_z} = 5.88 \times 10^{-5} \frac{cm^2}{s}$), we could confirm that confinement of water between hydrophobic graphene layers enhances its lateral diffusivity with respect to the bulk, whereas it quenches perpendicular diffusivity.

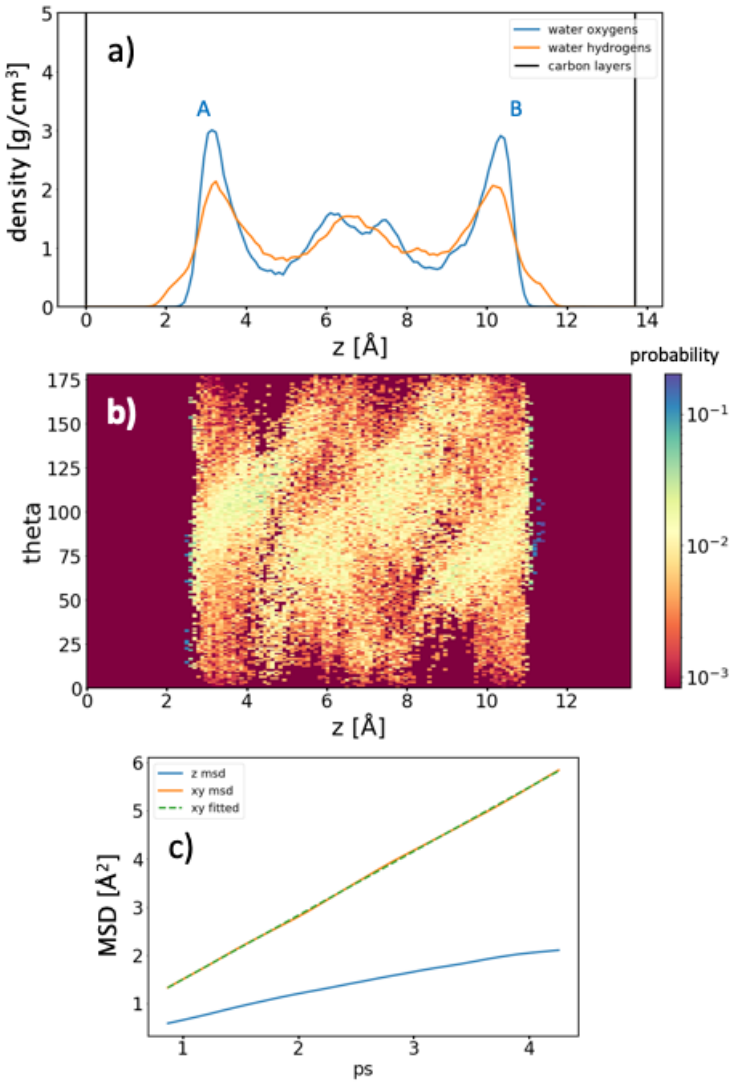

Figure 5.10: Water confined between graphene layers with interlayer distance $d = 13.7$ Å. Mass density distribution of oxygens and hydrogens in water, as a function of their distance from graphene layers (at 0 Å and 13.7 Å) (a). O–H bond orientation distribution of H_2O molecules (b). Mean squared displacement of H_2O molecules (c) along horizontal (xy) and perpendicular (z) directions with respect to graphene layers.

For what concerns water confinement between rGO layers, we reported in Figure 5.11 results from dynamics of water confined between 10% –O– 0% –OH rGO layers.

The high-density peaks in mass density distribution of H_2O molecules are located at (A) 3.0 Å and (B) 10.3 Å which are slightly closer to the graphitic surfaces with respect to the case of monolayer rGO (with the same composition). As we previously saw for staked graphene layers (with d =13.7 Å), water molecules never recover bulk properties. Epoxides on the left surface do not undergo any transformation during the MD and were located on average at 1.3 Å (C) from the graphitic plane. On the right surface instead, where one epoxide transformed into O^- species after ∼5 ps, the density peak of oxygen-containing groups is located at 11.9 Å (D). O–H bonds of interfacial water on average lay flat, almost parallel to the rGO surfaces, as demonstrated by the angles they form with the z axis ($\theta \sim 40°$ - $120°$ near the left surface, $\theta \sim 60°$ - $150°$ near the right surface), which are also consistent with the case of 10% –O– 0% –OH monolayer rGO that we examined in previous section. We observed that H_2O molecules had lower self-diffusion coefficients with respect to graphene confinement, both along lateral ($\overline{D_{xy}} = 2.5 \times 10^{-5} \frac{cm^2}{s}$) and perpendicular ($\overline{D_z} = 9.2 \times 10^{-6} \frac{cm^2}{s}$) directions. Lateral diffusion is comparable to the case of bulk water, whereas vertical diffusion is extremely reduced with respect to the bulk [131].

In Figure 5.12 we reported results from dynamics of water confined between 0% –O– 10% –OH rGO layers. The mass density distribution of H_2O molecules has two high-density peaks located at (A) 3.1 Å and (B) 10.0 Å. One –OH group on the left surface soon detached, while remaining within the interfacial water layer, and another one transformed in O^- releasing an hydrogen atom to surrounding water molecules. Hydroxyl groups on the right surface instead remained stable throughout the whole dynamics. These observations are confirmed by the presence of two peaks in the mass density distribution of surface oxygens adsorbed on the left surface, with one peak at 1.4 Å (C) corresponding to –OH groups and the other at 1.7 Å (D) corresponding to O^- species. Interfacial water molecules are slightly oriented toward rGO surfaces, with O–H bonds oriented between $\theta \sim 10°$ - $130°$ near the left surface and $\theta \sim 50°$ - $170°$ near the right surface. For H_2O molecules confined between 0% –O– 10% –OH rGO layers we computed similar self-diffusion coefficients along lateral ($\overline{D_{xy}} = 2.6 \times 10^{-5} \frac{cm^2}{s}$) and perpendicular ($\overline{D_z} = 6.3 \times 10^{-6} \frac{cm^2}{s}$) directions with respect to the previous case.

In Figure 5.13 are shown results from dynamics of water confined between 20% –O– 10% –OH rGO layers. The mass density distribution of H_2O molecules has two high-density peaks located at (A) 3.1 Å and (B) 9.9 Å. During the dynamics, one H_2O molecule adsorbed on the left surface of rGO, leaving an –OH and transforming a a O^- into another –OH, as can be seen from the surface oxygen distribution peaks at 1.4 Å (C) corresponding to –OH species and at 1.9 Å (D) corresponding to O^- species. On the right surface instead, one –OH deprotonated into a O^- and two peaks are present in the surface oxygen distribution, at 11.6 Å (E) and at 12.3 Å (F). Interfacial water molecules have O–H bonds oriented between $\theta \sim 15°$ - $130°$ near the left surface and $\theta \sim 40°$ - $160°$ near the right surface, highlighting that H_2O molecules are more oriented toward rGO near the latter. H_2O molecules showed low self-diffusion coefficients as

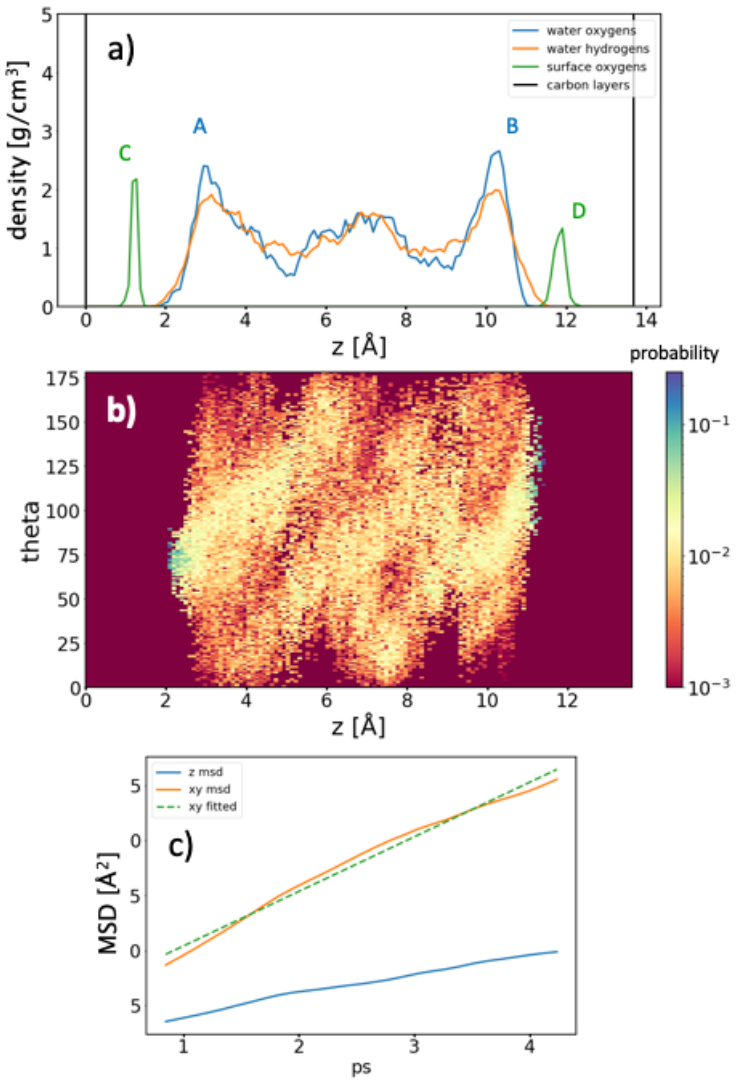

Figure 5.11: Water confined between rGO (10% –O– 0% –OH) layers with interlayer distance $d = 13.7$ Å. Mass density distribution of oxygens and hydrogens in water and mass density distribution of surface oxygens, as a function of their distance from the graphene layers (at 0 Åand 13.7 Å) (a). O–H bond orientation distribution of H_2O molecules (b). Mean squared displacement of H_2O molecules (c) along horizontal (xy) and perpendicular (z) directions with respect to graphene layers.

in the previous case with 0% –O– 10% –OH rGO layers: $\overline{D_{xy}} = 1.8 \times 10^{-5} \frac{cm^2}{s}$ and $\overline{D_z} = 8.3 \times 10^{-6} \frac{cm^2}{s}$.

Finally, in Figure 5.14 we reported results from MD of water molecules confined between 10% –O– 20% –OH rGO layers. The oxygen mass density distribution of H_2O

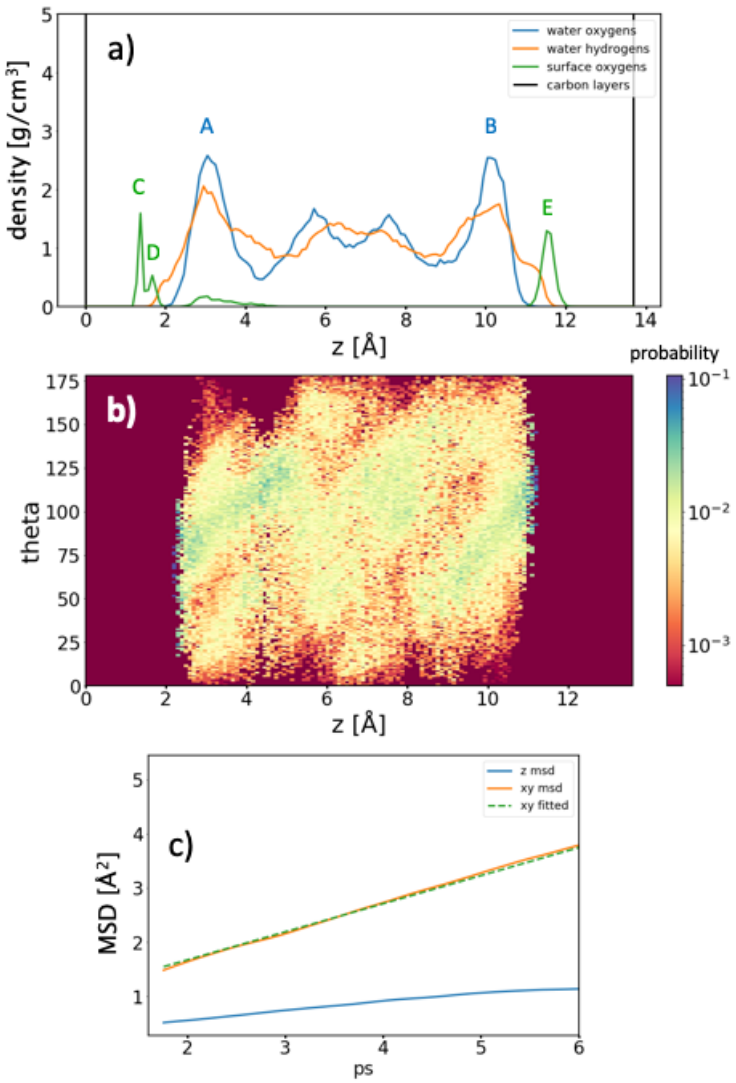

Figure 5.12: Water confined between rGO (0% –O– 10% –OH) layers with interlayer distance d =13.7 Å. Mass density distribution of oxygens and hydrogens in water and mass density distribution of surface oxygens, as a function of their distance from the graphene layers (at 0 Å and 13.7 Å) (a). O–H bond orientation distribution of H_2O molecules (b). Mean squared displacement of H_2O molecules (c) along horizontal (xy) and perpendicular (z) directions with respect to graphene layers.

molecules has two peaks at 3Å (A) and at 9.9 Å (B), while the mass density distribution of surface oxygens has two peaks near the left surface, at 0.9 Å (C) and at 1.4 Å (D), while it has one peak near the right surface at 11.5 Å. During MD, one O^- on the left surface became an –OH after one nearby H_2O deprotonated, while on the right surface one –OH is adsorbed. One ether is present on the left surface. Interfacial water

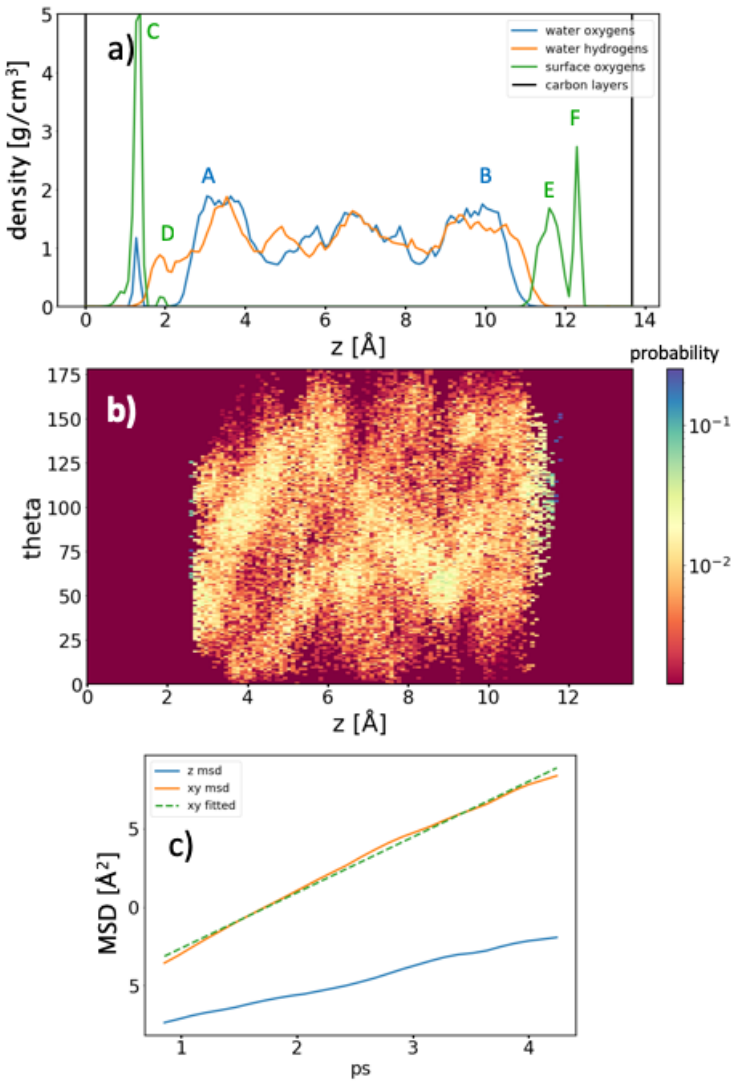

Figure 5.13: Water confined between rGO (20% –O– 10% –OH) layers with interlayer distance $d = 13.7$ Å. Mass density distribution of oxygens and hydrogens in water and mass density distribution of surface oxygens, as a function of their distance from the graphene layer (at 0 Å and 13.7 Å) (a). O–H bond orientation distribution of H_2O molecules (b). Mean squared displacement of H_2O molecules (c) along horizontal (xy) and perpendicular (z) directions with respect to graphene layers.

molecules are slightly oriented toward the left surface ($\theta \sim 15°$ - $145°$) while they stay almost parallel to the right surface ($\theta \sim 65°$ - $130°$). H_2O molecules confined between 10% –O– 20% –OH rGO layers have similar self-diffusion coefficients to the case that we previously analyzed, with $\overline{D_{xy}} = 1.8 \times 10^{-5} \frac{cm^2}{s}$ and $\overline{D_z} = 8.3 \times 10^{-6} \frac{cm^2}{s}$.

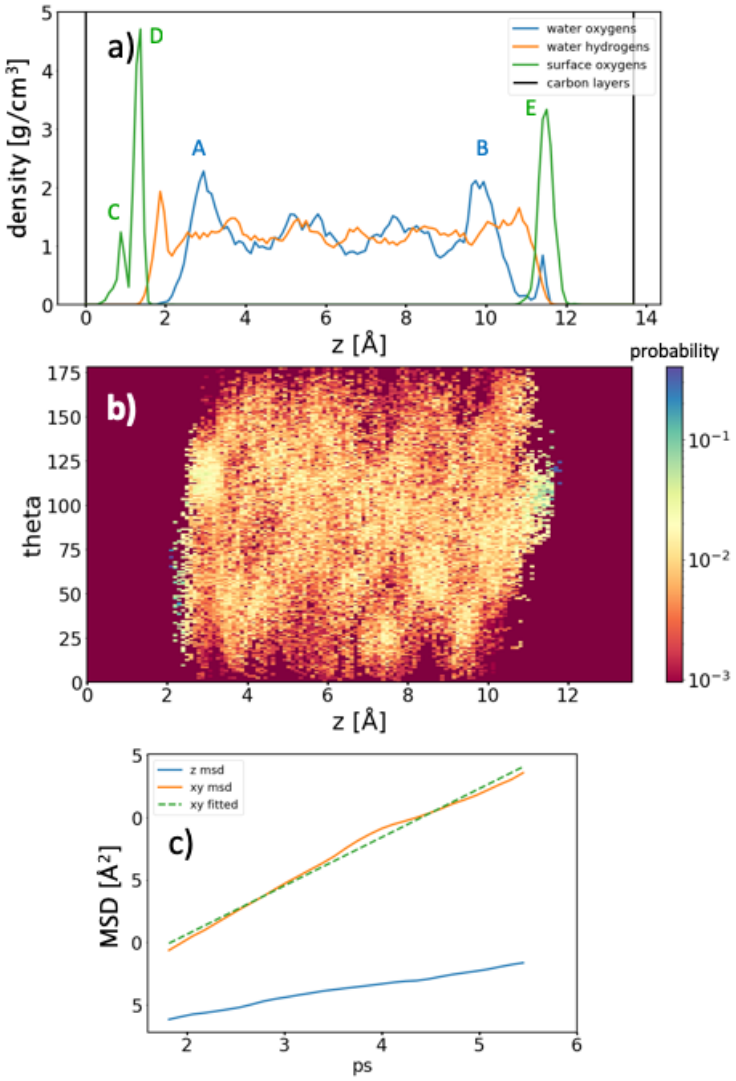

Figure 5.14: Water confined between rGO (10% –O– 20% –OH) layers with interlayer distance $d = 13.7$ Å. Mass density distribution of oxygens and hydrogens in water and mass density distribution of surface oxygens, as a function of their distance from the graphene layer (at 0 Å and 13.7 Å) (a). O–H bond orientation distribution of H_2O molecules (b). Mean squared displacement of H_2O molecules (c) along horizontal (xy) and perpendicular (z) directions with respect to graphene layers.

From the analysis of water confined between rGO layers we concluded that oxygen-containing groups have the effect of reducing both vertical and lateral diffusivities with respect to the case of pristine graphene. We confirmed, on the other hand, that the self-diffusivity of H_2O molecules increases in proximity of hydrophobic graphene surfaces. This phenomenon is particularly relevant when water is strongly confined, as

surface effects are dominant over the entire water layer. In the case of confinement between rGO layers instead, we observed a strong influence of oxygen-containing species on both lateral and perpendicular diffusivity of water. From our analysis we could not conclude whether different oxygen-containing species in rGO have distinct effects on water diffusivity. Although we observed slight reductions of lateral self-diffusion coefficients when increasing rGO oxidation from ($\Theta = 10\%$ to $\Theta = 30\%$), this differences are very small and probably negligible in experimental applications.

5.6 Conclusions and perspectives

In this Chapter we investigated interfaces between water and rGO, with the aim of defining solid relationships between the composition of rGO, its wettability and the structural and dynamical properties of water molecules near the interface. We discussed the strength of H-bonds interactions between water molecules and specific oxygen-containing groups that are commonly found in rGO, concluding that O^- and –OH species form the strongest H-bond with water molecules, with respectively $E^{O^-}_{H-bond} = -0.43$ eV and $E^{-OH}_{H-bond} = -0.24$ eV which are higher than the average H-bond energy between water molecules ($E^{H_2O}_{H-bond} = -0.215$ eV). Our results showed instead that epoxide and 1,2-ethers form weaker H-bonds with water molecules, with respectively $E^{epo}_{H-bond} = -0.199$ eV and $E^{eth}_{H-bond} = -0.14$ eV. These conclusions suggested that rGO containing a majority of –OH and O^- groups would be more hydrophilic than rGO with a predominance of epoxides and ethers. To study in greater detail the wettability of this material, we simulated isolated rGO monolayers with different compositions dispersed in water and analyzed their effects on the structural properties of H_2O molecules. From the analysis of molecules density and orientation distributions we observed the formation of interfacial layers where H_2O molecules accumulate and reorient in order to partially reconstruct the H-bond network disrupted by the presence of the interface [126]. Analyzing the average electric dipole distribution of water near graphene, we confirmed results from Cicero et al [126] by showing a drastic dipole reduction of H_2O molecules near the interface with respect to the bulk. In the case of rGO samples, at low coverages ($\Theta = 10\%$) we still observed reduced interfacial water electric dipoles with respect to the bulk, although to slightly higher values than in the case of graphene. Increasing the number of oxygen containing species instead ($\Theta = 30\%$), we observed an enhancement of interfacial electric dipoles with respect to bulk water that indicate the presence of a strong H-bond network between H_2O molecules and oxygen-containing groups in rGO. This is consistent with our results on the H-bond energy between oxygen-containing species and water molecules, with higher oxidation levels increasing the hydrophilicity of rGO sheets.

Finally, from the analysis of water confined between rGO layers we concluded that oxygen-containing groups have relevant effects on the diffusivity of water. We confirmed that confinement between pristine graphene layers enhances H_2O molecules

diffusivity with respect to bulk H_2O. Consistently with the work presented by Cicero and collaborators [126], where they suggested that such increase in water diffusivity is due to weaker electric dipoles, we also reported a remarkable reduction of H_2O electric dipoles near graphene. In the case of confinement between rGO layers instead, we observed a strong influence of oxygen-containing species on both lateral and perpendicular diffusivity of water. A recent paper from Mouhat and collaborators [132] reported an *ab initio* MD study of GO in liquid water aiming at investigating the properties of this material in water. Although that work has similar premises to this chapter, they only investigated GO structures with fixed stoichiometry (8.3% –O– 16.7% –OH) and performed different analysis. Nonetheless, conclusions from both works are consistent, regarding water diffusivity and chemical reactions between water and GO, with this work further exploring the effects of different confinement conditions and stoichiometries which are fundamental to accurately model experimental applications. To conclude, we expect this work to provide solid references to engineer and fabricate highly permeable and selective RO membranes for water purification based on multilayer rGO. Using accurate *ab initio* MD simulations we defined relationships between microscopical features of rGO flakes and the dynamical properties of water molecules intercalated between them. These can provide valuable resources to explain results from filtration experiments, as well as to qualitatively predict the performances of multilayer rGO membranes based on the composition of their flakes.

Conclusions

In this doctoral thesis we presented results from a research project involving the use of state of the art atomistic simulations to model and study the properties of reduced Graphene Oxide and its applications to membranes for reverse osmosis water filtration. The main ambition of this work was to improve scientific knowledge on the nature of rGO and its interactions with water, to facilitate its application to membrane technology for filtration.

Before studying rGO in water, we used state-of-the-art atomistic simulations to create accurate models for this material, considering different oxidation levels and stoichiometries to provide a comprehensive representation of typical experimental samples. After preparing these models, we used accurate DFT simulations to investigate the effects of specific oxygen-containing species on the structural and electronic properties of monolayer rGO. These simulations highlighted the presence of 1,2-ether groups, besides epoxides and hydroxyls, which were not included in either the Lerf-Klinowski or Szabó-Dékány models (the two most accepted atomic models for GO). Therefore, we proposed the addition of 1,2-ethers to the Lerf-Klinowski model (which our model structures were based on), as we demonstrated that these species induce distinct effects on both the structural and electronic properties of rGO. In this sense, we reported evidences of distinct modifications to the structure and to the valence band properties of rGO arising from epoxides, ethers and hydroxyl groups. Moreover, we provided indications about contributions of these oxygen-containing groups to XPS C-1s spectra, simulated by means of DFT, that we expect to be useful in interpreting XPS analysis of rGO.

After analyzing in details the contributions of oxygen-containing groups to the properties of rGO, we investigated the mechanisms that lead these species to diffuse and clusterize in monolayer rGO. In particular, we studied how to control this phenomenon and exploit it for producing pores of controlled size in monolayer rGO with the aim of fabricating single-layer membranes for water filtration, in a scalable and controllable way. With a combination of accurate DFT calculations and long (up to 5 days) KMC simulations we investigated the mechanisms driving the formation of epoxide clusters in rGO and simulated their evolution in time. The use of KMC, combined with CE to compute transition rates, allowed us to observe and analyze the diffusion and clusterization of epoxide species in rGO at different temperatures and for long times. In

this way we proved the existence of a direct relationship between annealing time and temperature and the area of resulting epoxide clusters, therefore opening the possibility to finely tune the size of oxidized areas by controlling annealing time, temperature and initial rGO coverage. After highlighting the experimental conditions to promote controlled clusterization, we studied the use of high-temperature thermal treatments to remove carbon atoms from oxidized areas, as a way to produce pores with accurate and uniform size in monolayer rGO. We concluded that pores only form in correspondence of initial clusters, while pristine graphene regions remained intact. The area or resulting pores strongly depends on the shape and size of initial clusters, as well as on their oxidation degree and on annealing temperatures. Our results showed that the best conditions in terms of carbon removal efficiency are obtained when using rGO structures containing large and dense circular clusters, processed at very high temperatures. Based on this work, we suggested a two-step experimental treatment that allows to generate pores of controlled size in rGO monolayers, consisting of a first mild annealing to tailor the morphology of the flake and a successive high-temperature treatment to create pores of accurate and uniform size. As this procedure allows in principle the possibility to fabricate rGO monolayers with controlled porosity in a scalable way, we expect it to have remarkable impacts on the application of single layer graphitic membranes for water desalination, with foreseable benefits in terms of power consumption of reverse osmosis desalination plants.

To further explore applications to membranes technology, we investigated the interactions between rGO and water. To this extent, we simulated isolated rGO monolayers dispersed in water and analyzed their effects on the structural properties of H_2O molecules. In particular, we studied how the composition of rGO influences its surface wettability, analyzing fundamental physical quantities of water molecules that provide an accurate description of the interactions between the solid surface and interfacial water molecules. From the analysis of molecules density, orientation and electric dipole, we concluded that the presence of oxygen-containing species in rGO allows water to form a H-bond network with the surface, creating a hydrophilic surface. This is particularly evident in the case of high-coverage rGO samples, whereas in low-coverage structures, the hydrophobic nature of the graphitic basal plane tends to dominate. We conclude that a majority of hydroxyl and O^- groups in rGO determines a strong enhancement of the interactions with interfacial water and therefore increases rGO hydrophilicity with respect to epoxides and ethers. Finally, from the analysis of water confined between rGO layers we concluded that oxygen-containing groups have relevant effects on the diffusivity of water. We observed a strong influence of oxygen-containing species on both lateral and perpendicular diffusivity of water.

To conclude, we expect this work to provide a solid computational reference for further investigations of rGO, shining light on fundamental open questions about its structure and about the role of oxygen-containing species in tailoring its properties. Moreover, our focus on applications to membranes for water filtration allowed us to draw fundamental conclusions about the interface between water and rGO, that will

hopefully contribute to developing more efficient membranes and reduce the high energy requirements of RO plants for water desalination. To this extent, the introduction of a scalable method to produce pores of controllable and repeatable dimensions in monolayer rGO flakes will have a huge impact on the development of effective single-layer graphitic membranes.

Bibliography

[1] S. Eigler et al. “Wet Chemical Synthesis of Graphene”. In: *Adv. Mater.* (2013).

[2] A. M. Dimiev and S. Eigler. *Graphene Oxide Fundamentals and Applications*. Wiley, 2017.

[3] B. C. Brodie. “Note sur un nouveau procédé pour la purification et la désagrégation du graphite”. In: *Ann. Chim. Phys.* 45 (1855).

[4] B. C. Brodie. “On the atomic weight of graphite”. In: *Phil. Trans. R. Soc. Lond.* 149 (1859).

[5] L. Staudenmaier. “Verfahren zur Darstellung von Graphitsäure”. In: *Ber. Dtsch. Chem. Ges.* 31 (1898).

[6] U. Hofmann. “Über Graphitsäure und die bei ihrer Zersetzung entstehenden Kohlenstoffarten”. In: *Ber. Dtsch. Chem. Ges.* 61 (1928).

[7] W. Scholz and H. P. Boehm. “Betrachtungen zur Struktur des Graphitoxids”. In: *Z. Anorg. Allg. Chem.* 369 (1969).

[8] H. P. Boehm. “Graphene – how a laboratory curiosity suddenly became extremely interesting”. In: *Angew. Chem. Int. Ed.* 49 (2010).

[9] F. Gottschalk. “Beiträge zur Kenntnis der Graphitsäure”. In: *J. Prakt. Chem.* 95 (1865).

[10] H. Thiele. “Über Salzbildung und Basenaustausch der Graphitsäure”. In: *Kolloid-Z.* 80 (1937).

[11] A. Clauss et al. “Untersuchungen zur Struktur des Graphitoxyds”. In: *Z. Anorg. Allg. Chem.* 291 (1957).

[12] K. S. Novoselov et al. “Electric Field Effect in Atomically Thin Carbon Films”. In: *Science* 306 (2004).

[13] W. Luzi. “Beiträge zur Kenntnis des Graphitkohlenstoffs”. In: *Z. Naturwiss.* 64 (1891).

[14] G. Charpy. “Sur la formation de l’oxyde graphitique et la définition du graphite”. In: *C. R. Hebd. Séances Acad. Sci.* 148 (1909).

[15] W.S. Hummers and R.E.. Offeman. "Preparation of graphite oxide". In: *J. Amer. Chem. Soc.* 80 (1958).

[16] H.P. Boehm, M. Eckel, and W. Scholz. "Über den Bildungsmechanismus des Graphitoxids". In: *Z. Anorg. Allg. Chem.* 353 (1967).

[17] H.P. Boehm and W. Scholz. "Vergleich der Darstellungsverfahren für Graphitoxyd". In: *Liebigs Ann. Chem.* 691 (1966).

[18] U. Hofmann, A. Frenzel, and E. Csalán. "Die Konstitution der Graphitsäure und ihre Reaktionen". In: *Liebigs Ann. Chem.* (1934).

[19] A.B. Bourlinos, D. Gournis, and D. Petridis. "Graphite oxide: chemical reduction to graphite and surface modification with primary aliphatic amines and amino acids". In: *Langmuir* 19 (2003).

[20] D. Voiry et al. "High-quality graphene via microwave reduction of solution-exfoliated graphene oxide". In: *Science* 353 (2016).

[21] H. Thiele. "Graphit und Graphitsäure". In: *Z. Anorg. Allg. Chem.* 190 (190).

[22] W. Scholz and H.P. Boehm. "Betrachtungen zur Struktur des Graphitoxids". In: *Z. Anorg. Allg. Chem.* 369 (1969).

[23] A. Lerf et al. "Structure of graphite oxide revisited". In: *J. Phys. Chem. B* 102 (1998).

[24] C. Gomez-Navarro et al. "Atomic structure of reduced graphene oxide". In: *Nano Lett.* 10 (2010).

[25] K. Erickson et al. "Determination of the local chemical structure of graphene oxide and reduced graphene oxide". In: *Adv. Mater.* 22 (2010).

[26] T. Szabó et al. "Evolution of surface functional groups in a series of progressively oxidized graphite oxides". In: *Chem. Mater.* 18 (2006).

[27] A. Dimiev, L. Alemany, and J.M. Tour. "Graphene oxide. Origin of acidity and dynamic structural models". In: *ACS Nano* 7 (2012).

[28] T. Szabó, O. Berkesi, and I. Dékány. "DRIFT study of deuterium-exchanged graphite oxide". In: *Carbon* 43 (2005).

[29] A.M Dimiev, L.B. Alemany, and J.M. Tour. "Graphene oxide. Origin of acidity, its instability in water, and a new dynamic structural model". In: *ACS Nano* 7 (2013).

[30] D Cohen-Tanugi and J.C. Grossman. "Water Desalination across Nanoporous Graphene". In: *Nano Lett.* 12 (2012).

[31] L.-C. Lin and J.C. Grossman. "Atomistic understandings of reduced graphene oxide as an ultrathin-film nanoporous membrane for separations". In: *Nat. Comm.* (2015).

[32] R.K. Joshi et al. “Precise and ultrafast molecular sieving through graphene oxide membranes”. In: *Science* 343 (2014).

[33] R Devanathan et al. “Molecular Dynamics Simulations Reveal that Water Diffusion between Graphene Oxide Layers is Slow”. In: *Sci. Rep.* (2016).

[34] B. Chen et al. “Observation and Analysis of Water Transport Through Graphene Oxide Interlamination”. In: *J. Phys. Chem. C* (2017).

[35] W. Li et al. “Molecular Dynamics Simulations of CO2/N2 Separation through Two-Dimensional Graphene Oxide Membranes”. In: *J. Phys. Chem. C* 120 (2016).

[36] A.D. DeYoung et al. “Graphene Oxide Supercapacitors: A Computer Simulation Study”. In: *J. Phys. Chem. C* 118 (2014).

[37] S. Kim et al. “Room-temperature metastability of multilayer graphene oxide films”. In: *J. Phys. Chem. C* 11 (2012).

[38] S. Zhou and A. Bongiorno. “Origin of the chemical and kinetic stability of graphene oxide”. In: *Sci. Rep.* (2013).

[39] R. Larciprete et al. “Dual Path Mechanism in the Thermal Reduction of Graphene Oxide”. In: *J. Am. Chem. Soc.* 133 (2011).

[40] T. Sun and S. Fabris. “Mechanisms for Oxidative Unzipping and Cutting of Graphene”. In: *Nano Lett.* 12 (2012).

[41] D.W. Boukhvalov and M. I. Katsnelson. “Modelling of Graphite Oxide”. In: *J. Am. Chem. Soc* 130 (2008).

[42] R.J.W.E Lahaye et al. “Density functional theory study of graphite oxide for different oxidation levels”. In: *Phys. Rev. B* 79 (2009).

[43] J. Ito, J. Nakamura, and A. Natori. “Semiconducting nature of the oxygen-adsorbed graphene sheet”. In: *J. Appl. Phys.* 103 (2008).

[44] W. Li et al. “Molecular Dynamics Simulations of CO_2/N_2 Separation through Two-Dimensional Graphene Oxide Membranes”. In: *J. Phys. Chem. C* 10 (2015).

[45] R.W. Baker. *Membrane Technology and Applications*. Wiley, 2004.

[46] S. Homaeigohar and M. Elbahri. “Graphene membranes for water desalination”. In: *NPG Asia Mater.* 9 (2017).

[47] V. Berry. “Impermeability of graphene and its applications”. In: *J. Appl. Phys.* (2013).

[48] B. Corry. “Designing Carbon Nanotube Membranes for Efficient Water Desalination”. In: *J. Phys. Chem. B* 112 (2008).

[49] S. C. O’Hern et al. “Selective molecular transport through intrinsic defects in a single layer of CVD graphene”. In: *ACS Nano* 6 (2012).

[50] S. P. Surwade et al. “Water desalination using nanoporous single-layer graphene”. In: *Nat. Nanotechnol.* 10 (2015).

[51] S. C. O’Hern et al. “Selective Ionic Transport through Tunable Subnanometer Pores in Single-Layer Graphene Membranes”. In: *Nano Lett.* 14 (2014).

[52] N. Wei, X. Peng, and Z. Xu. “Understanding Water Permeation in Graphene Oxide Membranes”. In: *Appl. Mater. Interfaces* 6 (2014).

[53] L. Huang et al. “Graphene Based Membranes for Molecular Separation”. In: *J. Phys. Chem. Lett.* (2015).

[54] J.W. Burres et al. “Graphene Oxide Framework Materials: Theoretical Predictions and Experimental Results”. In: *Angew. Chem.* 49 (2010).

[55] B. Mi. “Graphene Oxide Membranes for Ionic and Molecular Sieving”. In: *Science* 343 (2014).

[56] E. Fortunato et al. “Transparent Conducting Oxides for Photovoltaics”. In: *MRS Bulletin* 32 (2007).

[57] F. Bonaccorso et al. “Graphene photonics and optoelectronics”. In: *Nat. Photonics* 4 (2010).

[58] Q. Zheng et al. “Graphene oxide-based transparent conductive films”. In: *Prog. Mater. Sci.* 64 (2014).

[59] J.D. Roy-Mayhew and I.A. Aksay. “Graphene Materials and Their Use in Dye-Sensitized Solar Cells”. In: *Chem. Rev.* 114 (2014).

[60] J. Zhu et al. “Graphene and Graphene-Based Materials for Energy Storage Applications”. In: *Small* 10 (2014).

[61] N. Mahmood et al. “Graphene-based nanocomposites for energy storage and conversion in lithium batteries, supercapacitors and fuel cells”. In: *J. Mater. Chem. A* 2 (2014).

[62] S. Gilje et al. “A Chemical Route to Graphene for Device Applications”. In: *Nano Lett.* 7 (2007).

[63] S. Kochmann, T. Hirsch, and O.S. Wolfbeis. “Graphenes in chemical sensors and biosensors”. In: *Trends Anal. Chem.* 39 (2012).

[64] K. Toda, R. Furue, and S. Hayami. “Recent progress in applications of graphene oxide for gas sensing: A review”. In: *Anal. Chim. Acta* (2015).

[65] J.T. Robinson et al. “Reduced Graphene Oxide Molecular Sensors”. In: *Nano Lett.* 8 (2008).

[66] P. Hohenberg and W. Kohn. “Inhomogeneous Electron Gas”. In: *Physical Review, 136* (1964).

[67] W. Kohn and L. J. Sham. “Self-Consistent Equations Including Exchange and Correlation Effects”. In: *Physical Review, 140* (1965).

[68] R. M. Martin. *Electronic Structure, Basic Theory and Practical Methods.* Cambridge University Press, 2004.

[69] D. M. Ceperley and B. J. Alder. "Ground State of the Electron Gas by a Stochastic Method". In: *Physical Review Letters* (1980).

[70] A. D. Becke. "Density-functional exchange-energy approximation with correct asymptotic behavior". In: *Physical Review A, 38* (1988).

[71] J. P. Perdew et al. "Atoms, molecules, solids and surfaces: Applications of the generalized gradient approximation for exchange and correlation". In: *Physical Review B, 46* (1992).

[72] J. P. Perdew, K. Burke, and M. Ernzerhof. "Generalized Gradient Approximation Made Simple". In: *Physical Review Letters, 77* (1996).

[73] A. D. Becke. "A new mixing of Hartree-Fock and local density-functional theories". In: *J. Chem. Phys. 98* (1993).

[74] J.P Perdew, M. Ernzerhof, and K. Burke. "Rationale for mixing exact exchange with density functional approximations". In: *J. Phys. Chem.* 105 (1996).

[75] C. Lee, W. Yang, and Parr. "Development of the Colle-Salvetti correlation-energy formula into a functional of the electron density". In: *Physical Review B, 37* (1988).

[76] A. R. Sidik et al. "O_2 Reduction on Graphite and Nitrogen-Doped Graphite: Experiment and Theory". In: *J. Phys. Chem. B 110* (2006).

[77] G. L. Li et al. "Organo- and Water-Dispersible Graphene Oxide-Polymer Nanosheets for Organic Electronic Memory and Gold Nanocomposites". In: *J. Phys. Chem. C 114* (2010).

[78] R. Dovesi et al. *CRYSTAL14 User's Manual (University of Torino, Torino, 2014).*

[79] P. Giannozzi et al. "QUANTUM ESPRESSO: a modular and open-source software project for quantum simulations of materials". In: *J. Phys.: Condens. Matter* 21 (2009).

[80] H. J. Monkhorst and J. D. Pack. "Special points for Brillouin-zone integrations". In: *Physical Review B, 13* (1976).

[81] S. Plimpton. "ReaxFF: A Reactive Force Field for Hydrocarbons". In: *J. Comp. Phys., 117* (1995).

[82] A. Bagri et al. "Stability and Formation Mechanisms of Carbonyl- and Hydroxyl-Decorated Holes in Graphene Oxide". In: *J. Phys. Chem. C* (2010).

[83] A. Bagri et al. "Structural evolution during the reduction of chemically derived graphene oxide". In: *Nature Chemistry* (2010).

[84] R. M. Abolfath and A. C. T. van Duin. "Molecular-Dynamics-Based Study of the Collisions of Hyperthermal Atomic Oxygen with Graphene Using the ReaxFF Reactive Force Field". In: *J. Phys. Chem. A* (2011).

[85] S. G. Srinivasan and K. Cho. "Computational Studies for Reduced Graphene Oxide in Hydrogen- Rich Environment". In: *J. Phys. Chem. A* (2012).

[86] R. Car and M. Parrinello. "Unified Approach for Molecular Dynamics and Density-Functional Theory". In: *Phys. Rev. Lett.* 55 (1985).

[87] D. Marx and J. Hutter. Ab initio *Molecular Dynamics: Basic Theory and Advanced Methods*. Cambridge University Press, 2009.

[88] D. J. Evans and Holian B. L. "The Nose-Hoover thermostat". In: *J. Chem. Phys. 83* (1985).

[89] G Ceder. "A derivation of the Ising model for the computation of phase diagrams". In: *Comput. Mater. Sci.* 1 (1993).

[90] F. Raffone et al. "MoS2 enhanced T-phase stabilization and tunability through alloying". In: *Phys. Chem. Lett.* 7 (2016).

[91] S. Piccinin and M. Stamatakis. "CO oxidation on Pd(111): a first- principles-based kinetic Monte Carlo study". In: *ACS Catal.* 4 (2014).

[92] J. M. Bray and W. F. Schneider. "First-principles analysis of structure sensitivity in NO oxidation on Pt". In: *ACS Catal.* 5 (2015).

[93] F. Raffone, F. Savazzi, and G. Cicero. "Controlled Pore Generation in Single-Layer Graphene Oxide for Membrane Desalination". In: *J. Phys. Chem. Lett.* 10 (2019).

[94] A. van de Walle and G. Ceder. "Automating first-principles phase diagram calculations". In: *J. Phase Equilib.* 23 (2002).

[95] A.P.J. Jansen. *An introduction to kinetic Monte Carlo simulations of surface reactions*. Springer, 2012.

[96] F. Savazzi et al. "Unravelling Some of the Structure–Property Relationships in Graphene Oxide at Low Degree of Oxidation". In: *J. Phys. Chem. Lett.* 9 (2018).

[97] S. Pei and H.-M. Cheng. "The Reduction of Graphene Oxide". In: *Carbon* 50 (2012).

[98] C. Mattevi et al. "Evolution of Electrical, Chemical and Structural Properties of Transparent and Conducting Chemically Derived Graphene Thin Films". In: *Adv. Funct. Mater.* 19 (2009).

[99] S. Plimpton. "Fast parallel algorithms for short-range molecular dynamics". In: *J. Phys. Chem. Lett.* 117 (1995).

[100] P. V. Kumar et al. "Scalable enhancement of graphene oxide properties by thermally driven phase transformation". In: *Nat. Chem.* 6 (2014).

[101] R. Dovesi et al. "CRYSTAL14: A Program for the Ab Initio Investigation of Crystalline Solids". In: *Int. J. Quantum Chem.*. 114 (2014).

[102] L. Pisani et al. "Electronic Structure and Magnetic Properties of Graphitic Ribbons". In: *Phys. Rev. B* 75 (2007).

[103] F. Corà. "The Performance of Hybrid Density Functionals in Solid State Chemistry: The Case of BaTiO3." In: *Mol. Phys.* 103 (2005).

[104] C. Gatti, V. R. Saunders, and C. Roetti. "Crystal Field Effects on Topological Properties of the Electron Density in Molecular Crystals". In: *J. Chem. Phys.* 101 (1994).

[105] W.A. Harrison. *Electronic Structure and the Properties of Solids: The Physics of the Chemical Bond*. Dover, 1989.

[106] R.F.W. Bader. "A Quantum Theory of Molecular Structure and Its Applications". In: *Chem. Rev.* 91 (1991).

[107] Z. Md. Hossain et al. "Chemically Homogeneous and Thermally Reversible Oxidation of Epitaxial Graphene". In: *Nat. Chem.* 4 (2012).

[108] A. Barinov et al. "Initial Stages of Oxidation on Graphitic Surfaces: Photoemission Study and Density Functional Theory Calculations". In: *J. Phys. Chem. C* 113 (2009).

[109] J.-Q. Huang et al. "Permselective Graphene Oxide Membrane for Highly Stable and Anti Self Discharge Lithium Sulfur Batteries". In: *ACS Nano* (2015).

[110] D. Konatham et al. "Simulation insights for graphene-based water desalination membranes". In: *Langmuir* 38 (2013).

[111] M. D. Fischbein and M. Drndić. "Electron beam nanosculpting of suspended graphene sheets". In: *Appl. Phys. Lett.* 93 (2008).

[112] M.-C. M.-C.Clochard et al. "Large area fabrication of self-standing nanoporous graphene-on-PMMA substrate". In: *Mat. Lett.* 184 (2016).

[113] P.V. Kumar, M. Bernardi, and J.C. Grossman. "The Impact of Functionalization on the Stability, Work Function, and Photoluminescence of Reduced Graphene Oxide". In: *ACS Nano* 7 (2013).

[114] P.V. Kumar et al. "New insights into the thermal reduction of graphene oxide: Impact of oxygen clustering". In: *Carbon* 100 (2016).

[115] J. Nielsen et al. "Parallel kinetic Monte Carlo simulation framework incorporating accurate models of adsorbate lateral interactions". In: *Appl. Phys. Lett* 139 (2013).

[116] M. Stamatakis. "Kinetic modelling of heterogeneous catalytic systems". In: *J. Phys.: Condens. Matter* 27 (2015).

[117] M. Stamatakis and D. G. Vlachos. "A graph-theoretical kinetic Monte Carlo framework for on-lattice chemical kinetics". In: *J. Chem. Phys.* 134 (2011).

[118] D. Vanderbilt. "Soft Self-Consistent Pseudopotentials in a Generalized Eigenvalue Formalism". In: *Phys. Rev. B* 41 (1990).

[119] C. Riplinger and F. Neese. "An efficient and near linear scaling pair natural orbital based local coupled cluster method". In: *J. Chem. Phys.* 138 (2013).

[120] F. Neese. "Software update: the ORCA program system, version 4.0". In: *Wiley Interdiscip. Rev. Comput. Mol. Sci.* 8 (2017).

[121] J. Sun et al. "SCAN: An Efficient Density Functional Yielding Accurate Structures and Energies of Diversely-Bonded Materials". In: *arXiv preprint* arXiv:1511.01089 (2015).

[122] C. Adamo and V. Barone. "Toward reliable density functional methods without adjustable parameters: The PBE0 model". In: *J. Chem. Phys.* 110 (1999).

[123] K. Vijayarangamuthu et al. "Temporospatial control of graphene wettability". In: *Adv. Mater.* 28 (2016).

[124] J.C. Grossman et al. "Towards an assessment of the accuracy of density functional theory for first principles simulations of water". In: *J. Phys. Chem.* 120 (2004).

[125] E. Schwegler et al. "Towards an assessment of the accuracy of density functional theory for first principles simulations of water. II". In: *J. Phys. Chem.* 121 (2004).

[126] G. Cicero et al. "Water Confined in Nanotubes and between Graphene Sheets: A First Principle Study". In: *J. Am. Chem. Soc.* 130 (2008).

[127] M.J. Abraham et al. "GROMACS: High performance molecular simulations through multi-level parallelism from laptops to supercomputers". In: *SoftwareX* (2015).

[128] J. Abraham et al. "Tunable sieving of ions using graphene oxide membranes". In: *Nat. Nanotechnol.* 12 (2017).

[129] D. Keffer. "The Working Man's Guide to Obtaining Self Diffusion Coefficients from Molecular Dynamics Simulations." In: 148 (2018).

[130] N. Marzari and D. Vanderbilt. "Maximally localized generalized Wannier functions for composite energy bands". In: *Phys. Rev. B* 56 (1997).

[131] W. Dawson and F. Gygi. "Equilibration and analysis of first-principles molecular dynamics simulations of water". In: *J. Chem. Phys.* 148 (2018).

[132] F. Mouhat, F.-X. Courdet, and M.-L. Boucquet. "Structure and chemistry of graphene oxide in liquid water from first principles". In: *Nat. Comm.* 11 (2020).

This Ph.D. thesis has been typeset by means of the TEX-system facilities. The typesetting engine was LuaLATEX. The document class was `toptesi`, by Claudio Beccari, with option `tipotesi=scudo`. This class is available in every up-to-date and complete TEX-system installation.